



Review

Progress in 2D photonic crystal Fano resonance photonics

Weidong Zhou^{a,*}, Deyin Zhao^a, Yi-Chen Shuai^a, Hongjun Yang^a,
Santhad Chuwongin^a, Arvinder Chadha^a, Jung-Hun Seo^b, Ken X. Wang^c,
Victor Liu^c, Zhenqiang Ma^{b,**}, Shanhui Fan^{c,***}

^aDepartment of Electrical Engineering, University of Texas at Arlington, Arlington, TX 76019, USA

^bDepartment of Electrical and Computer Engineering, University of Wisconsin-Madison, Madison, WI 53706, USA

^cDepartment of Electrical Engineering, Stanford University, Stanford, CA 94305, USA

Available online 15 February 2014

Abstract

In contrast to a conventional symmetric Lorentzian resonance, Fano resonance is predominantly used to describe asymmetric-shaped resonances, which arise from the constructive and destructive interference of discrete resonance states with broadband continuum states. This phenomenon and the underlying mechanisms, being common and ubiquitous in many realms of physical sciences, can be found in a wide variety of nanophotonic structures and quantum systems, such as quantum dots, photonic crystals, plasmonics, and metamaterials. The asymmetric and steep dispersion of the Fano resonance profile promises applications for a wide range of photonic devices, such as optical filters, switches, sensors, broadband reflectors, lasers, detectors, slow-light and non-linear devices, etc. With advances in nanotechnology, impressive progress has been made in the emerging field of nanophotonic structures. One of the most attractive nanophotonic structures for integrated photonics is the two-dimensional photonic crystal slab (2D PCS), which can be integrated into a wide range of photonic devices. The objective of this manuscript is to provide an in depth review of the progress made in the general area of Fano resonance photonics, focusing on the photonic devices based on 2D PCS structures. General discussions are provided on the origins and characteristics of Fano resonances in 2D PCSs. A nanomembrane transfer printing fabrication technique is also reviewed, which is critical for the heterogeneous integrated Fano resonance photonics. The majority of the remaining sections review progress made on various photonic devices and structures, such as high quality factor filters, membrane reflectors, membrane lasers, detectors and sensors, as well as structures and

*Corresponding author. Tel.: +1 817 272 1227.

**Corresponding author. Tel.: +1 608 261 1095.

***Corresponding author. Tel.: +1 650 724 4759.

E-mail addresses: wzhou@uta.edu (W. Zhou), mazq@engr.wisc.edu (Z. Ma), shanhui@stanford.edu (S. Fan).

phenomena related to Fano resonance slow light effect, nonlinearity, and optical forces in coupled PCSs. It is expected that further advances in the field will lead to more significant advances towards 3D integrated photonics, flat optics, and flexible optoelectronics, with lasting impact in areas ranging from computing, communications, to sensing and imaging systems.

© 2014 Elsevier Ltd. All rights reserved.

Keywords: Fano resonances; Photonic crystals; Membrane lasers; Filters; Slow light; Silicon photonics

Contents

1. Introduction	3
2. Principles of Fano resonance in photonic crystal slabs	5
2.1. 2D Photonic Crystal Slabs	5
2.2. The presence of Fano resonance in photonic crystal slabs	5
2.3. Characteristics of Fano resonance in photonic crystal slabs	6
3. Transfer printing techniques for Fano resonance photonics	8
3.1. Transfer printed semiconductor nanomembranes for Fano resonance photonics	8
3.2. Comparison with other epitaxial lift-off (ELO) and wafer bonding processes	13
4. Fano resonance photonic crystal filters	15
4.1. Single layer filters	15
4.2. Coupled double layer filters	21
4.3. Fano resonance filter configurations	24
4.3.1. Single layer Fano resonance filters	24
4.3.2. Double layer Fano resonance filters	26
4.3.3. Double layer Fano resonance filters with controlled lattice displacement	27
5. Fano resonance photonic crystal membrane reflectors	30
5.1. Broadband reflector design	31
5.2. Different configurations and buffer layer design	33
5.3. Energy and phase penetration properties in membrane reflectors	34
5.4. Angle and polarization properties	36
6. Fano resonance photonic crystal membrane lasers	37
6.1. Photonic crystal functions in light sources	37
6.2. Design of MR-VCSELs	39
6.3. MR-VCSEL Fabrication and configurations	42
6.3.1. Epitaxial growth approach	42
6.3.2. Wafer bonding and CMP techniques	43
6.3.3. Transfer printing techniques	43
7. Fano resonance photonic crystal field localization and absorption engineering	46
7.1. Electromagnetic field localization and enhancement in photonic crystal cavities	46
7.2. Demonstration of spectral-selective absorption enhancement and IR detectors	49
7.2.1. CQD integrated Si-NM Fano filters	49
7.2.2. Fano resonance enhanced photonic crystal Infrared Photodetectors	51
8. Fano resonance photonic crystal sensors	54
8.1. Asymmetric Fano resonance line shape and high Q cavities	54
8.2. Fano resonance PCS sensor configurations	55
9. Fano resonance photonic crystal cavity optomechanics	57
9.1. Optical forces in nano-scale cavities	57
9.2. Optical forces in coupled Fano resonance PCSs	58

9.3. Optomechanical control and MOMES applications	63
10. Fano resonance photonic crystal slowlight and nonlinearity	63
10.1. Slowlight and stopping light in Fano resonance photonic crystals	63
10.2. Bi-stability, switching, and modulation.	64
11. Conclusions and prospects	66
Acknowledgments	67
References	67

1. Introduction

In contrast to a conventional symmetric-shaped Lorentzian resonance, Fano resonance is predominantly used to describe asymmetric resonance [1,2], which arises from the constructive and destructive interference of discrete resonance states by broadband continuum states. First observed from the transmission spectra of gratings, Fano resonance is responsible for one variety of Wood's anomalies [3]. This phenomenon and the underlying mechanism, being common and ubiquitous in many realms of physical sciences [1,4], are found in a wide variety of nanophotonic structures and quantum systems, such as quantum dots, photonic crystals (PhCs), plasmonics, and metamaterials. The asymmetric and steep dispersion of the Fano resonance profile promises applicability in a wide range of photonic devices, such as optical filters, switches, sensors, broadband reflectors, lasers, detectors, slow-light and non-linear devices, etc. With the advances in nano-fabrication processes and the development of integration techniques, Fano resonance based materials, structures, devices, and systems have been widely investigated and reported over the last few years. There are also excellent reviews written by many experts in the field. Miroshnichenko et al. [4] presented a detailed review on the principles and origins of Fano resonance in various nanostructures and physical systems. Luk'yanchuk et al. [5,6] and Giannini et al. [7] presented reviews on progress made on Fano resonance in plasmonic nanostructures and metamaterials.

Here we focus our review on progress made in PhC Fano resonance photonics, with a specific focus on Fano resonances in two-dimensional photonic crystal slabs (2D PCS) [8,9]. Optical gratings, which can also be viewed as 1D PhCs, are a research topic with a long history, including guided mode resonances (GMRs) in 1D gratings, reported by Magnusson et al. [10–12]. Recently, due to the unique characteristics and potentials for high performance optic and photonic devices, subwavelength high-index-contrast gratings (HCGs) have been proposed and investigated by Chang-Hasnain et al. [13–16] for applications in mirrors, lasers, and focusing elements, etc. [13].

2D PCS structures also support guided resonances [9,17]. In one of the original papers on this topic, Fan et al. [9] presented a detailed analysis of the guided resonances in 2D PCS structures and investigated the transmission/reflection spectra properties in such systems when these modes are coupled with vertical radiation modes. Subsequently, many theoretical and experimental papers appeared on this topic with investigations on associated physical characteristics of such resonances and related device demonstrations. This paper attempts to review the progress made in this general area of Fano resonance photonics, based on 2D PCS structures. An outline of what this review will cover is presented in Fig. 1. Based on the unique physical properties, various photonic devices can be realized for a wide range of applications. In Section 2, we will briefly discuss the Fano resonance principles and characteristics. The fabrication technique associated with Fano resonance photonic devices, transfer printing of heterogeneously integrated materials

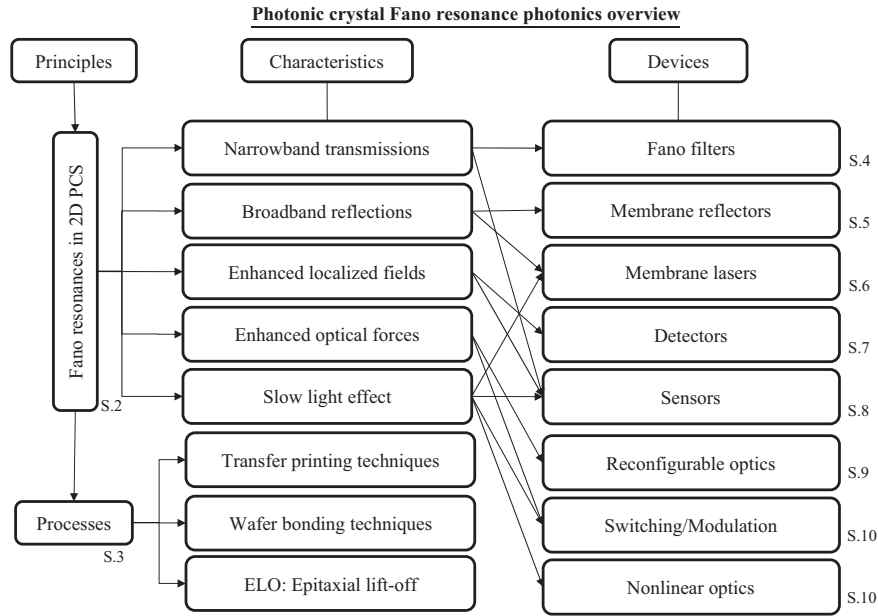


Fig. 1. Overview of photonic crystal Fano resonance photonics: principles, processes, characteristics, and device applications. Topics covered in different sections of this review are denoted with S.1, S.2, etc.

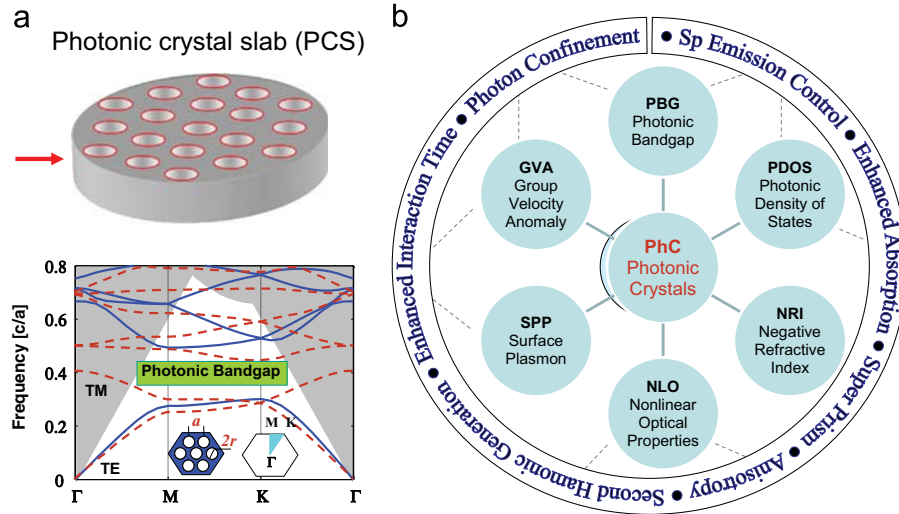


Fig. 2. Two-dimensional photonic crystal slabs (2D PCS): (a) schematic representation of triangular lattice PCS, with simulated dispersion plot for two (TE/TM) polarizations; and (b) overview of photonic crystal properties and applications.

on various substrates, will be introduced in [Section 3](#). The majority of the remaining sections will be arranged based on different device applications, including filters ([Section 4](#)), reflectors ([Section 5](#)), lasers ([Section 6](#)), detectors ([Section 7](#)) and sensors ([Section 8](#)). Finally, optical

forces in coupled PCSs, Fano resonance slow light effect, and nonlinearity, will be discussed in Sections 9 and 10, followed by a conclusion.

2. Principles of Fano resonance in photonic crystal slabs

2.1. 2D Photonic Crystal Slabs

2D PCSs are a particularly important class of PhC structures [18,19]. A 2D PCS consists of a two-dimensionally periodic index contrast introduced into a high-index guiding layer. As shown in Fig. 2(a), PCSs are quasi-3D structures in which the light confinement arises from the in-plane 2D photonic bandgap (PBG) confinement and vertical waveguide index confinement (through the total internal reflection or TIR principle). 2D PCS structures are certainly more amenable to fabrication of devices using current semiconductor technology than three dimensional structures, yet they provide much the same amount of functionality (Fig. 2(b)) [20]. 2D PCS can be easily integrated with other photonic components for photonic integrated circuits (PICs) using planar micro- and nano-fabrication processes [21–27]. One of the most widely studied structures is the triangular lattice based air column 2D PCS structure, which possesses a large transverse-electric (TE) and transverse-magnetic (TM) like mode and a large complete TE/TM PBG. A typical dispersion plot is shown in Fig. 2(a), where a complete TE/TM bandgap is shown. Note that a light core region is formed due to the vertical confinement. These structures support in-plane guided modes below the lightlines, which are completely confined by the slab without any coupling to external radiations.

2.2. The presence of Fano resonance in photonic crystal slabs

In addition to in-plane waveguiding, PCS can also interact with external radiation in complex and interesting ways. Of particular importance here is the presence of guided resonance in the structures [9,17]. Similar to the guided mode, for guided resonance the electro-magnetic power is also strongly confined within the slab. Unlike the guided mode, however, the resonance can be coupled with external radiation (the leaky mode is above the lightline, Fig. 2(a)). Therefore, guided resonance can provide an efficient way to channel light from within the slab to the external environment. A detailed theoretical analysis of guided resonances in 2D PCS's was first presented by Fan et al. [9]. Kanskar et al. [28] presented one of the first experimental reports of guided resonances at optical frequencies in a 2D PCS structure based on a suspended AlGaAs layer.

For light incident on PCS from out of the plane direction (e.g. surface-normal direction), photon transport can take two pathways: a direct or background pathway that does not involve the guided resonance or a resonance-assisted pathway in which photons are coupled into the resonances and subsequently leak out to free space. Assuming that the slab has mirror symmetry in the vertical direction, and taking into consideration the interference between these two pathways, we express the transmission amplitude t as a function of frequency ω

$$t = t_d + f \frac{\gamma}{i(\omega - \omega_0) + \gamma} \quad (1)$$

$$r = r_d \pm f \frac{\gamma}{i(\omega - \omega_0) + \gamma} \quad (2)$$

where t_d and r_d are the direct transmission and reflection coefficients, ω_0 and γ are the center frequency and width of the resonance, respectively, and f is the normalized complex amplitude of the resonant mode. The plus and minus sign correspond with even and odd resonant modes for structures with the mirror symmetry. Energy conservation requires

$$f = -(t_d \pm r_d) \quad (3)$$

For $0 < |t_d| < 1$, Eq. (1) gives a Fano resonance lineshape. For example, we consider a system consisting of a square lattice of air holes introduced into a dielectric slab (Fig. 3(a)). The intensity transmission spectrum is given in Fig. 3(b and c), exhibiting Fano resonance lineshapes with strong asymmetric profiles. Using finite-difference time-domain (FDTD) simulations, one can determine the parameters for Eq. (1) and compare the spectrum from this theoretical derivation to that from the FDTD simulation (Fig. 3(b and c)).

In the vicinity of the Fano resonance, the intensity transmission in Fig. 3(b) undergoes a transition between 0% and 100%, meaning the constructive and destructive interferences are located close to each other. This phenomenon is due to the rapid variation of the phase along the localized (resonance-assisted) pathway compared to the background pathway.

2.3. Characteristics of Fano resonance in photonic crystal slabs

While Eq. (1) intuitively captures the interference between the background and the resonance-assisted pathways, it can be naturally derived from the more general and phenomenological temporal coupled-mode theory [19], in which a system is modeled as a set of localized and propagating modes. Instead of introducing the general formalism dealing with an arbitrary number of resonances and waveguides [30], Fan et al. [29] focused on the simple case of a single resonance coupled to two ports to better illustrate the essence of the physical process. This two-port configuration could be guaranteed in the structure when the light's wavelength is greater than the lattice constant such that there is no diffraction above or below the slab, as shown in Fig. 3(a).

The dynamics of this lossless single-resonance double-port system is described by the coupled-mode equations

$$\frac{da}{dt} = \left(i\omega_0 - \frac{1}{\tau}\right)a + (\kappa_1 \ \kappa_2) \begin{pmatrix} s_{1+} \\ s_{2+} \end{pmatrix} \quad (4)$$

$$\begin{pmatrix} s_{1-} \\ s_{2-} \end{pmatrix} = C \begin{pmatrix} s_{1+} \\ s_{2+} \end{pmatrix} + a \begin{pmatrix} d_1 \\ d_2 \end{pmatrix} \quad (5)$$

where a is the amplitude of the resonant mode such that $|a|^2$ represents the electromagnetic energy stored in the resonance. ω_0 and $\gamma = 1/\tau$ are the center frequency and the width of the resonance, respectively. s_{1+} and s_{2+} are the incoming amplitudes of the planewaves on the two ports such that $|s_{1+}|^2$ and $|s_{2+}|^2$ correspond with the intensities. s_{1-} and s_{2-} are the outgoing amplitudes of the planewaves from the two ports such that $|s_{1-}|^2$ and $|s_{2-}|^2$ correspond with the intensities. κ_1 and κ_2 are the coupling constants between the incoming waves and the resonance, respectively. d_1 and d_2 are the coupling constants between the outgoing waves and the resonance, respectively. C is the background scattering matrix.

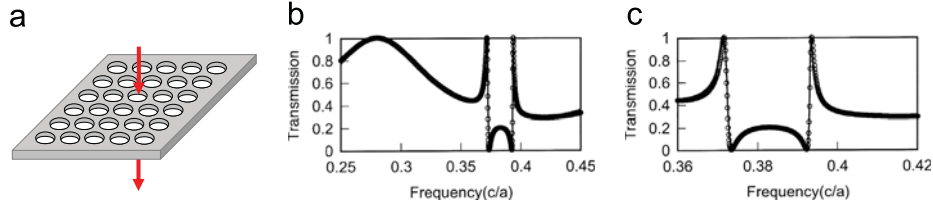


Fig. 3. Fano resonances in 2D photonic crystal slabs: (a) photonic crystal structure consisting of a square lattice of air holes with a radius of $r=0.2a$ in a dielectric slab with dielectric constant $n_h=12$ and a thickness (t) of $0.5a$, where a is the lattice constant. The arrow indicates the direction of the incident light. (b) The intensity transmission spectrum through such a structure. The circles are the result of the finite-difference time-domain simulations. The solid curve is determined by the analytic theory as represented by Eq. (1). (c) The same plot as (b), except the frequency range is now restricted to $[0.36(c/a), 0.42(c/a)]$ to exhibit further details of the resonance line shape. Reproduced with permission from [29].

The coupling constants are constrained by energy conservation and time-reversal symmetry as follows [30]:

$$|d_1|^2 + |d_2|^2 = \frac{2}{\tau} \quad (6)$$

$$\kappa_1 = d_1, \quad \kappa_2 = d_2 \quad (7)$$

$$C \begin{pmatrix} d_1^* \\ d_2^* \end{pmatrix} = - \begin{pmatrix} d_1 \\ d_2 \end{pmatrix} \quad (8)$$

By choosing the appropriate positions of the reference planes, without loss of generality, the direct scattering matrix C can be expressed as

$$C = e^{i\phi} \begin{pmatrix} r & it \\ it & r \end{pmatrix} \quad (9)$$

where ϕ is a phase factor, and r and t , both being real, are the reflection and transmission coefficients of the direct process satisfying $r^2 + t^2 = 1$ [31]. Combining Eqs. (6)–(9), one can solve for the coupling constants in terms of the decay rate and the elements in the direct scattering matrix [32], and the theory accounts for asymmetric photonic crystal slabs [33]. For the structure with mirror symmetry in Fig. 3(a), one can further simplify the solution by requiring $d_1 = d_2$, and the intensity reflection coefficient R is therefore

$$R = \frac{r^2(\omega - \omega_0)^2 + t^2(1/\tau)^2 \mp 2rt(\omega - \omega_0)(1/\tau)}{(\omega - \omega_0)^2 + (1/\tau)^2} \quad (10)$$

which agrees with Eq. (2).

Typically there are two techniques for the simulation of the transmission and reflection properties of PCS structures. The first approach is the rigorous coupled wave analysis (RCWA) technique [34], a relatively straightforward technique for obtaining the exact solution of Maxwell's equations for the electromagnetic diffraction of grating structures. It is a non-iterative, deterministic technique utilizing a state-variable method that converges with the proper solution without inherent numerical instabilities. The accuracy of the solution obtained depends solely on the number of terms in the field space-harmonic expansion, ensuring that the energy is always conserved [35]. Recently, a Fourier Modal Method based package was developed by Liu and Fan, and it is now freely available as Stanford Stratified Structure Solver (S⁴) software package

[36]. Compared to the commercial RCWA package GD-Calc [37], the S^4 software package offers much higher resolution due to the consideration of higher diffraction orders and also takes much less computation time [38].

The other widely used simulation approach is the three-dimensional finite-difference time domain (3D FDTD) technique [39]. In this case, a unit cell is defined by using a periodic boundary condition (PBC) and a perfectly matched layer (PML) in the four lateral and two vertical directions [40], as shown in Fig. 4(a). A Gaussian source is launched from the top of the PCS structure, with two power monitors monitoring both the reflected and the transmitted power. For practical structures, where the number of the PhC lattice period is finite, full vectorial 3D FDTD can also offer very precise and accurate simulation results. Depending on the PCS lattice parameters, either Fano resonance filters or broadband reflectors can be realized with different Q values. A set of simulated spectra for transmission and reflection is shown in Fig. 4(b) and (c), respectively. High Q filters with Q greater than 1000 can be easily obtained when a smaller r/a value is used ($r/a=0.08$, $t/a=0.34$, $a=765$ nm for high Q case here). On the other hand, a larger r/a value can lead to a lower Q filters for broadband reflector design ($r/a=0.28$, $t/a=0.347$, $a=980$ nm for low Q case here). A medium Q design was also presented with $r/a=0.19$, $t/a=0.417$, and $a=600$ nm.

The resonance modes were further verified with the field propagation plots based on 3D FDTD simulations. Snapshots of field propagation for the on- and the off-resonance modes are shown in Fig. 5(a) and (b), respectively. Note that, for the on-resonance mode (λ_1), the surface-normal incident light is reflected from the patterned PCS structure due to the coherence (in-phase) reflection, which leads to a dip in the transmission spectra. On the other hand, light at other spectra locations (off-resonance) can pass through the patterned PCS structure with maximum transmission efficiency.

Shown in Fig. 6 is the simulated dispersion plot for the square lattice PCS structure, based on a three-dimensional (3D) plane wave expansion (PWE) technique [41]. The Fano resonance modes operate above the lightline region, denoted as the shaded area. The properties of a few Fano resonance modes (ω_1 , ω_2 , ω_3) will be discussed in later sections [40]. Note also that the existence of PBG is not essential for the design of Fano resonance PCS structures.

In summary, Fano resonances in 2D PCSs arise from the coupling of in-plane discrete guide modes with the vertical continuum free-space radiation mode. Depending on the coupling strength, the output spectral resonance can vary from symmetric to asymmetric, with sharp transition and large phase change between the resonance peak and dip, which can lead to extremely high quality factor (or infinite) optical cavities, or very broadband high reflectivity reflectors. Local field enhancements associated with the Fano resonance cavity can result in strong light-matter interactions for enhanced light emission, detection, sensing, and enhanced optical forces, as well as other non-linear effects. The existence of the photonic bandgap is not essential in Fano resonance PCS structures. The flexibility in dispersion engineering and the associated slow-light effects can further enhance light-matter interactions [9,14,29,33,42–46].

3. Transfer printing techniques for Fano resonance photonics

3.1. Transfer printed semiconductor nanomembranes for Fano resonance photonics

To realize the full potential of Fano resonance photonics, high quality materials and innovative manufacturing processes are needed for (a) single or multi-layer stacking of the same or different materials heterogeneously integrated for multi-functional structures; and (b) structures on

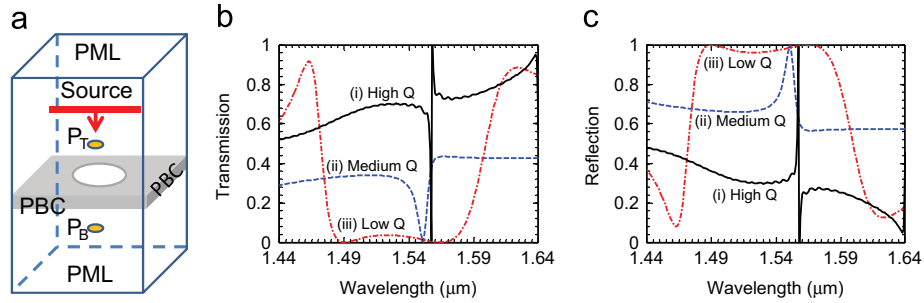


Fig. 4. Simulation and spectral control of Fano resonances in 2D PCS: (a) Schematic of an unit cell used in the simulation based on 3D-FDTD technique; Simulated (b) transmission and (c) reflection spectra for surface-normal Fano filters with different quality factors (Q s) for either highly spectrally-selective filters or broadband reflectors. Reproduced with permission from [41].

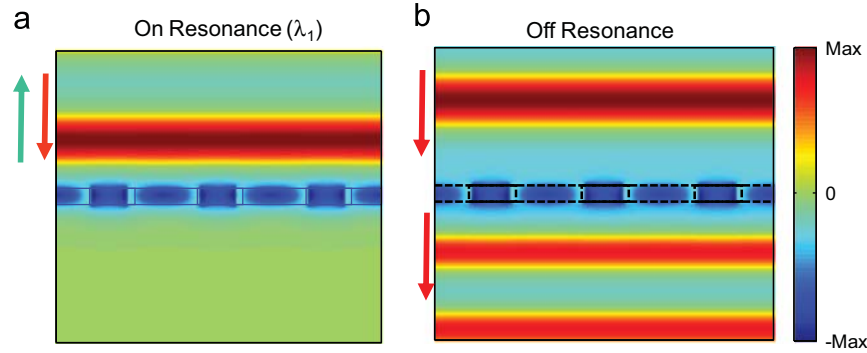


Fig. 5. Snap shots of electric field distribution of Fano filters at (a) on-resonance; and (b) off-resonance conditions. Reproduced with permission from [41].

substrates with the desired mechanical properties (rigid or flexible) and optical properties (opaque or transparent) for flexible electronics, optoelectronics, and bio-integrated structures.

In the last several years inorganic crystalline semiconductor nanomembranes (NMs, free-standing sheets that are between a nanometer and a sub-micrometer thick) have demonstrated great potential to become a disruptive technology, driven primarily by the success shown in Group IV crystalline NMs transferred and stacked onto foreign substrates, including both rigid (e.g. silicon and glass) and flexible (e.g. plastics and polymers) substrates [41,47–57]. The inherently novel electronic and mechanical properties of these sheets drive this potential. Their flexibility, conformability, biocompatibility, and transferability to other hosts, the ability to introduce strain (and thus novel properties associated with strain) in ways not possible with bulk materials, and the ability to integrate membranes of different materials because of the much better bondability of membranes than bulk material are just some of the properties driving this potential.

Traditionally epitaxial lift-off (ELO) [58–60] and wafer bonding processes [61–63] are the dominant fabrication techniques, where the native (growth) substrates are typically removed from one functional layer via a wet-etching process. Over the last few years, though, a PDMS

stamp transfer printing process, pioneered by Rogers [47,64], has been developed for the transfer of crystalline semiconductor nanomembranes (NMs) onto any substrate [47,48,57,65–67]. Based on this disruptive NM platform, a new class of photonic structures and devices has emerged [41,47,48,52,57,65–73].

Transfer printing, alternatively termed stamp printing, has several variants but all of them involve the release of the functional layers (e.g. crystalline semiconductor NMs) or structures (e.g. fabricated devices) from the starting substrate, and transfer of the functional layers or structures onto a foreign flexible substrate. High etching selectivity is desired to minimize the damage on the membrane layer. As shown in Table 1, an SiO_2 buried layer is used for the release of Si and Ge functional NM layers, while III–V material for a membrane layer should be grown on the lattice matched sacrificial layer. The generic process of transfer printing is illustrated in Fig. 7. The buried layer, which will be removed during the selective etching step, is fabricated in the form of strips or membranes (Fig. 7(a and b)). Then the sample is immersed in the etchant to undercut the buried layer (Fig. 7(c)). The top layer, then, gently falls down and bonds with the handling substrate with a weak van der Waals force (Fig. 7(d)). The bonding force varies based on how thick the buried layer is. Generally, the thicker the buried layer, the weaker the van der Waals force will be. Consequently, the membrane may float in the etchant if the buried sacrificial layer is too thick (roughly thicker than 1000 nm). In this case, special anchors need to be designed to hold the released NMs in place. The free-standing membrane layer is then ready to be transferred to the new foreign substrate (Fig. 7(d)).

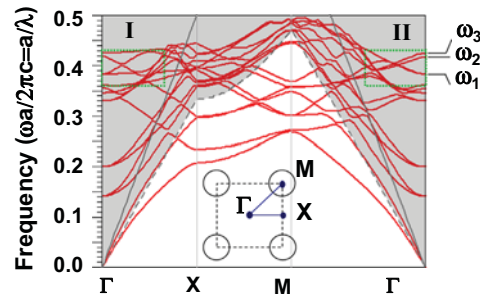


Fig. 6. Simulated dispersion characteristics for the square lattice Si PCS structure on low index glass substrate. The lattice parameters are $r/a=0.19$, $t/a=0.417$, the refractive indices of silicon and glass are 3.48 and 1.5, respectively. Reproduced with permission from [40].

Table 1
Selective wet etching for nanomembrane material release process.

Group	Membrane layer	Sacrificial layer	Etchant	Ref.
IV	Si	SiO_2	HF	[57,74]
	Ge	SiO_2	HF	[75,76]
	SiGe	SiO_2	HF	[77]
III–V	GaAs	AlGaAs	HF:H ₂ O	[78]
	InP	InGaAs	H ₂ SO ₄ :H ₂ O ₂ :H ₂ O	[79]
	InGaAsP	InGaAs	H ₂ SO ₄ :H ₂ O ₂ :H ₂ O	[80]
	GaN	Al_2O_3	Laser lift-off	[81]
Etc.	Diamond	SiO_2	HF	[82]

There are three routes for transfer printing: (1) direct flip transfer, (2) stamp-assisted transfer, and (3) transfer printing without an adhesive layer, all of which are shown in Fig. 7(e–g). Adhesive coating on the new foreign substrate is necessary for the direct flip transfer and the stamp-assisted transfer methods to hold the membrane layer in place after a transfer printing (Fig. 7(e)). UV-curable epoxies such as SU-8 (from Microchem Corp.) or NOA (Norland Products) are commonly used as the adhesive material. Transfer printing without an adhesive layer is also called “dry transfer printing”, because no adhesive chemical is involved. For the direct flip transfer method, the adhesive coated substrate is directly attached to the substrate with a membrane layer (Fig. 7(e1)) and then detached (Fig. 7(e2)). For stamp-assisted transfer, the membrane layer is picked up by an elastomeric stamp (Fig. 7(f1)) and then transferred and adhered onto the new foreign substrate (Fig. 7(f2)). After membrane layer transfer with either method, adhesive layer should be exposed to UV light, so that the transferred membrane layer will be permanently adhered to the new foreign substrate (Fig. 7(f3)). For dry transfer printing, the membrane layer is picked up by an elastomeric stamp (Fig. 7(g1)), as with the stamp-assisted transfer method, but the membrane layer is released using kinetically controlled adhesion of the elastomeric stamp (Fig. 7(g2–g3)). A more detailed description of the mechanisms of dry transfer can be found elsewhere [64]. Basically, fast membrane peeling speed is required for the pick-up and slow peeling speed is needed for the release. Both the stamp-assisted transfer and the dry transfer method are non-flipped transfer methods. Poor transfer quality and yield can be caused by slow printing speed or particles on the substrate during the dry transfer. Precise machine controlled dry transfer[83,84] or dry transfer with a specially designed elastomeric stamp to reduce the surface energy between the membrane layer and the stamp [85] can increase the

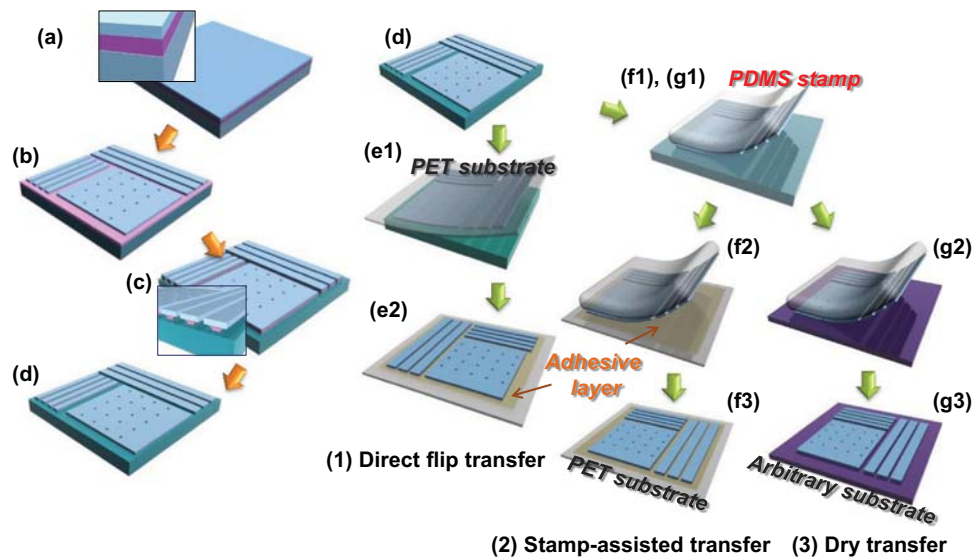


Fig. 7. Generic process of a transfer printing: (a and b) make a pattern on an SOI wafer, (c) immerse in the etchant for undercut, (d) membrane layer gently falls down after buried oxide layer is completely removed, (e1) adhesive layer coated plastic substrate is flipped and membranes picked (e2) completion of the direct flip transfer, (f1) pick up membranes by the elastomeric stamp (f2) transfer printing on the adhesive layer coated flexible substrate, (f3) completion of the stamp-assisted transfer, (g1) pick up membranes with fast peeling speed, (g2) release membrane with slow peeling speed, (g3) Application of additional annealing procedure to enhance the bonding force.

transfer yield. Despite this limitation of dry transfer, it is a very useful and practical technique for applications that need to stack several delicate layers or have an ultra-clean interface without any adhesive layers [64,80,86].

By releasing high-quality flexible materials from SOI and other source substrates and transfer-printing them to a new host substrate, integration of dissimilar material systems becomes feasible on both rigid and flexible substrates. This is possible with individually optimized material structures, energy-efficient and flexible integration process, and intelligent functions [41,47,56,64,67,68,77,85,87,88]. The transfer printing steps can also be repeated to produce stacked multi-layer photonic structures [89]. Besides Si [90], many materials including III-V semiconductors [79,91], metals [92], and organic semiconductors [93] are all amenable to transfer printing processing.

Using transfer printed NMs on flexible substrates, various high performance photonic and optoelectronic devices have been demonstrated, including flexible photodetectors, LEDs, solar cells, flexible Si Fano resonance filters, and mostly significantly, fast flexible electronics, with record speed RF performances due to the high electron mobility in single crystalline semiconductors [75,77,94–96]. Many excellent results have also been reported on the unique electronic, photonic, thermoelectronic, and mechanical properties associated with this new class of inorganic flexible semiconductor membrane material systems. To improve the yield of the printing transfer process, Xu et al. [97] reported an innovative stamp printing technique with an adhesion controllable suspended configuration. To address the alignment challenge of the large area flexible substrate, a local alignment scheme in combination with more accurate Si-NM transfer measures for minimizing alignment errors were reported. Using a $1\ \mu\text{m}$ channel alignment for the Si-NMs on a soft plastic substrate, thin film transistors with a record speed of 12 GHz maximum oscillation frequency were demonstrated. Recently, another record for fast flexible transistors was set by the strained Si/SiGe/Si-NMs transferred onto flexible substrates, with a maximum oscillation frequency of 15 GHz [77]. These results indicate the great potential of properly processed Si-NMs for high-performance flexible optoelectronics [55].

High quality photonic crystal (PhC) structures have been successfully transferred onto PET substrates using NM transfer processes, as shown in Fig. 8. PhC air hole structures were first

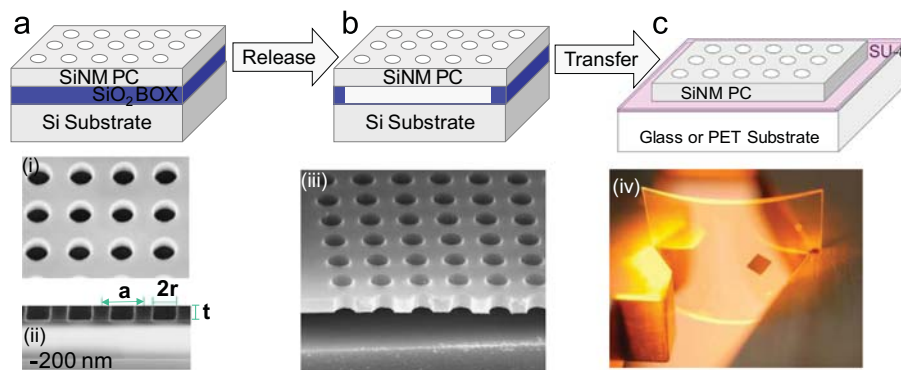


Fig. 8. Modified process for air hole PhC NM structure transfer. Single layer NM pattern (a), release (b), and transfer (c) process, along with experimental results (bottom): (i) SEM image of top and (ii) cross-sectional view of patterned Si-NM on SOI, (iii) SEM images of patterned Si-NM after BHF etching of BOX layer underneath the pattern area, (iv) micrograph of a 3×3 mm patterned NM transferred onto 1×1 in. flexible PET substrate. Reproduced with permission from [41].

fabricated with the target wavelength of 1550 nm on 260-nm thick silicon-on-insulator (SOI) wafers using e-beam lithography and plasma dry-etching processes. Shown in Fig. 8(a) are a schematic (top) and scanning electron micrographs (SEMs) of the patterned PhC SOI structures (bottom). The patterned PhC SOI structures were subsequently immersed in aqueous diluted HF solution (49% HF:DI water=1:4) for several hours to selectively etch away the BOX (buried oxide) layer (Fig. 8(b)). Once the top patterned PhC Si-NM was completely released, it was rinsed in DI water and transferred onto PET plastic substrates (Fig. 8(c)). A micrograph is shown in Fig. 8(iv), where a large piece of NM was transferred onto a flexible (curved) PET substrate.

3.2. Comparison with other epitaxial lift-off (ELO) and wafer bonding processes

One can form a crystalline membrane using various methods. Among them, the epitaxial lift-off (ELO) process [58,98] and the laser lift-off (LLO) process are the most common ways to create thin membranes from the bulk source substrates [59,60]. The ELO process is more common than the LLO, since most of materials are available with etching selectivity, as shown in Table 1. The major difference between the LLO process and the ELO process is the use of external energy to change the interface composition. LLO is only used to create a single crystalline GaN membrane layer from the GaN/Sapphire structure as a lighting device. The substrate used for LLO process should be firmly glued to the source substrate to avoid unwanted damages during the lift-off process, often caused by difference in strain between the GaN and Sapphire layers. Therefore, only the transfer printing with an adhesive layer can be used for the

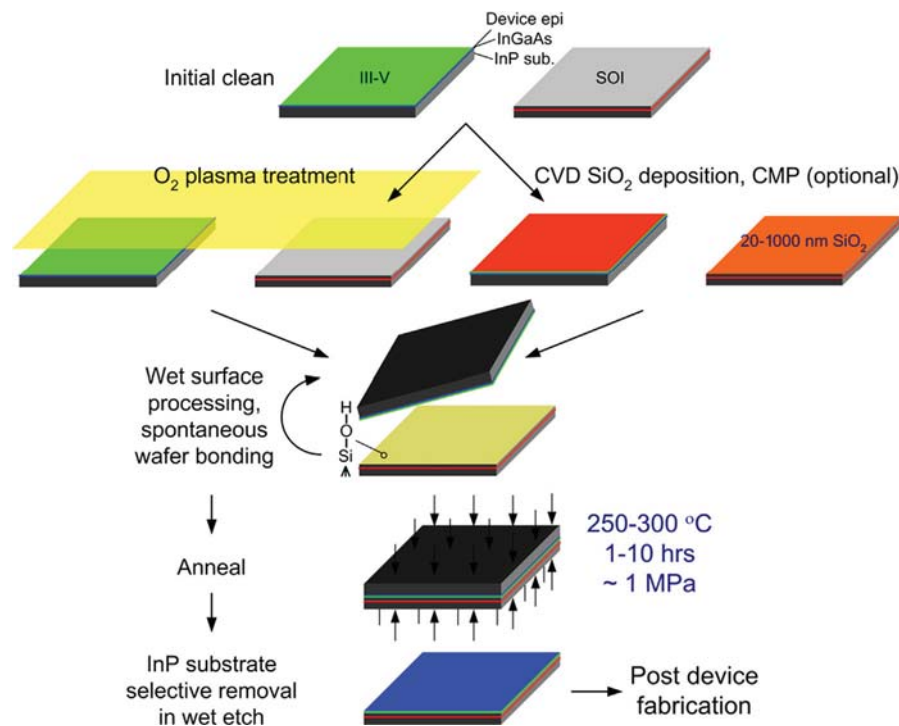


Fig. 9. Schematic process flow for O₂ plasma-assisted bonding and SiO₂ covalent wafer bonding. Reproduced with permission from [110].

LLO process [81] or one must resort to a multiple layer transfer process, making the process more difficult. On the other hand, as shown in the previous section, the thin membrane created by the ELO will gently fall down and bond to the handling substrate by weak Van der Waals force. This weak bonding enables the application of all of the transfer printing methods, in addition to the precisely aligned transfer printing of free standing membranes.

Among the different layer transfer methods, a wafer bonding has been widely used to bond two different layers for device/circuit integration [61–63,99–105] or to form a unique device platform (such as a Silicon-on-Insulator or Germanium-on-Insulator) [106,107]. Wafer bonding techniques include wafer-to-wafer bonding, wafer-to-piece bonding and wafer-to-wafer bonding with an adhesive layer, etc.

The integration of different optical functions on a photonic IC fabricated using high-yield wafer-scale technologies is expected to result in systems-on-a-chip that outperform their discrete and die-level integrated counterparts in compactness, performance, complexity, and cost. Generally these systems contain both active functions (amplification, switching, modulation, light emission, and detection) and passive optical waveguides, so different materials need to be integrated into a single system [108]. Roelkens et al. [109] presented a review on heterogeneously integrated III–V on SOI for the realization of near infrared light sources on a silicon waveguide platform that are suitable for inter-chip and intra-chip optical interconnects. Two wafer bonding technologies were used to realize the III–V/SOI integration: one based on molecular wafer bonding and the other based on DVS-BCB adhesive wafer bonding, for the realization of micro-disk lasers, Fabry–Perot lasers, DFB lasers, DBR lasers and mode-locked lasers on the III–V/SOI material platform.

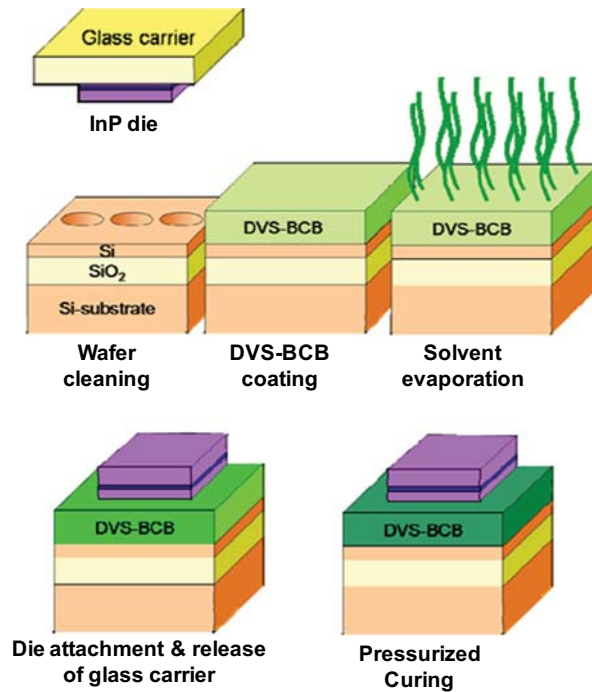


Fig. 10. Overview of the DVS-BCB die-to-wafer bonding process. Reproduced with permission from [110].

Another review by Liang et al. [110] presented detailed discussions and comparisons of these two types of wafer bonding techniques. Fig. 9 shows the schematic process of the O_2 plasma-assisted bonding and SiO_2 covalent wafer bonding. For this process, it is critical to have very smooth (RMS roughness < 0.5 nm) hydrophilic surfaces [111,112]. On the other hand, adhesive bonding can also be used to transfer III–V epitaxial layers onto an SOI waveguide circuit, with relaxed constraints on surface roughness [113]. The process is shown in Fig. 10. Various adhesives can be used, including polyimides, epoxies, spin-on-glasses, photoresist, SU-8, DVS-BCB, etc. [103]. Both methods can generate strong, low stress and stable bonding within a process requiring low temperatures. Compared to direct bonding, adhesive bonding does not require special surface treatment and is able to tolerate some surface topography, depending on interfacial polymer chemistry and layer thickness. This results in a relatively simple process. Direct bonding, however, has the inherent advantage of better integration proximity, which benefits optical coupling and heat transportation between dissimilar materials for the hybrid III–V-on-Si photonic integration platform in particular, provided that the outgassing problem is sufficiently minimized or eliminated [110].

Compared to the wafer bonding techniques, the NM transfer printing process offers better material and host substrate versatility, including much better bonding strength, greatly enhanced thermal expansion coefficient mismatch tolerance, and much more flexibility in the material distribution and on the host substrate [74,85,114,115]. It is better suited for applications where different pieces of material need to be integrated to form multi-layer stacked configurations, such as the formation of laser cavities [57]. We expect that all techniques reported here will co-exist and that the choice of the specific process will depend on the device and system integration architectures.

4. Fano resonance photonic crystal filters

4.1. Single layer filters

As an example of how one might apply the theory in Section 2, we can construct single-pole filters using an individual resonance. For $r=1$ and therefore $t=0$, (Eq. (10)) gives the

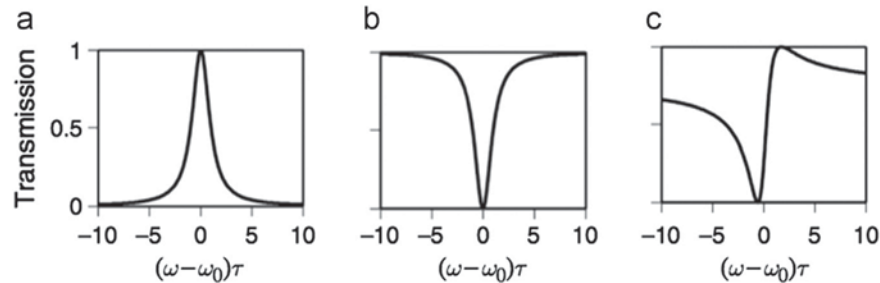


Fig. 11. Single-pole filter lineshapes. ω_0 and $\gamma=1/\tau$ are the center frequency and width of the resonance. (a) A bandpass filter constructed by a resonance imposed on a total reflection background. (b) A notch filter constructed by a resonance imposed on a zero reflection background. (c) A Fano filter constructed by a resonance imposed on a partial reflection background.

transmission spectrum

$$T = \frac{(1/\tau)^2}{(\omega - \omega_0)^2 + (1/\tau)^2} \quad (11)$$

which exhibits a Lorentzian peak and such a configuration functions as a band-pass filter (Fig. 11 (a)). For $r=0$ and therefore $t=1$, the transmission spectrum

$$T = \frac{(\omega - \omega_0)^2}{(\omega - \omega_0)^2 + (1/\tau)^2} \quad (12)$$

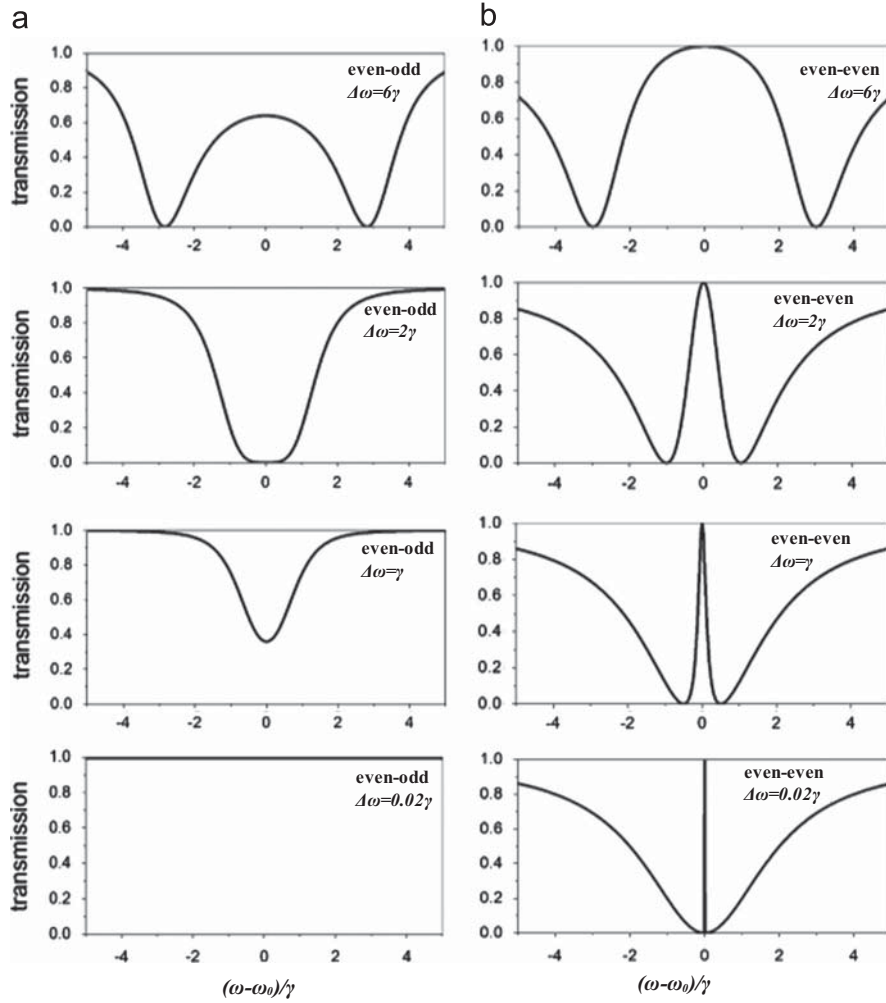


Fig. 12. Double-pole filter lineshapes resulting from two resonances. ω_0 and $\gamma=1/\tau$ are the center frequency and width of the resonances. $\Delta\omega$ is the frequency difference between the two resonances. (a) Transmission spectra through two orthogonal, even and odd, resonances. When $\Delta\omega \gg \gamma$, the system behaves in essence as two separate Lorentzian filters. At $\Delta\omega=2\gamma$, the structure is a flattop filter. When $\Delta\omega \ll \gamma$, the structure is an all-pass filter. (b) Transmission spectra through two nonorthogonal, both even, resonances. The structure exhibits electromagnetically induced transparency (EIT) lineshapes. Reproduced with permission from [30].

features a band-rejection filter (Fig. 11(b)). With all intermediate background parameters being $0 < r < 1$ and $0 < t < 1$, the transmission spectrum given by Eq. (10) exhibits sharp asymmetric Fano lines (Fig. 11(c)). Many aspects in the spectral response can be controlled if appropriately designed [116]. Although we have been dealing with planewaves in the temporal coupled-mode theory discussions, similar phenomena can be seen with focused illumination as well [117].

To construct double-pole filters, one should introduce an additional resonance in the photon transport through PCSs. This can be achieved by coupling two PCSs, which we will discuss later, or by using two resonances in a single PCS. A variety of double-pole filters can be constructed depending on, for example, the symmetry of the two resonances and the difference in frequency between the two resonances compared to the width of each individual resonance. In Fig. 12, we show graphs corresponding with different configurations. Fig. 12(a) is a collection of graphs displaying photon transport through two orthogonal resonances, in addition to the direct pathway. Fig. 12(b) displays what occurs when the two resonances are nonorthogonal. Because it is relatively difficult to construct two nonorthogonal resonances in a single layer PCS, we will focus on the orthogonal case in this section, and continue the discussion of the nonorthogonal case in the next section, which is on coupled double-layer filters.

Relying on two resonances with opposite mirror symmetries in a single PCS, the structure can serve as an all-pass transmission or a flat-top reflection filter [45]. To have two resonances in the vicinity of a signal frequency, one needs to choose appropriate geometrical parameters for the photonic crystal slab. Fig. 13 shows such a configuration.

Because the resonances are orthogonal, similar to Eq. (1), the complex amplitude transmission coefficient can be written as

$$t = 1 - \frac{\gamma_{\text{even}}}{i\omega - i\omega_{\text{even}} + \gamma_{\text{even}}} - \frac{\gamma_{\text{odd}}}{i\omega - i\omega_{\text{odd}} + \gamma_{\text{odd}}} \quad (13)$$

When $\gamma_{\text{even}} = \gamma_{\text{odd}} = \gamma$, $\omega_{\text{even}} = \omega_{\text{odd}} = \omega_0$, Eq. (13) can be simplified to

$$t = \frac{i(\omega - \omega_0) - \gamma}{i(\omega - \omega_0) + \gamma} \quad (14)$$

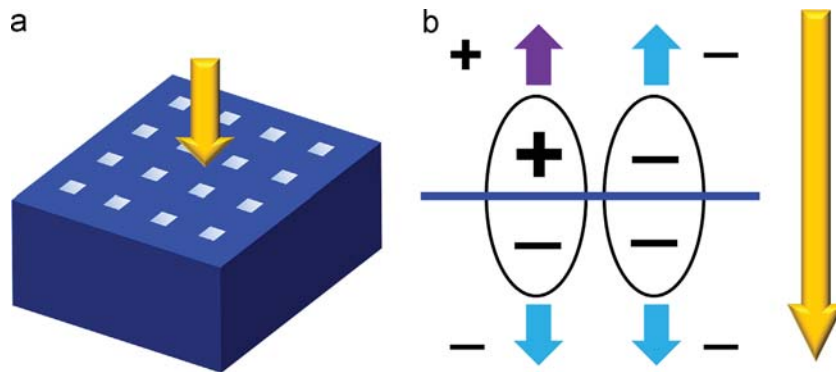


Fig. 13. (a) Photonic crystal slab structure consisting of a square lattice of air holes introduced into a high-index dielectric slab. The slab is $2.05a$, thick and the radius of the holes is $0.12a$, where a is the lattice constant. The arrow represents the direction of the incident light. (b) Schematic of a theoretical model for a resonator system that supports two resonant modes with opposite symmetry with respect to the mirror plane perpendicular to the incident light. Reproduced with permission from [45].

and the photonic crystal slab becomes an all-pass filter. The intensity transmission is uniform for both on and off resonances. However, the phase delay varies from 0 to 2π in the vicinity of the resonance. This can be realized in the structure if we choose a dielectric constant of 10.07, as shown in Fig. 13. The all-pass transmission and the phase delay spectra are shown in Fig. 14. The theoretical derivation (Eq. (14)) is verified by FDTD simulations [45].

When $\gamma_{\text{even}} = \gamma_{\text{odd}} = \gamma$, $|\omega_{\text{even}} - \omega_{\text{odd}}| = 2\gamma$, Eq. (13) becomes

$$T = |t|^2 = \frac{(\omega - \omega_0)^4}{(\omega - \omega_0)^4 + 4\gamma^4} \quad (15)$$

where $\omega_0 = (\omega_{\text{even}} + \omega_{\text{odd}})/2$ and flat-top reflection is achieved in the vicinity of the resonance. This can also be realized in the structure shown in Fig. 13, if we choose a dielectric constant of 10.9. In Fig. 15, we plot the transmission spectrum. The theoretical derivation (Eq. (15)) is again verified against FDTD simulations [45].

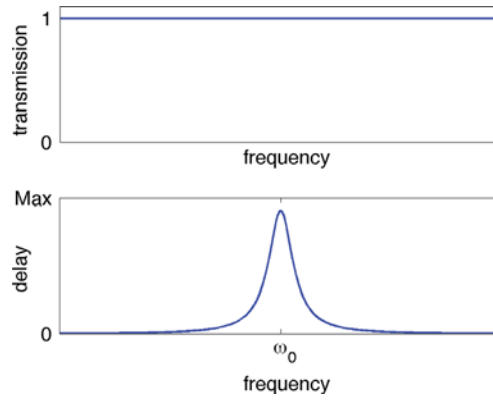


Fig. 14. Spectral response functions (intensity transmission and group delay) for the one slab structure in Fig. 13 with a dielectric constant of 10.07.

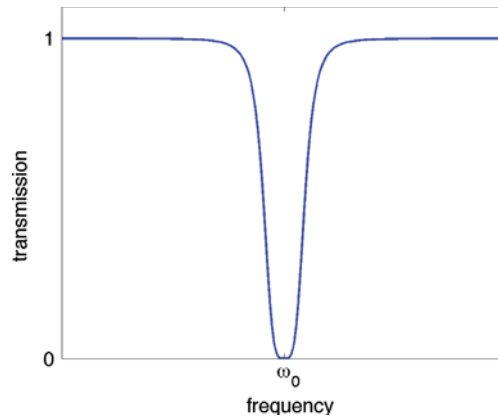


Fig. 15. Intensity transmission for the one slab structure in Fig. 13 with a dielectric constant of 10.9.

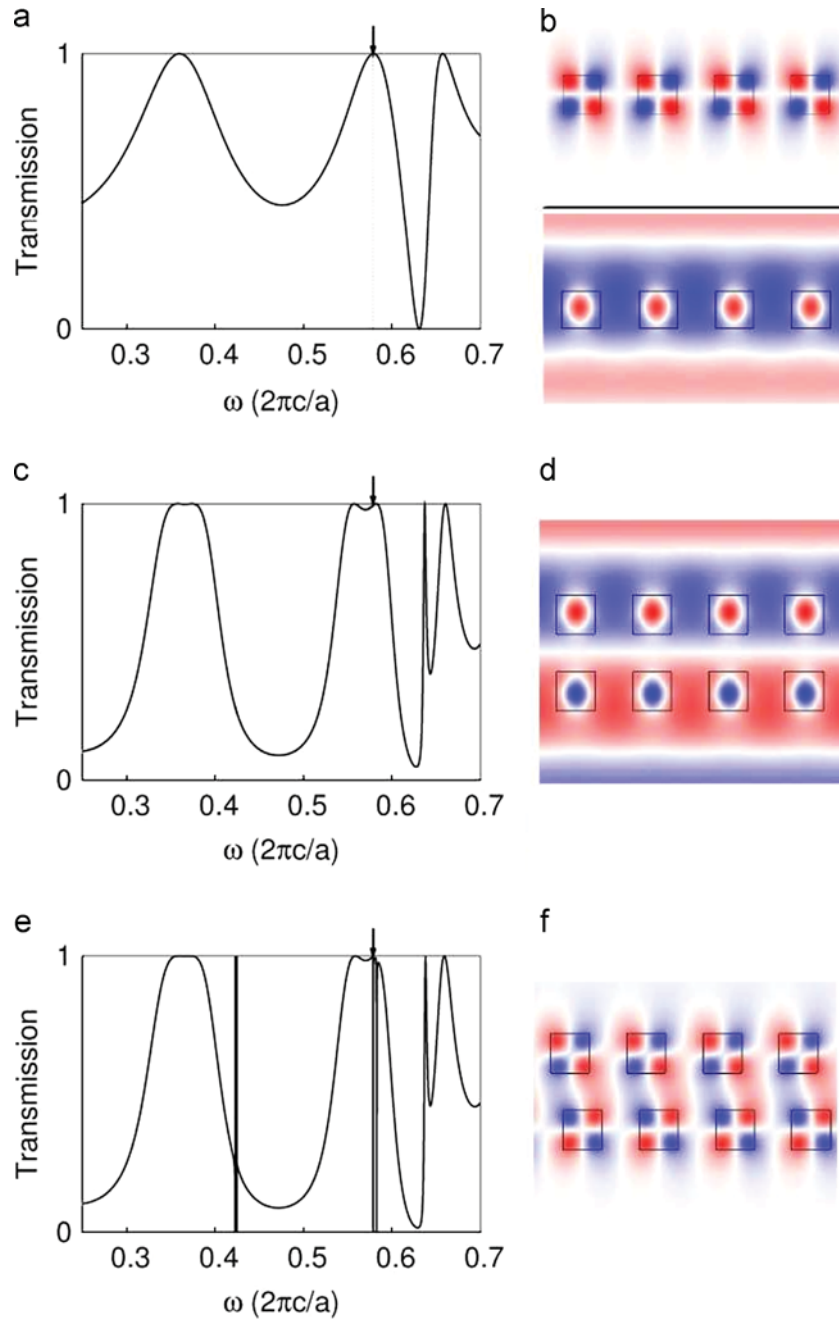


Fig. 16. Dark states in a two photonic crystal slab system that arise from coupled dark resonances from single slabs. (a) Single slab transmission spectrum. (b) Mode profile at the dark state frequency (top) and field profile at the frequency indicated by the arrow in (a). (c) Double slab transmission spectrum for $d=0.5a$, where d is the spacing and a is the lattice constant. (d) Field profile at frequency indicated by the arrow in (c). (e) Double slab transmission spectrum for $\Delta x=0.15a$, where Δx is the lateral displacement. (f) Field profile at lowest frequency resonance from (e). Reproduced with permission from [120].

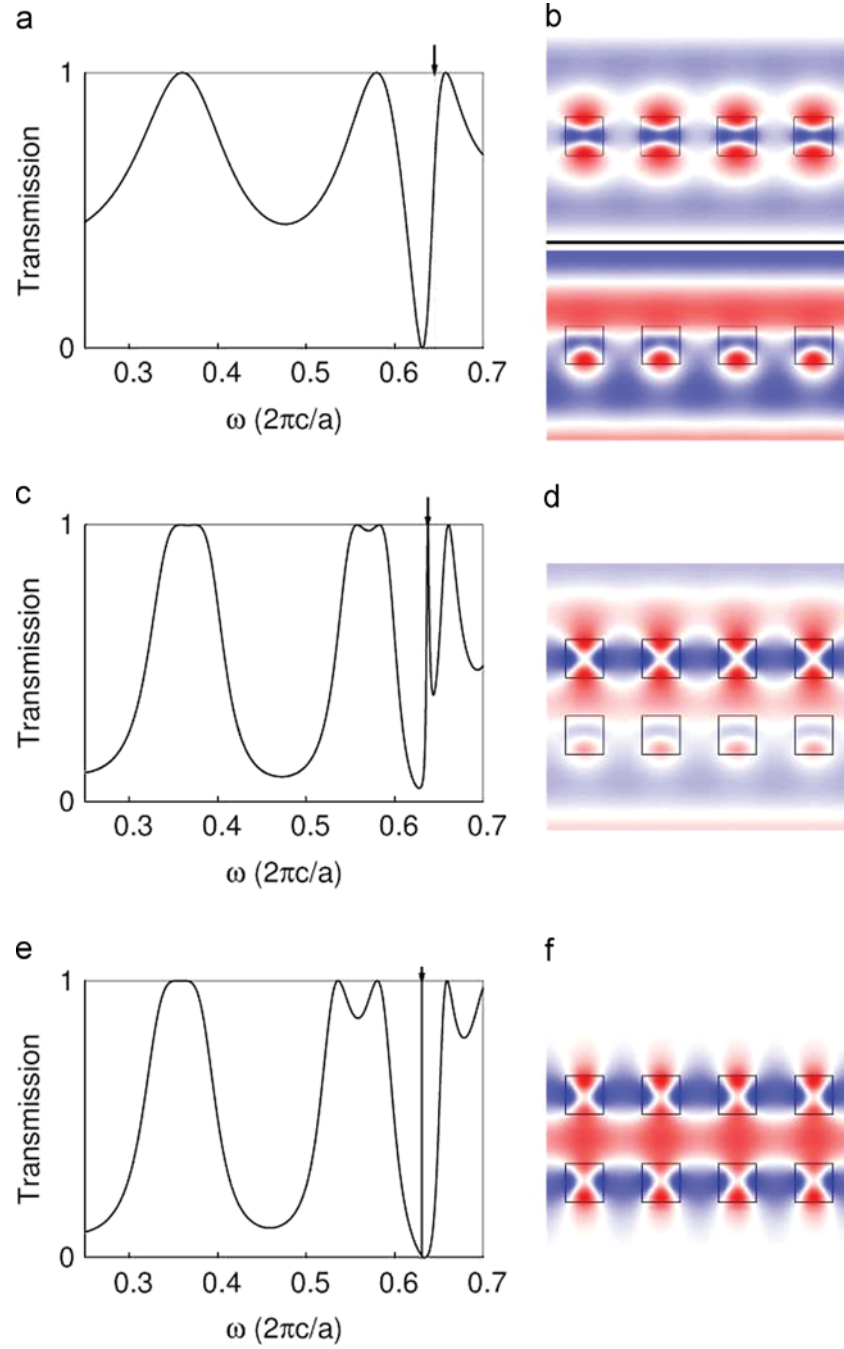


Fig. 17. Dark states in a two photonic crystal slab system that arise from coupled bright resonances from single slabs. (a) Single slab transmission spectrum. (b) Mode profile at the dark state frequency (top) and field profile at the frequency indicated by the arrow in (a). (c) Double slab transmission spectrum for $d=0.5a$, where d is the spacing and a is the lattice constant. (d) Field profile at frequency indicated by the arrow in (c). (e) Double slab transmission spectrum for $d=0.65a$. (f) Field profile at peak of resonance in (e). Reproduced with permission from [120].

4.2. Coupled double layer filters

All the filters we have shown so far are constructed on a single PCS. These filters can also be made with two coupled PCSs. This can be assumed because with additional layers, PCS filters offer higher quality factor and dispersion engineering capabilities [38]. For example, by spacing

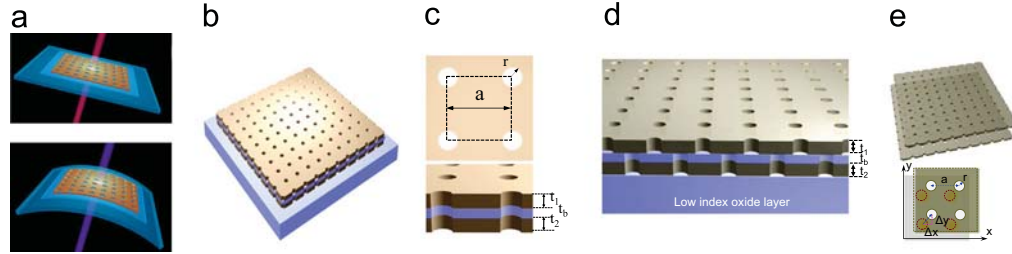


Fig. 18. Schematics of Fano resonance PCS filter configurations: (a) single layer PCS on glass (top) or flexible (bottom) substrates; (b) double-PCS Fano filter 3D sketch; (c) key parameters defined for the square lattice double-layer PCS filter including lattice constant (a), air hole radius (r), thin oxide buffer layer thickness (t_b), and two single layer PCS layer thicknesses (t_1 and t_2); (d) 3D close-up view of double-PCS Fano filters with lattice displacement; and (e) Illustration and definition of key design parameters, including lattice displacement (Δx , Δy) between two layers.

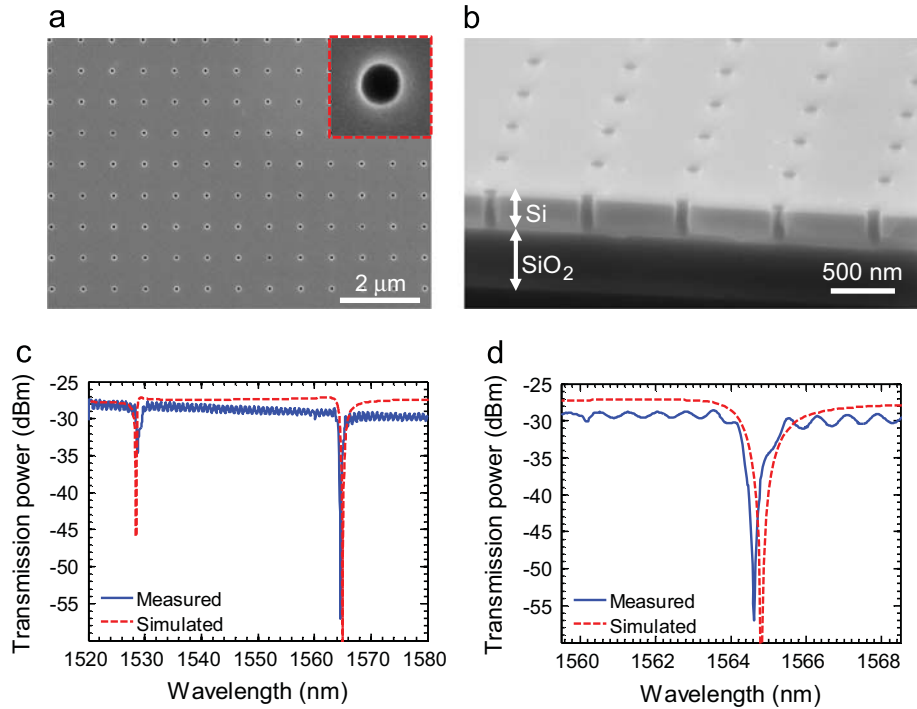


Fig. 19. Experimental results for Design S_1 : (a) top and (b) cross-section views of fabricated single-layer PhC Fano resonance filters on oxide buffer; (c) measured (blue solid line) and simulated (red dash line) transmission spectra for the fabricated single-layer PhC Fano resonance filter transferred on glass substrates; and (d) enlargement of (c) over the second dip ($\lambda = 1564.62$ nm) region. Reproduced with permission from [38].

two PCSs together closer than the wavelength, one can construct a structure for which the transmission is highly sensitive to the distance between the slabs, providing single-pole Fano and Lorentzian filters [118], as well as double-pole all-pass and flat-top filters [119].

It is relatively straightforward to couple two resonances with the same symmetry in double layer structures. Because the resonances are non-orthogonal, the transmission coefficient can no

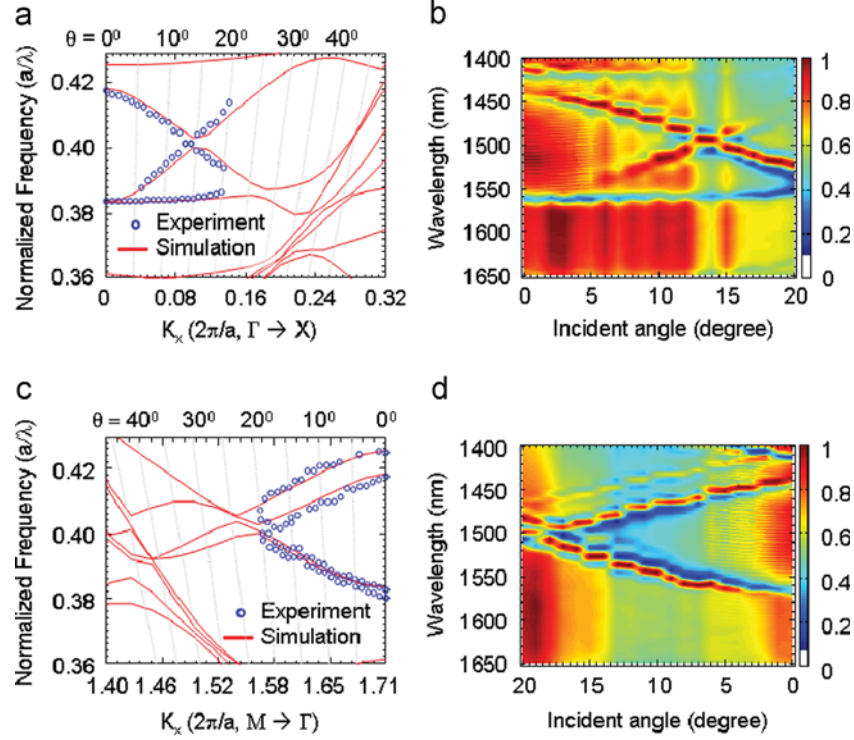


Fig. 20. (a and c) Simulated dispersion plot (red lines) zoomed-in for the regions (I and II) shown in Fig. 6 along (Γ – X , Γ – M) directions, along with measured Fano resonances (blue dots) for different incident angle θ with (a) $\phi=0^\circ$ and $\Psi=0^\circ$, and (c) $\phi=45^\circ$ and $\Psi=45^\circ$. The straight gray lines represent the relationships between the normalized frequency and the normalized wave-vectors along (Γ – X , Γ – M) directions. (b and d) Measured transmission intensity contour plots for angle-dependent transmissions at different incident angles θ with (b) $\phi=0^\circ$ and $\Psi=0^\circ$, and (d) $\phi=45^\circ$ and $\Psi=45^\circ$. Reproduced with permission from [40].

Table 2

Key design parameters and Q 's for the selected single- (S_1 – S_3) and double- (D_1 – D_3) layer filters.

Unit	a nm	r/a	t_1 nm	t_2 nm	t_b nm	Q
S_1	765	0.08	260	–	–	4100
S_2	765	0.1	260	–	–	1900
S_3	780	0.08	260	–	–	4500
D_1	1000	0.2	230	230	160	1.2×10^4
D_2	1000	0.08	230	230	20	2.2×10^4
D_3	1000	0.05	230	230	20	9.8×10^4

longer be intuitively written as a sum of the three pathways (two resonances plus the direct pathway) as in Eq. (13). Instead, one needs to solve the more general temporal coupled-mode equations [30]. The amplitude transmission coefficient can be calculated as

$$t = t_d \mp \frac{(r_d \pm t_d)[\gamma_1(i\omega - i\omega_1) + \gamma_2(i\omega - i\omega_2)]}{(i\omega - i\omega_1 + \gamma_1)(i\omega - i\omega_2 + \gamma_2) - \gamma_1\gamma_2} \quad (16)$$

where the top signs are used when both modes are even, and the bottom signs are used when both modes are odd. In Fig. 12(b), we assume that both modes are even, and that $\omega_1 = \omega_0 - \Delta\omega/2$, $\omega_2 = \omega_0 + \Delta\omega/2$, and $\gamma_1 = \gamma_2 = \gamma$. The transmission behavior in Fig. 12(b) resembles that of electromagnetically induced transparency (EIT). At the resonant frequencies ω_1 and ω_2 , the transmission is zero regardless of the spacing between the two resonant frequencies; while at ω_0 , the transmission is at unity. This configuration was demonstrated using coupled PCSs [119].

In coupled PCSs, there exists extra opportunity to engineer dark resonances [120]. A dark resonance is a guided resonance decoupled from particular free space radiation modes due to symmetry mismatch. We also refer to externally excited guided resonances as bright resonances. A dark resonance in coupled PCSs can arise from the coupling of dark resonances or bright resonances in individual slabs.

For two PCSs that each possess a dark resonance, bringing them close to each other allows their resonances to couple. If both slabs are aligned such that the proper symmetries are preserved, these coupled dark resonances remain dark. If we shift the relative position of these

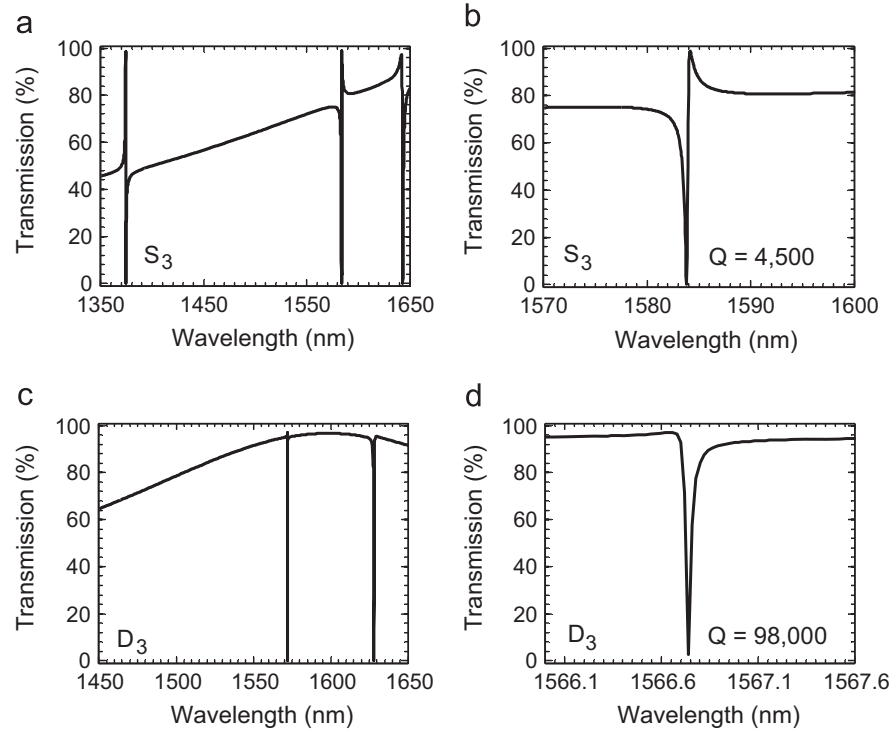


Fig. 21. Simulated transmission spectra for (a and b) single- and (c and d) double-layer Fano resonance PhC filters, where (b) and (d) are enlarged plots of (a) and (c), respectively. The design parameters are summarized in Table 1 for Cases S₃ and D₃, respectively. Reproduced with permission from [38].

two slabs to break the symmetry, these coupled guided resonances are externally excited and become bright. This will result in two Fano resonances in close proximity, and the quality factors depend strongly on the lateral displacement. This type of dark resonance is illustrated in Fig. 16.

It is also possible to couple two bright resonances together to make them dark. For a pair of PCSs each with a bright resonance, we can decouple them from radiation modes by placing a Fabry–Perot resonance between the two slabs. At a frequency where the reflectivity of each individual slab is at unity, the bright resonances lose access to external radiation. This type of dark resonance is illustrated in Fig. 17.

4.3. Fano resonance filter configurations

4.3.1. Single layer Fano resonance filters

Following initial experimental demonstrations [28] and theoretical investigations [9,45,121], 2D PCS Fano resonance filters have been reported from a few other groups [9,33,44,122].

Over the last few years, based on the PDMS transfer printing techniques, many different types of Fano resonance filters have been reported, based on single- or double-layer PCSs on Si, glass, and flexible substrates (Fig. 18). The key lattice parameters are the air hole radius (r), the lattice period (a), thicknesses for the top (t_1) and bottom Si PhC layers, (t_2) and the oxide buffer layer in between (t_b).

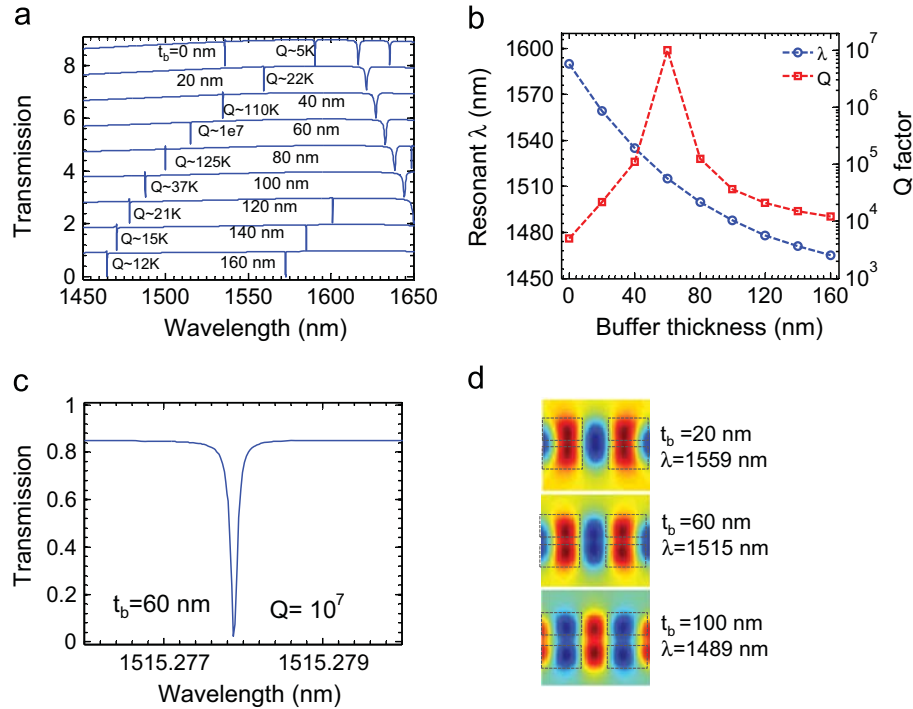


Fig. 22. Simulation results for Design D₂ with different buffer layer thicknesses t_b : (a) transmission spectra with different t_b from 0 nm to 160 nm; (b) High Q resonant wavelengths and the corresponding Q values for different buffer thicknesses t_b ; (c) zoom-in spectrum for the buffer thickness $t_b = 60$ nm and filter Q of 10,000,000; and (d) simulated E-field intensity profile at resonant wavelengths for three different t_b values, where $t_b = 60$ nm representing the highest Q condition for this design. Reproduced with permission from [38].

Yang et al. [40] reported the first experimental surface-normal Fano filters based on transferred silicon nanomembranes on glass and on flexible PET substrates. Subsequently, with improved designs and processes, single layer PCS Fano filters have been demonstrated with much improved performance. Shown in Fig. 19(a) and (b) are scanning electron microscope (SEM) images of the fabricated single layer Fano filters on glass substrate. The measured (blue solid line) and simulated (red dashed line) transmission spectra are shown in Fig. 19(c), with enlarged images shown in Fig. 19(d). Two transmission dips were found, at 1529.88 nm and 1564.62 nm. For the 1564.62 nm dip, the Q value was 1737, with a 26 dB extinction ratio.

The angle and polarization properties of these filters have been investigated in detail by Qiang et al. [40] and Chen et al. [96], focusing on measurement and simulated dispersion properties. Detailed analysis of the angle dependent Fano resonant mode dispersion properties are presented in Fig. 20. Following the conventional definition, the light incident angles are specified by two polar angles, the colatitude angle θ (an angle from the surface-normal direction) and the azimuth angle ϕ (an angle from the positive x -axis to the orthogonal projection of the incident beam in the x - y plane) [123]. The incident beam with the wave-vector \mathbf{k} was kept within the Γ - X direction in the k -space, i.e., for the case shown in Fig. 20(a) with $\phi = 0^\circ$, the momentum vector k_x relates to the normalized momentum $k_{\Gamma-X}$ along the Γ - X direction as $k_x = k_{\Gamma-X}(2\pi/a) \cos \phi$. Thus the normalized frequency (a/λ) can be related to the normalized momentum $k_{\Gamma-X}$ in the dispersion plot as $k_{\Gamma-X} = (a/\lambda) \sin \theta$.

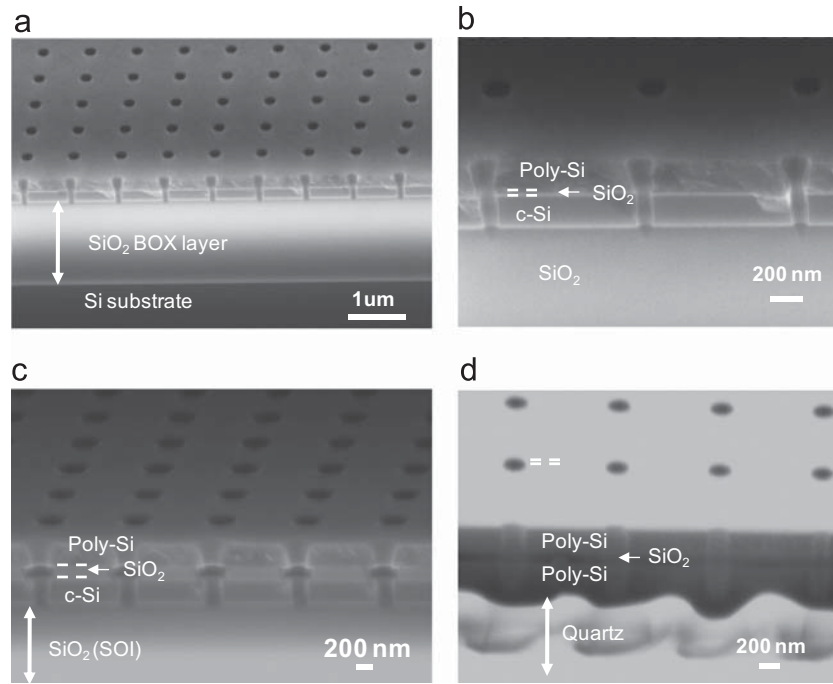


Fig. 23. Cross-sectional SEM images for fabricated double-layer PhC Fano resonance filters based on Design D₂ parameters: (a–c) double-layer PhC structure was formed by poly-Si deposition on top of the SOI substrates; and (d) double-layer PhC structure was formed by two steps of poly-Si deposition on quartz substrates. Notice the oxide buffer thicknesses are 20 nm, 160 nm, and 20 nm, for cases (b), (c), and (d), respectively. Reproduced with permission from [38].

A set of straight lines can be superimposed on the normalized dispersion plot along the Γ - X direction, as shown in Fig. 20(a), which is an amplified plot of region I shown in Fig. 6. The measured Fano resonant modes were normalized and plotted in Fig. 20(a) (blue circles). Excellent agreement was achieved between the experimental and simulation results. The transmission intensity contour plots for the measured angle-dependent transmission spectra, with $\phi=0^\circ$, are also shown in Fig. 20(b), where the intensity dips/peaks are shown in blue and red. The intensity contour plot clearly resembles the spectra shifting behavior shown in Fig. 20(a).

Following a similar procedure, the measured transmission results shown in Fig. 20(b), with $\phi=45^\circ$, were analyzed such that wave vector k lies in the Γ - M plane, with results shown in Fig. 20(c) and (d). Again, the experimental and simulation results agree very well. It was confirmed that angle-independent filters are feasible based on the dispersion engineering of the Fano resonances in PCS. Details can be found in a short review by Zhou et al. [41]

4.3.2. Double layer Fano resonance filters

On the other hand, much higher Q 's can be achieved in coupled double-layer Fano resonance PhC structures. Liu and Fan et al. [120] reported earlier that much higher Q 's can arise from the coupled dark states in double-layer stacked PCS structures. Suspended double-layer PCS filters

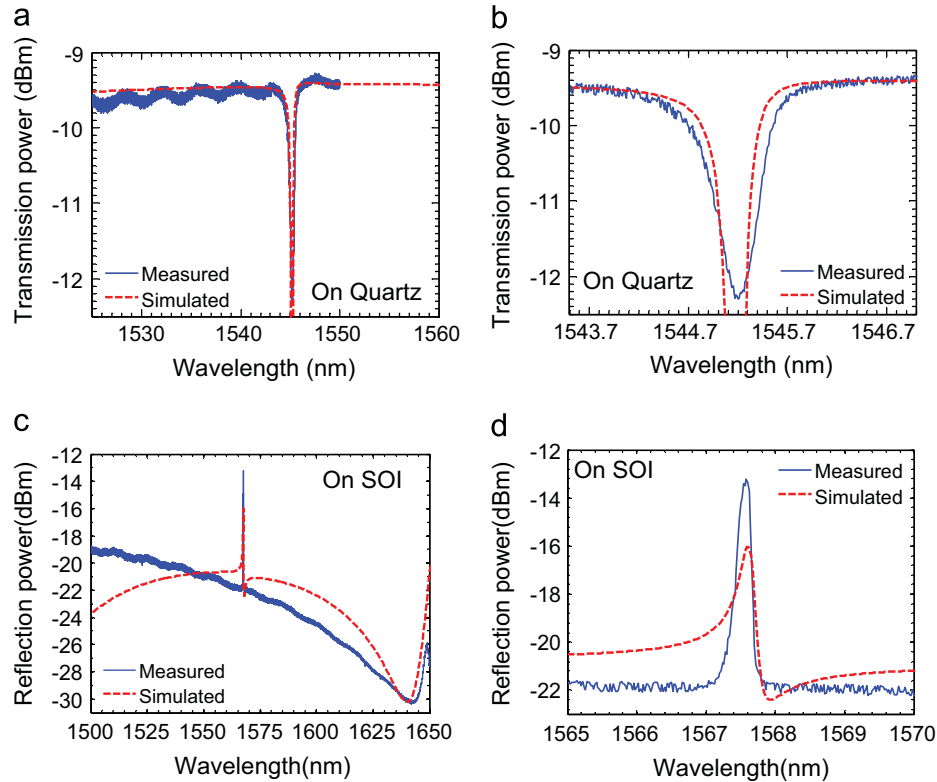


Fig. 24. (a and b) Measured (blue solid line) and simulated (red dash line) transmission spectra for the double-layer PhC Fano resonance filters on quartz; and (c and d) measured (blue solid line) and simulated (red dash line) reflection spectra for the double-layer PhC Fano resonance filters on SOI. (b) and (d) are magnifications of (a), (c), respectively. Reproduced with permission from [38].

have also been experimentally demonstrated in GaAs, [124] InP [125], and Si [38] materials. Both single- and double-layer Fano resonance Si PhC filters were designed and optimized for high Q 's around 1550 nm on the spectral band. Shown in Table 2 are key design parameters for a few optimized design structures, where S_1 – S_3 are for single-layer designs and D_1 – D_3 are for double-layer designs. Notice that the Fano filter Q increases from 4,500 for single layer filter to over 98,000 for a double-layer filter. Shown in Fig. 21 are the simulated transmission spectra for Designs S_3 and D_3 , with Q 's of 4500 and 98,000 respectively [38].

Additionally, it was predicted that the double-layer PhC structure could produce an extremely high Q mode (infinite in theory), by varying the coupling condition between two PhC layers. [120] Based on the Design D_2 parameters, transmission spectra were simulated by varying the buffer layer oxide thickness t_b .

For the double-layer structure, the simulated transmission spectra are plotted in Fig. 22(a), with oxide buffers ranging from 0 to 160 nm thick. With the increased oxide buffer layer thicknesses, the high Q modes (shorter wavelength modes shown in Fig. 22(a) shift towards shorter wavelengths, with the filter Q value maximizing around 10,000,000 for a buffer layer of $t_b = 60$ nm, as shown in Fig. 22(b). Shown in Fig. 22(c) is the magnified spectral plot for the transmission dip with a Q of 10,000,000. Simulated field distribution profiles for three cases close to the maximum Q are shown in Fig. 22(d), where strong field confinement is evident for the high Q transmission dips at the optimal buffer layer thickness.

Two types of structures were prepared for double-layer PhC Fano filters on silicon and on quartz substrates. For the double-layer PhC Fano filters on SOI, a low index oxide buffer layer was first formed using thermal oxidation of a single-crystalline Si layer on the SOI substrate, followed by a low pressure chemical vapor deposition (LPCVD) poly-Si deposition process, to form a poly-Si/thermal SiO₂/crystalline-Si double-Si-layer structure. The other double-layer PhC Fano filters on quartz substrates were formed by two rounds of the LPCVD poly-Si deposition process, with a plasma-enhanced chemical vapor deposited (PECVD) SiO₂ layer sandwiched in between the two LPCVD poly-Si layers. Shown in Figs. 23(a)–5(c) are cross-sectional SEM images for the double-layer poly-Si/SiO₂/c-Si filter structures, with different thermal oxide thicknesses. The same E-beam patterning and etching processes were utilized for the 2D-PhC patterning. An SEM image is shown in Fig. 23(d).

The double-layer Fano filters were characterized by measuring transmission or reflection spectra for the two different configurations. For the transmission measurement on the double-layer filter quartz substrate, a transmission dip at 1545.2 nm was obtained, with an estimated Q of 5000 and an extinction ratio of 2.7 dB (Figs. 24(a) and 6(b)). For the reflection measurement on the double-layer filter on SOI substrate, a reflection peak was obtained at 1567 nm with a Q factor of 9734 and an extinction ratio of 8 dB (Figs. 24(c) and 6(d)). All of these measured spectra match well with the simulated ones at these resonance locations (with spectral dips or peaks). The measured Q values are lower than the simulated ones, which may be due to the imperfect process of etching the air holes, such as the conical shape and different hole sizes in the trilayer structure. We expect the filter performance to be improved with much higher Q factors when we optimize the fabrication process.

4.3.3. Double layer Fano resonance filters with controlled lattice displacement

It was theoretically understood that allowing lateral displacement of the lattices in the two layers with respect to each other enables an additional degree of freedom in controlling the filter characteristics of the two-layer structure [120,126]. However, experimental demonstration of coupled double-layer PCS structures with controlled lattice displacement has never been

reported, due to the challenges associated with the fabrication. But, by employing the PDMS (polydimethylsiloxane) nanomembrane transfer printing technique, it is possible to stack multiple layers of semiconductor and other dielectric materials [47,57]. Recently Shuai et al. [127] reported experimental demonstration of coupled double-layer PCS with precisely controlled lattice displacement, based on transfer printing and multi-layer e-beam patterning alignment processes [47,55]. Both simulation and measurement suggest that optical filter Q factors are very sensitive to the lattice displacement. For one structure with relatively large lattice displacement, they demonstrated a Q factor of 80,000 experimentally. Further design and process optimization leads them to expect much higher Q -factors, particularly due to a simulation Q factor of 2.11×10^8 for coupled double-PCS structures with optimal lattice displacement [127].

Shown in Fig. 25 are simulated transmission and reflection spectra for double layer stacked Fano filters without (Fig. 25(a and c)) and with (Fig. 25(b and d)) lattice offset ($\Delta x = 0.2a$, $\Delta y = 0.5a$), with the insets showing the magnified plot for the dominant (highest Q) resonance in each case. Also shown in the insets are the schematics of the structures considered in the simulation. For the transmission spectra shown in (Fig. 25(a and b)), a glass substrate was used. For the reflection spectra shown in (Fig. 25(c and d)), an SOI substrate was employed. The design parameters are $a = 1000$ nm, $r/a = 0.08$, $t_1 = t_2 = 230$ nm, and $t_b = 20$ nm. Simulations

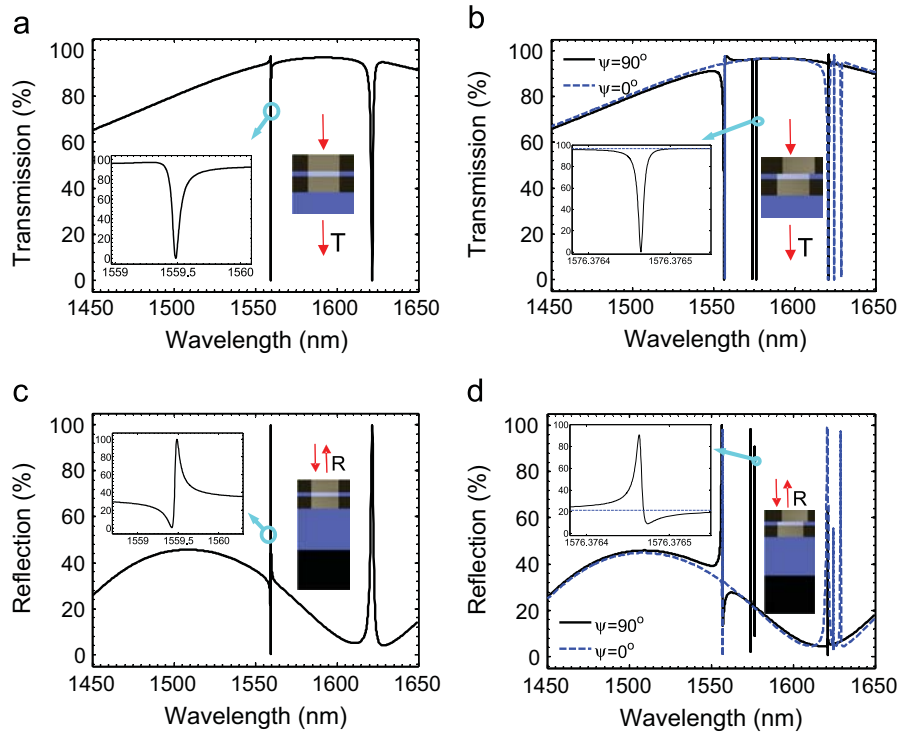


Fig. 25. Simulated transmission and reflection spectra for double layer stacked Fano filters with (b and d) and without (a and c) lattice offset ($\Delta x = 0.2a$, $\Delta y = 0.5a$), with the insets showing enlarged plots for the dominant (high Q s) resonance for each cases. Also shown in the insets are the schematics of the structures considered in the simulation. For the transmission spectra shown in (a and b), glass substrate was considered. For the reflection spectra shown in (c and d), SOI substrate was considered. Ψ represents the incident beam polarization (E -vector) defined as the angle from the positive x -axis to the polarization direction. Reproduced with permission from [127].

were carried out to find the Q factors for the different lattice displacements. The results shown in Fig. 25(b and d) correspond with the highest Q value obtained for this set of design parameters. Notice that the Fano filter Q increases from 26,000 and 28,000 for perfectly aligned lattice structures (Fig. 25(a and c)) to 2.11×10^8 and 1.76×10^8 for lattice misaligned structures (Fig. 25(b and d)) with optimal lattice displacement being $\Delta x = 0.2a$ and $\Delta y = 0.5a$. It is also worth mentioning that the low index buffer layer thickness (e.g. SiO₂ used here) can also be varied for Q -factors approaching infinity [38,120].

Following a short thermal oxidation process for the formation of a thin SiO₂ buffer layer ($t_b = 20$ nm) on top of the silicon-on-insulator (SOI) substrate, single layer Fano filters were fabricated with standard electron-beam lithography and dry etching processes. An un-patterned single crystalline Si nanomembrane was then stacked onto the patterned single layer Fano filter using the PDMS stamp assisted membrane transfer printing process. Filters with different displacements were fabricated. Shown in Fig. 26(a and b) are scanning electron microscope (SEM) images of fabricated double layer Si-NM Fano filters with displaced lattices between the coupled layers. Shown in Fig. 27 are the results obtained for the coupled double layer PCs, with large lattice displacement ($\Delta x = 0.495a$, $\Delta y = 0.45a$). A measured reflection spectrum is shown in Fig. 27(a), along with a top SEM image shown in the inset. We obtained two resonant locations, around 1548.6 nm and 1567 nm, with a magnified plot around 1548.6 nm resonant shown in Fig. 27(b). Again, simulation and Fano fit were carried out and the results match the experimental results well. In this case, we obtained a Q factor of 80,000. This value is the highest experimental Q factor reported so far, for all the different cases we fabricated. While the value is

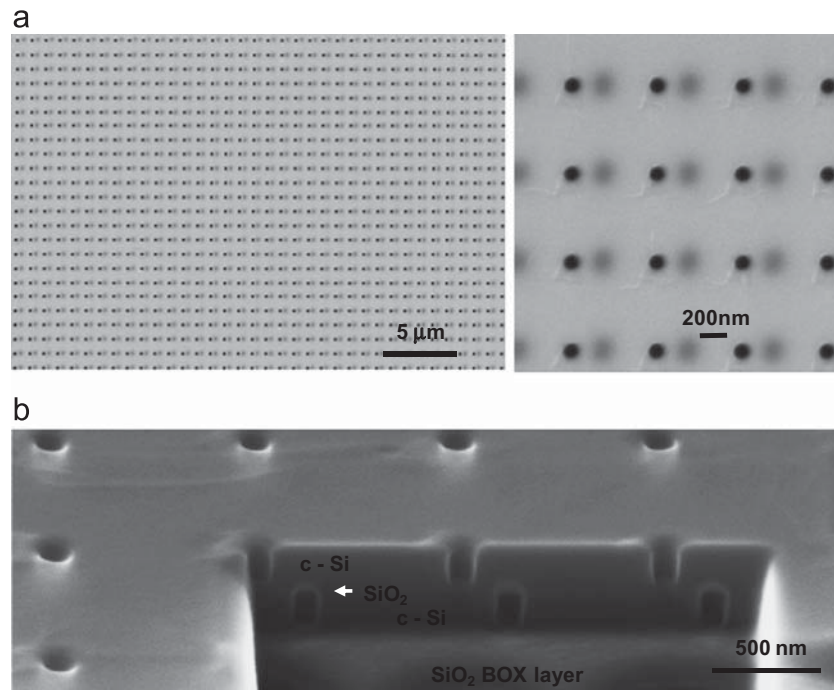


Fig. 26. Fabricated Fano filter scanning electron micrograph (SEM) images: (a) top view and (b) cross-sectional view of double layer Fano filter on SOI, with controlled lattice misalignment offset ($\Delta x = 0.2a$, $\Delta y = 0$). Reproduced with permission from [127].

still far from the optimal Q factor of 2.11×10^8 , the results demonstrate the great potential of coupled double-layer PCS structures with controlled lattice displacement. During testing, we also noticed that the performance of these filters is very sensitive to incident beam direction, collimation and polarization orientation. We anticipate much higher Q -factors can be obtained with precisely controlled displacement and an optimized fabrication process.

5. Fano resonance photonic crystal membrane reflectors

Surface-normal ultra-compact dielectric broadband reflectors are essential components for numerous optoelectronic devices, such as microcavities, lasers, photodetectors, filters, switches, solar cells, sensors, reconfigurable photonics, etc. [128] Typically high reflectivity dielectric mirrors are constructed using multi-layer films, such as distributed Bragg reflectors (DBRs) [129]. Strong reflection has also been observed with guided resonance in 1D or 2D grating structures [10,121]. As an alternative to the conventional multi-layer structure, single layer, high index-contrast sub-wavelength grating (HCG or SWG) structures that can be used as

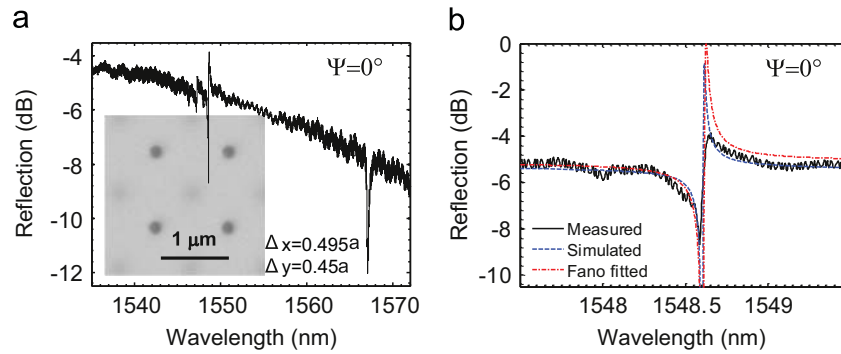


Fig. 27. Measured displaced Fano filter ($\Delta x=0.495a$, $\Delta y=0.45a$) reflection spectra for p-polarization state, with theoretical and experimental Q -factors of 115,000 and 72,000, respectively. Shown in the inset is the magnification of the measured reflection spectrum. Reproduced with permission from [127].

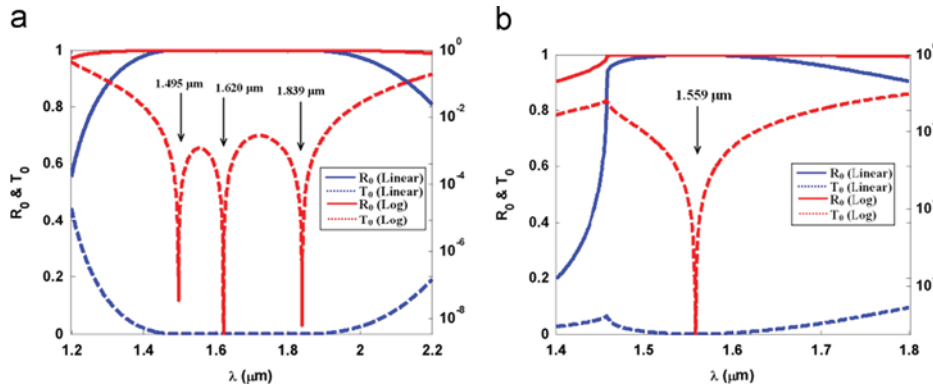


Fig. 28. The physical basis for broadband reflection in 1D gratings: zero-order reflectance and transmittance spectra of broadband reflectors operating in (a) TM and (b) TE polarizations. For clarity, the spectra are plotted on both linear and logarithmic scales. Reproduced with permission from [11].

ultra-compact broadband reflectors hold great promise for a wide range of devices [11,13,130]. However, basic one-dimensional SWG structures are intrinsically polarization-dependent [12,131]. Recently, more complicated grating structures have been proposed for polarization independent reflectors [132].

Two-dimensional photonic crystal slab (2D PCS) structures, on the other hand, can be used in both polarization dependent and independent operations, with proper dispersion engineering and structural optimizations [9,33,45,126]. Suh et al. [45] demonstrated that broadband near 100% reflection for normal incident light can be obtained using a single dielectric layer PCS with square lattice air holes in a high-dielectric index film. The first detailed analysis of the angular and polarization properties in 2D PCS based MR's was reported by Lousse et al. [123]. They found that 2D PCS MR's can be designed to have broadband reflection over a range of incident angles for both polarizations, or to reflect one polarization completely, while allowing 100% transmission for the other polarization, behaving as a polarization splitter with complete contrast. While the initial experimental demonstrations showed relatively narrow reflection bands [121,123], subsequent reports showed rapid progress and drastic improvements in performance [46,123]. In this section, we will review the progress made towards ultra-broad reflection band MR's based on 2D PCS, their phase properties, as well as the polarization and angle dependent properties.

5.1. Broadband reflector design

One of the key design targets for broadband reflectors is high reflectivity spectral bandwidth. The spectral bandwidth and reflection properties have been well investigated in multi-layer DBR based reflectors, where ultra-broadband reflectors can be achieved with the control of index contrast between pairs of dielectric layers. However, it remains a challenge to understand the correlations between spectral bandwidth and the design parameters in 2D PCS based MR structures. On the other hand, details of theoretical investigations have been reported indicating the physical basis for wideband resonators in 1D grating structures. Magnusson et al. attributed the broadband reflection in 1D gratings to the coupling of leaky modes and their excitation conditions [11]. In a design with a target reflection band over 1.45–2.0 μm for TM polarization in a high index contrast 1D Si grating on an oxide substrate, they reported a very broad reflection bandwidth of 520 nm, with 99% reflection for TM polarization, which was supported by a blend of three guided mode resonances (transmission dips) located inside the band (Fig. 28(a)). Similar

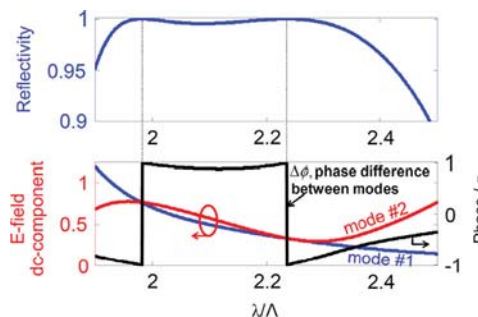


Fig. 29. The physical basis for broadband reflection in 1D HCG reflectors: Double-mode solution exhibiting perfect cancellation at the HCG output plane leading to 100% reflectivity. At the wavelengths of 100% reflectivity both modes have the same magnitude and opposite phases. Reproduced with permission from [133].

analysis was applied to a design for TE polarization, with a reflection band of 125 nm for 99% reflection (Fig. 28(b)).

On the other hand, Karagodsky et al. [133] presented an analytic analysis of the ultra-high reflectivity of sub-wavelength high contrast grating reflectors, and it was classified as a destructive interference effect between the two grating modes. The average lateral e-fields of the first two modes are plotted with their phase difference in Fig. 29. At 100% reflectivity, the modes are at anti-phase with equal intensities, which means that perfect cancellation occurs. If two such 100% reflectivity points are located within a small spectral vicinity, a broad-band of high reflectivity can be achieved. The authors also presented a quickly-converging matrix transmission line formulation for the HCG reflectivity and discussed a graphic design algorithm for broadband HCG mirrors.

For 2D PCS based MR's, the designs are largely based on the trial-and-error approaches based on complete 3D computational tools, such as RCWA and FDTD techniques. Based on the different designs for high Q filters and broadband MR's, researchers found that the Q factor (spectral linewidth) can be controlled by varying the radius, with very small r/a values (~ 0.1) favoring high Q filter designs and large r/a values (0.3–0.49) favoring broadband reflector designs. Additionally, the layer thickness is optimal at around 0.1λ , where λ is the wavelength in the structure. Other design parameters include the lattice structure and the air hole shape, the buffer layer selection below and above the functional layer, effective indices, and so on.

Boutami et al. [46] reported experimental demonstration of 2D PCS based MRs with controlled polarization dependence and a superior reflection band of 200 nm at a 1550 nm wavelength. Based on the elliptical air hole design in a square lattice photonic crystal InP membrane structure, polarization-dependent MR's were demonstrated. Later, designs of MR's on SOI were reported by Qiang et al. [134] who demonstrated control of reflection bands based on the control of vertical confinement with controlled refractive indexes for the buffer layers below and above the MR layer. Detailed experimental results were subsequently reported by Yang et al. [135] with a controlled index tuning range over 50 nm for both blue and red shifts, in which they controlled the buffer oxide index with controlled etching and the index above the slab with controlled oxide deposition.

Further design optimization leads to a much broader reflection band in Si-based 2D PCS MR's. In addition to the lattice parameters, buffer layer index control is also very important for achieving high performance MR's. Two optimized designs are shown in Fig. 30. In Fig. 30(a),

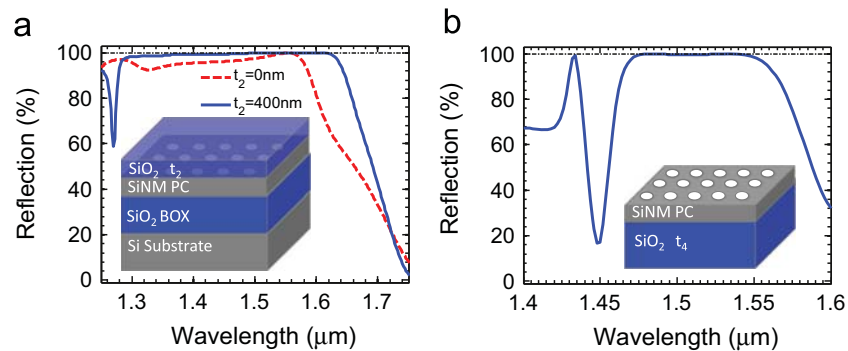


Fig. 30. Design of membrane reflectors (MR's) at 1550 nm: Simulated reflection spectra for (a) MR on SOI with top SiO₂ buffer layer (t₂); and (b) MR on glass substrate. Key lattice parameters are (a): $a=880$ nm, $r/a=0.45$; and (b) $a=1010$ nm, $r/a=0.3$.

the MR design was based on an SOI substrate, with an optional top SiO_2 buffer layer of t_2 . Notice that with the optimal thickness of t_2 , there is a significant improvement in reflection spectrum performance, with a reflection band of over 300 nm. On the other hand, in another design with an SiNM PC MR on a glass substrate, we can achieve reflection band of 100 nm, as shown in Fig. 30(b).

5.2. Different configurations and buffer layer design

Taking advantage of the design freedoms associated with the MR structures, various configurations of MR's have been investigated, mostly on SOI substrates. One of the unique features is the potential for post-process spectral trimming capabilities in MR structures, achieved by altering the effective index of the surrounding medium. Resonance control of the reflectors is accomplished either by partially removing the buried oxide layer underneath the device layer, or by controlled SiO_2 film deposition on top of the device. Both blue- and red-shifts were demonstrated with a turning range of 50 nm and a central wavelength of 1550 nm [135].

In addition to the spectral trimming, the addition of a SiO_2 layer on top of the Si MR structure on the SOI substrate improves MR performance. As shown in Fig. 31, by depositing a ~ 400 nm SiO_2 on top of the Si MR, one can slightly improve the spectral red-shift performance compared to that of the simulated one. Note also that, with the control of SiO_2 deposition process, it is possible to control the effective index in the air hole region with selectively filling the air holes with SiO_2 .

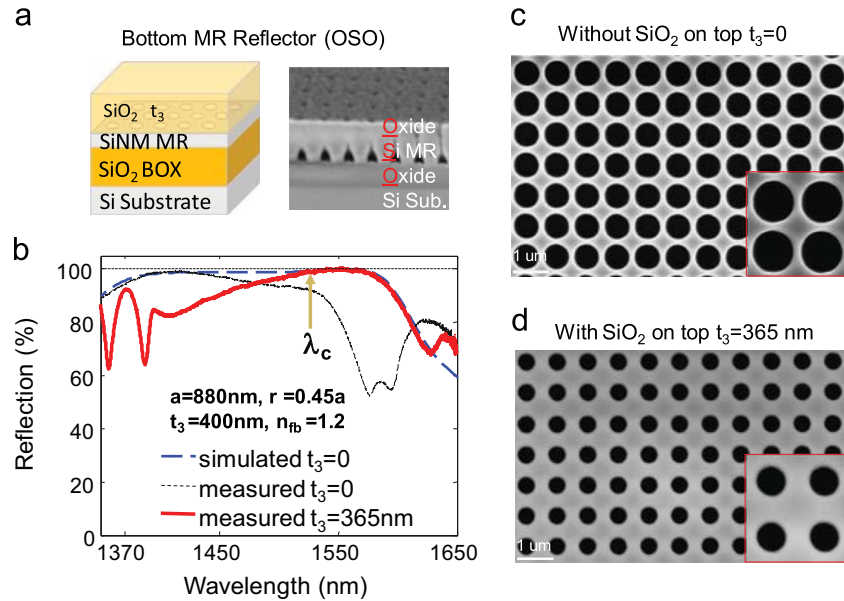


Fig. 31. Experimental demonstration of Si MR with a top SiO_2 layer: (a) a schematic and a SEM image of an OSO Si MR with an oxide buffer; (b) measured and simulated reflection spectra for the bottom OSO MR reflector; (c and d) SEM images of the fabricated bottom MR reflector with and without an oxide buffer layer on top. Notice reduced air hole size on top (compare (d) to (c)) due to partial enclosure of air hole region associated with the oxide PECVD deposition, as shown in the cross-section view in (a).

Another structure demonstrated is the Si-MR on a glass substrate, employing a modified PDMS stamp transfer printing technique [114]. Polarization independent reflection properties were also obtained, both theoretically and experimentally. Based on spectral scaling properties, the design of MR's at near infrared can be extended further to visible and longer wavelengths, as shown in Fig. 32 [136]. An MR operating at $\sim 76 \mu\text{m}$ was also demonstrated experimentally, with close to 100% reflection. [136]

For practical applications, large area MR's, which require more scalable manufacturing processes, are needed. Seo et al. [74] reported a $2 \text{ cm} \times 2 \text{ cm}$ large MR on a glass substrate, patterned with laser interference lithography (LIL) and printed with elastic stamp membrane transfer printing techniques. High reflectivity broadband membrane reflectors on glass were realized with reflectivity of 95% around 1300 nm and a bandwidth of about 100 nm. Very recently, a magnetic-field guided metal-assisted chemical etching process (*h*-MacEtch) was developed to replace dry etching process for the fabrication of high performance Si MRs [137].

5.3. Energy and phase penetration properties in membrane reflectors

Under surface-normal incidence, DBR, 1D SWG, and 2D PCS reflectors can all exhibit similar reflection properties with extremely high reflection and broad reflection spectral bands. However, their reflection mechanisms are different. For 1D SWG and 2D PCS mirrors, the incident wave couples with the in-plane guided-mode based on phase matching conditions. The wave then reradiates at one edge with a zero phase difference and at another edge with a π phase difference.

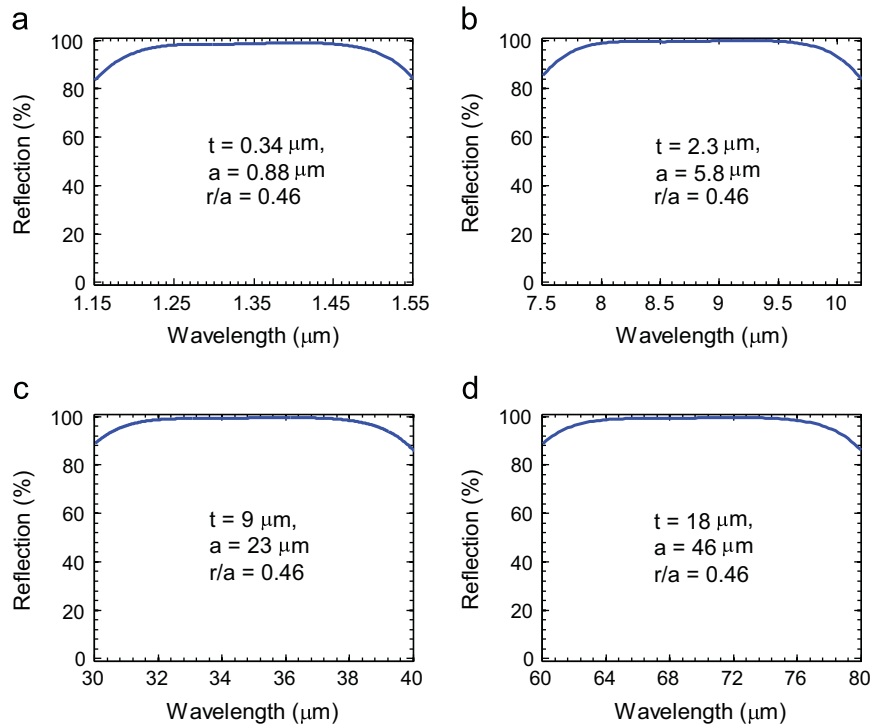


Fig. 32. Scaling of MR from near infrared to far-infrared: designs of Si-MR on SOI operate at different spectral bands. Reproduced with permission from [136].

Consequently, these constructive and destructive interferences result in high reflection and low transmission [74]. While for DBR, the high reflectivity arises from the multiple reflections with constructive interference among these reflected waves. Due to the large index difference, Bragg mirrors possess a broad reflection spectral band [137]. For 1D SWG and 2D PCS mirrors, the broad reflection spectral band most likely originates in the cooperation of the several adjacent guided mode resonances [11]. In Ref. [138], the authors reported excellent work on the phase discontinuity Φ_r and the energy penetration depth L_e , which were estimated from the mode spacing in the Fabry-Perot (FP) cavity. In 2009, the in-plane optical property of 2D PCS was reported by Sauvan [139]. With fully vectorial calculations, in heterostructure mirrors, the penetration length associated with the delay was much larger than the characteristic damping length of the energy distribution inside the mirror. This amazing property is evidence that these two characteristic lengths are not necessarily correlated. Consequently, the usual trade-off between short damping lengths and large penetration lengths that is encountered in classical DBRs can be overcome with carefully designed PhC structures. Later Zhao et al. [140] investigated in more detail the phase and energy penetration depths, and field distributions of 1D SWG and 2D PCS reflectors.

In dielectric mirrors, the reflection is not an instantaneous process. It includes a reflection time delay (τ) and energy storage in the mirrors. The reflection delay increases the laser cavity round-trip time or the photon lifetime. The energy storage in mirrors decreases the modal volume and

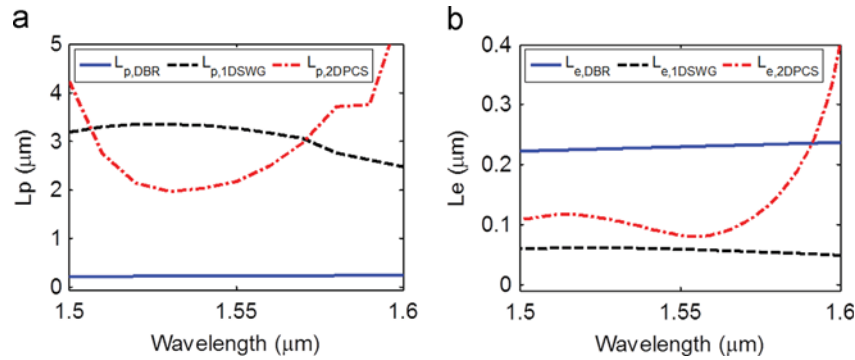


Fig. 33. (a) Calculated phase penetration depths for three types of reflectors; and (b) The energy penetration depths for three types of reflectors. Reproduced with permission from [140].

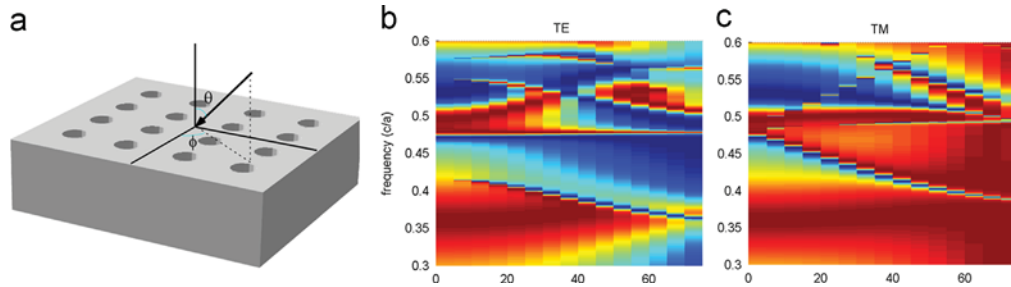


Fig. 34. (a) Photonic crystal structure consisting of a square lattice of circular air holes in a dielectric slab and angular study for TE-polarization. (b) TM-polarization of the filter responses for the photonic crystal structure with the angle φ (given in degrees)=0. Reproduced with permission from [123].

the confinement factor in the small cavity, such that the cavity round-trip time and the cavity volume have a comparable magnitude as the reflection delay and the mirror storage [20,21]. The reflection delay is directly related to the slope of the reflection phase shift Φ_r . The relation can be expressed as $\tau = \partial\Phi_r / \partial\omega$. The phase penetration depth, L_p , is defined as the half-distance that light propagates in the incident medium during this delay time,

$$L_p = \frac{1}{2} v_g \tau = \frac{v_g}{2} \frac{\partial\Phi_r}{\partial\omega} \quad (17)$$

where v_g is the group velocity of the incident wave.

The energy storage is always associated with the parameter of energy penetration depth, L_e . It is the length that the field intensity decays to $1/e$ of its maximum from the edge of the cavity into the mirrors. However, this method is not suitable for calculating the L_e of the PC mirrors we discussed here, because the guided modes are excited inside the mirrors. But L_e can be estimated from the mirror transmission or reflection based on the following equation:

$$T = 1 - R = \exp\left(-\frac{h}{L_e}\right) \quad (18)$$

where T is the transmission and h is the mirror thickness [139,140]. While, for DBRs, L_e can be obtained with [141]:

$$L_e = \frac{m_{eff}}{2} \left(\frac{\lambda}{4n_1} + \frac{\lambda}{4n_2} \right) \quad (19)$$

where $m_{eff} = \tanh(2mr)/(2r)$ is the effective period number seen by the incident light. $r = (n_1 - n_2)/(n_1 + n_2)$ and m are the actual period number in DBRs. n_1 and n_2 are the refractive index of the two materials in DBR. In the following we will numerically investigate the phase and energy penetration depth according to the above definitions.

Based on the simulation results shown in Fig. 33, compared to the DBR reflectors, these new types of single layer ultra-compact broadband reflectors can have more complicated larger phase delays and smaller energy penetration properties, which can be engineered via dispersion engineering for large spectral dependent phase delays, and ultra-small energy penetration depths. The work reported was mostly based on one set of optimized design parameters for 1550 nm band reflectors. Following similar procedures, other design parameters can be used for reflectors with different reflection requirements, as well as different phase delays, energy penetrations, and field distributions. All the results and conclusions can be very helpful for the design of resonant cavities for a wide range of photonic devices.

5.4. Angle and polarization properties

For the practical application of a highly reflective two-dimensional photonic crystal slab MR's, analyzing the angular dependency is important since the lateral dimensions of an incident beam are always finite and thus such beams consist of multiple angular components. Lousse's work [123] showed that a nearly-complete reflection could be obtained for wide frequency and incident angle ranges with the proper design of the crystal. One example of the angular polarization plots in Fig. 34 showed that the broad strong-reflectivity remains for a wide range of incidence angles θ . For both TE/TM polarizations, the reflectivity in this frequency range stays higher than 95% when the angle θ is increased from 0° to 15° . For higher incidence angles, transmission peaks due to additional resonances progressively appear in the high-reflectivity

window, first for TE polarization and then for both polarizations. The high-reflectance zones therefore close at high angles partly due the presence of lower-order resonances.

In the case of square lattice, air-hole photonic crystal structure based MR's at the normal incidence direction, as we discussed here, there is a 90-degree rotational symmetry, and therefore the reflectivity is independent of the polarization [114]. On the other hand, when the rotational symmetry of the structure is reduced, one could create mirrors that are polarization dependent. [46]

The reflection properties at oblique incidence were investigated experimentally by Chadha et al. [142] based on a 2D PCS MR structure. As expected, polarization independent reflection was obtained at surface normal direction. Additionally, high reflection can also be obtained for one polarization state over a wide range of incident angles. The experimental results were also correlated with the angle dependent Fano resonant mode dispersion properties.

Photonic crystal (PhC) Fano broadband reflectors have the potential to remove all the limitations associated with the conventional DBR reflectors [142]. A multi-wavelength laser array is thus feasible with the control of in-plane lattice parameters (i.e., lithography). Most importantly, MR reflectors can be made very compact, with sub-wavelength-scale thicknesses over a wide spectral range. This attractive feature has significant advantages over conventional DBR based reflectors. Since the DBR reflector thickness scales with wavelength, it becomes impractical for longer wavelength devices, where the thickness of DBR could approach 10–50 μm , assuming 20 pairs of DBRs with indices of 3.5 and 3.0 for high and low quarter-wavelength thick materials, respectively.

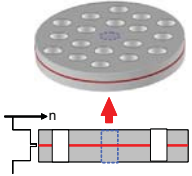
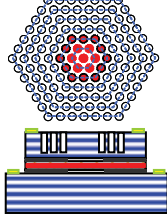
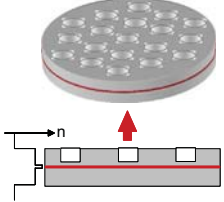
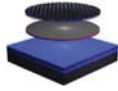
6. Fano resonance photonic crystal membrane lasers

6.1. Photonic crystal functions in light sources

Since the first proposal of spontaneous emission control with photonic crystals [130], a large variety of light emitting devices have been demonstrated, mostly with planar 2D PCS air hole lattice structures. A summary of different surface emitting lasers is given in Table 3. Broadly speaking, there are four types of PCS based light sources:

- a. Photonic bandgap defect mode lasers (PBDL): By etching through the active region of the light emitting structure, the spontaneous emission process can be altered in the defect (point and line defect, surface wave modes) cavity region, where enhanced/suppressed spontaneous emission is feasible when the active light emission region is placed inside the PBG defect cavity [143,144]. With extremely high Q/V_{mode} (Q and V_{mode} being the corresponding quality factor and modal volume, respectively), strong spontaneous emission control is feasible for ultra-low threshold single mode lasers. This configuration can lead to potentially thresholdless lasers (or single-mode LEDs) and single photon sources [145–151].
- b. Photonic crystal confined VCSELs (PC-VCSELs): In this case, the photonic crystal defect cavity is incorporated near the active region (no etching through), into the cladding layers or top DBR layers. The output modal control of the light emitters (LEDs or VCSELs) is feasible due to the feedback mechanics associated with the PhC cavities [150–153]. There is no or very little impact on the spontaneous emission process inside the active region.
- c. Photonic bandedge lasers (PBEL): Surface emitters based on the multi-directional distributed feedback effect occurring at frequencies close to band-edges in a defect-free PCS. In this case, the PCS serves as a 2D distributed feedback structure, with similar functions to those of 1D grating in conventional DFB lasers. This enables coherent lasing emission and polarization

Table 3
Photonic Crystal Surface Emitting Lasers (PCSELs).

Configurations	PhC functions	Characteristics	Ref.
<i>Defect-mode PhC lasers</i>			
PBDLs	<i>Photonic bandgap defect mode lasers:</i>		[145–149,163]
	<ul style="list-style-type: none"> ● 2D PhC air hole: Defect mode at the center of the PBG for enhanced spontaneous emission 	<ul style="list-style-type: none"> ● Spontaneous emission control with high spontaneous emission factor ● Potentially zero threshold ● Wavelength agile fabrication ● Potentially single photon sources 	
PC_VCSEL	<i>Photonic crystal confined VCSELs:</i>		[152,153]
	<ul style="list-style-type: none"> ● DBR (1D PhC): HR mirror for high Q cavity formation ● 2D PhC air hole: lateral mode confinement 	<ul style="list-style-type: none"> ● Mature DBR VCSEL technology; ● Relatively low threshold ● High output power ● Proven reliability ● Possibly high power single mode in PC-VCSELs 	
<i>Defect-free Phc lasers</i>			
PBEL	<i>Photonic Crystal DFBs or Photonic Bandedge Lasers:</i>		[154–159]
	<ul style="list-style-type: none"> ● Distributed feedback ● Enhanced gain at bandedge due to flat dispersion (zero group velocity) 	<ul style="list-style-type: none"> ● DBR free with simple wafer growth (LED like structure) ● Spontaneous emission control with high spontaneous emission factor ● Potentially zero threshold ● Wavelength agile fabrication ● Energy efficient ● Scalable power output ● Precise cavity control enable high uniformity 	
MR-VCSEL	<i>Membrane-reflector VCSELs:</i>		[57,161,164]
	<ul style="list-style-type: none"> ● Fano resonance broadband membrane reflectors 	<ul style="list-style-type: none"> ● DBR free with simple wafer growth (LED like structure) ● Wavelength agile fabrication ● Energy efficient ● Scalable power output ● Precise cavity control enable high uniformity 	

control over large areas, for potentially high power single mode lasers [154–159]. Noda [160] presented an excellent review on PBDL and PBEL.

d. Membrane reflector VCSEL (MR-VCSEL's): based on the Fano resonance principles, broadband reflection can be achieved in single layer membrane reflectors (MR's) based on 1D

or 2D PCS. These ultra-compact high performance MR structures have been proposed to replace the bulky DBR structures, to create ultra-compact MR-VCSELs [57,161]. Taking advantage of Fano resonance principles, ultra-compact high performance VCSEL cavities can be formed on any substrate, such as III–V and Si, because the mirror cavity and the gain medium can be heterogeneously integrated with different material systems. This is one of the most promising ways to form lasers on Si, and to form high performance long wavelength VCSELs, in which DBR remains a great challenge.

Among four configurations discussed above, both PBDL and PC-VCSEL utilize the localized or defect mode in the photonic bandgap (PBG). On the other hand, for the latter two configurations (PBEL and MR-VCSEL), it is not essential to design PCS's with PBG's, as both utilize distributed feedback and dispersion properties in defect-free PCS structures. While PBEL can utilize the mode both below and above the light lines, MR-VCSEL's only use the modes above the light lines. Since the Fano resonances are always related to the radiation modes above the light line, our discussion of Fano resonance photonic crystal membrane lasers will mainly focus on the lasers based on those modes. Fano resonance modes can be designed in PBEL, where lasing is feasible due to distributed feedback and the slowlight effect [162]. Most notably, the other type of Fano resonance based laser is the recently demonstrated MR-VCSEL, where Fano resonance membrane reflectors are incorporated in the VCSEL cavity design to form ultra-compact VCSEL's and lasers on any substrates, including both III–V and Si, for potential Si photonics integration.

Since the thin film Si membrane with the PC pattern can work as a broadband reflector with very high reflection, the conventional DBR-based VCSEL can be made more compact by replacing the thick DBRs with thin membranes just a few hundred nanometers thick. This concept was proposed and theoretically investigated by Magnusson et al. [165], Hattori et al. [166], Boutami et al. [167,168] and others [169,170]. In their investigations, either the top mirror or both the top and bottom DBRs were replaced with 1D grating mirrors. Huang et al. [130] and Boutami et al. [15] both experimentally demonstrated this in both InP-based and GaAs-based VCSEL's, where the top DBR was replaced with monolithically grown InP or GaAs single layer 1D grating mirrors. In the following years, many different configurations have been reported, with very promising results [13,171].

Based on the transfer printing nanomembrane process, we proposed and later experimentally demonstrated 2D PCS based membrane reflectors (MRs) and MR-VCSELs on silicon [57,164,172]. In this section, we will review the design, fabrication, and characterization of MR-VCSEL structures, followed by a brief discussion of other types of PhC based light sources.

6.2. Design of MR-VCSELs

As shown schematically in Fig. 35, the MR-VCSEL cavity consists of a III-V InGaAsP quantum well (QW) cavity (layer t_3), sandwiched between two single-layer Si PC Fano resonance membrane reflectors (Si-MRs, layers t_1 and t_5). Two low index buffer layers (SiO_2 , layers t_2 and t_4) are inserted to ensure proper index contrast to the top and bottom Si-MR's. The complete MR-VCSEL cavity (from t_1 to t_5) is built on the top of a silicon-on-insulator (SOI) substrate with a SiO_2 box layer thickness of t_0 . In order to achieve low threshold lasing in such a cavity, it is highly desirable to design an MR-VCSEL cavity with the following characteristics: (a) both top and bottom MR's should have broadband reflection bands, with reflections greater than 99%; (b) the cavity should be designed so that the cavity mode is spectrally separated from

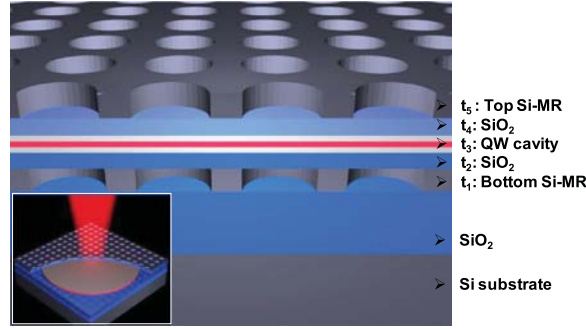


Fig. 35. Schematic of MR-VCSEL laser cavity structure, which consists of five layers (t_1 – t_5): an InGaAsP QW cavity sandwiched in between two single layer Si Fano resonance PC membrane reflectors (Si-MR's), stacked on a Si substrate. Low index SiO₂ buffer layers are inserted to ensure high reflection of MR's. The inset is a complete MR-VCSEL cut-out view. Reproduced with permission from [164].

the waveguide modes; (c) the cavity mode should match the QW emission peak spectrally with or without spectral detuning; and (d) the cavity mode should have an optimal field distribution spatially matched with the QW active region for high confinement factors and low lasing thresholds.

An example of a complete MR-VCSEL cavity design is shown in Fig. 36. As shown schematically in the inset of this complete MR-VCSEL, a relatively large air hole radius is used for the Si-MR's, with $r/a=0.46$ and 0.45 for the top and the bottom Si-MR respectively. Other parameters are optimized at $t_0=2\text{ }\mu\text{m}$, $t_1=t_5=340\text{ nm}$, $t_3=465\text{ nm}$, respectively. The thicknesses of the low index buffer layers (t_2 and t_4) can be tuned to adjust the cavity mode location. To make the field distribution more symmetric inside cavity, another SiO₂ layer with $t_6=400\text{ nm}$ or thicker is deposited on the top of the MR-VCSEL and $n_f=1.2$ is also considered for the top Si-MR, because it has similar surrounding low index material to the bottom Si-MR. In simulation, a periodic boundary condition is used, i.e., the lateral dimension is infinite. Fig. 36(a) demonstrates the simulated reflections for the top and bottom Si-MR's based on 3D FDTD, with a peak reflection of 100% and high reflection band ($>98\%$) covering the wavelength range from 1420 to 1530 nm.

We use two different techniques to determine the cavity mode. The first one is to calculate the reflection of the whole cavity structure. From the dips located in the high reflection band range, we can easily find the cavity mode according to its resonant transmission property. The reflection of MR-VCSEL with $t_2=t_4=400\text{ nm}$ is plotted in Fig. 36(b) as the blue line, which is calculated with the RCWA technique. The dip is located at 1478 nm. To confirm this cavity mode, a method based on the phase resonant condition (total phase change of one round-trip in the cavity is equal to the integer multiplied by 2π) is used to decide the cavity mode. The phase calculation details can be found in [134]. After obtaining the reflection phase change (ϕ) of the top and bottom Si-MR's, the resonant cavity mode can be easily determined. The phase of the mode in cavity is shown in Fig. 36(b) as the red dotted line, which is plotted in the range $[0, 2\pi]$. One can find the mode located at 1478 nm with a 2π phase shift, which confirms that the mode at 1478 nm is a real cavity mode.

The quality factor and the field distribution of this cavity mode at 1478 nm are investigated by employing the FDTD technique. The quality factor of the cavity mode at 1478 nm is 4300 according to the equation $Q=\text{Re}(\omega)/-2\text{Im}(\omega)$. This cavity mode is excited and its stable field is recorded. The E-field of the standing wave distribution is demonstrated in Fig. 36(c) with the red

line, where the cavity index profile is also plotted with the blue line. One of E-field peaks is located at QW well region and the calculated confinement factor is about $\Gamma = 5.6\%$ according to $\int_{QW} E^2 dv / \int_{cav} E^2 dv$. Note that the field intensity inside the top and the bottom Si-MR is also

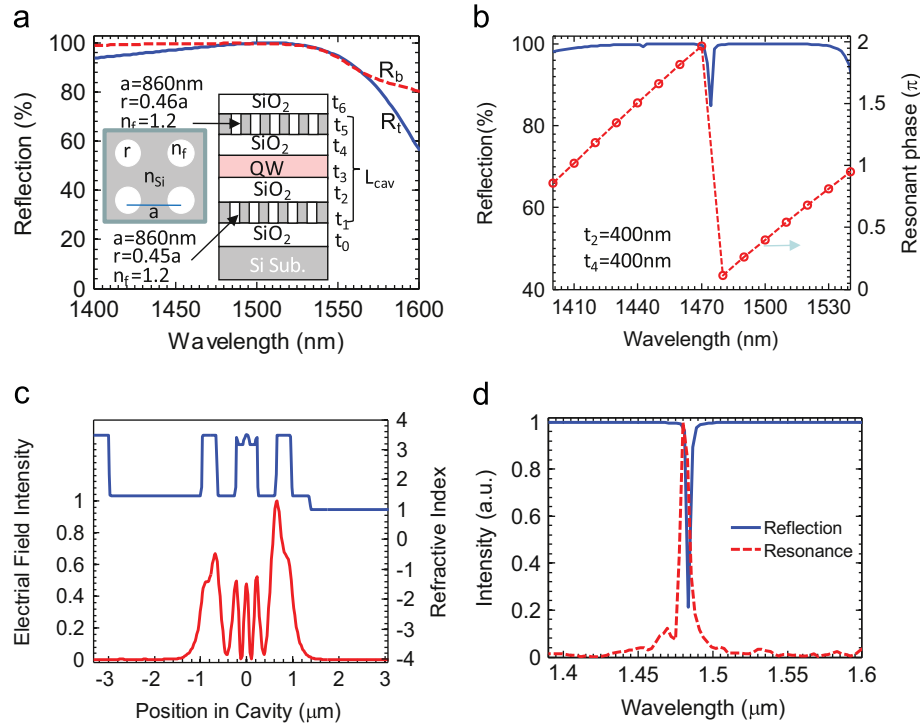


Fig. 36. Design of an MR-VCSEL cavity: (a) reflections of top and bottom MR's, inset is the MR-VCSEL cavity structure configuration, where $t_0 = 2 \mu\text{m}$, $t_1 = t_5 = 340 \text{ nm}$, $t_2 = t_4 = 400 \text{ nm}$, $t_6 = 400 \text{ nm}$. (b) Calculated cavity resonance mode based on cavity reflection and phase resonant condition. (c) Field distribution of cavity mode. (d) Cavity mode of MR-VCSEL cavity with finite size. Reflections (blue lines) and resonant (red dash lines) spectra of MR-VCSEL for Low T at $\lambda = 1478 \text{ nm}$. Reproduced with permission from [164].

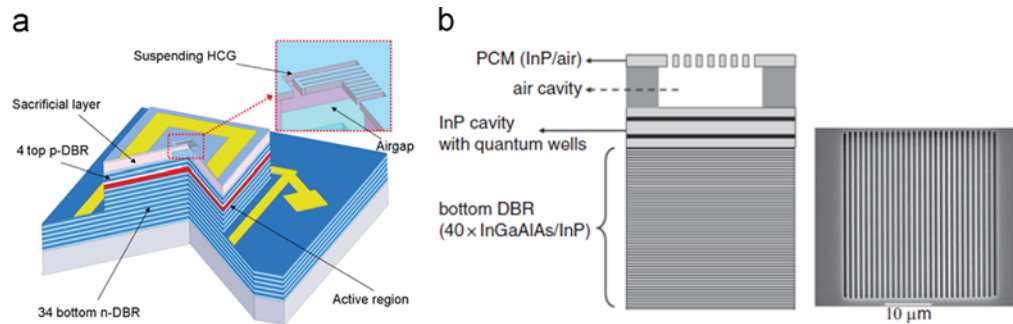


Fig. 37. Hybrid top MR/bottom DBR VCSEL configurations: (a) suspended GaAs high contrast grating (HCG) reflector monolithically grown on GaAs substrate; and (b) suspended InP 1D photonic crystal grating mirror (PCM) monolithically grown on InP substrate. Reproduced with permissions from [130,15].

relatively large. Although the field intensity inside Si-MR is large, it does not give rise to much cavity loss and the absorption loss since Si itself is transparent around 1550 nm. Most importantly, owing to the strong confinement in the reduced cavity lengths, the calculated confinement factor for Si-MR is similar to the typical confinement factors obtained in conventional DBR-based VCSEL's. This critical feature enables low threshold lasing in the MR-VCSEL cavities.

Considering the practical MR-VCSEL design, the top and the bottom Si-MR's may have different PC lattice parameters and the cavity has a finite size. In this case, instead of the simple periodical boundary condition, the perfect match layer (PML) boundary condition is used in FDTD simulations. Here we studied the cavity configurations with a square size $\sim 22 \times 22 \mu\text{m}^2$, $a_t = 860 \text{ nm}$, $r_t = 0.46a_t$, $a_b = 880 \text{ nm}$, $r_b = 0.45a_b$, $t_2 = 380 \text{ nm}$, $t_4 = 420 \text{ nm}$. The reflection of the cavity is obtained by calculating the reflected flux outside the cavity and the resonant mode is found through the Fourier transfer of the $E(t)$ of one monitor inside the cavity. The reflection and resonant spectra are plotted together with blue solid and red dashed lines in Fig. 36(d). The cavity mode match is well between the dip in the reflection spectrum and the peak in the resonant spectrum. In addition, the estimated Q of this cavity mode is ~ 1100 , which is largely limited by the relatively short amount of time in FDTD simulation. The simulation time and structure size are limited by the memory and the CPU number. A much higher cavity Q is expected in real structures due to their large size and better simulation resolution.

During the design, one interesting feature associated with top and bottom MR's is the excitation of the waveguide mode inside the QW layer since MR's can also work as couplers. The waveguide modes can be easily distinguished from the cavity mode by varying the thicknesses of oxide buffer layers ($t_2 = t_4$). The cavity mode shifts as the cavity length changes, while the waveguide mode does not. When designing the laser cavity, it is best to design it with the waveguide mode decoupled from the cavity mode to avoid any loss associated with this waveguide. The waveguide mode can be analyzed based on traditional waveguide theory [164].

6.3. MR-VCSEL Fabrication and configurations

6.3.1. Epitaxial growth approach

The most straight forward way of incorporating MR's is to grow the top MR layer monolithically on the laser heterostructure, to form hybrid VCSEL cavities with top MR and bottom DBR configurations. Huang et al. [130] reported an electrically pumped 850 nm VCSEL

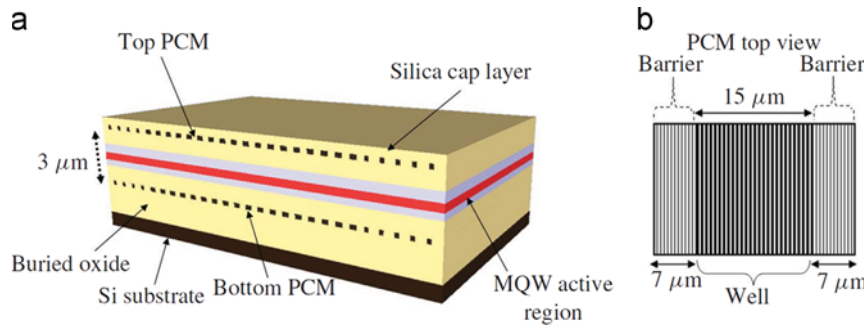


Fig. 38. (a) Schematic view of double PCM-VCSEL's for photonics-on-CMOS integration along with (b) a top view of a heterostructure-confined PCM. Reproduced with permission from [161].

on a GaAs substrate (Fig. 37(a)). Excellent performance was reported with single mode emission and a side-mode suppression ratio of 45 dB. Boutami et al. [15] reported an optical 1550 nm VCSEL on an InP substrate (Fig. 37(b)), with pulsed operation at room temperature and a threshold power around 15 mW.

6.3.2. Wafer bonding and CMP techniques

The ultimate goal for this configuration is to replace both top and bottom MR's with single layer MR's. However, in this case, monolithic growth is not possible. One straight forward technique is to use the wafer bonding technique for the integration of a gain medium on top of the bottom MR's. Sciancalepore et al. [161] reported an optically pumped 1550 nm VCSELs on Si. They used a double one-dimensional (1-D) PCM employing III–V/SiO₂ molecular bonding and amorphous-Si deposition processes. A 2-inch III–V wafer was bonded to a SiO₂ coated 200 mm silicon-on-insulator (SOI) wafer, followed by an InP substrate removal process. The polarization dependent top 1-D PCM was formed on a deposited amorphous-Si film using deep-UV lithography and reactive-ion etching (Fig. 38).

6.3.3. Transfer printing techniques

The fabrication process of MR-VCSEL is illustrated in Fig. 39 schematically. High quality patterned photonic crystal Si reflectors were fabricated via e-beam lithography and a reactive ion etching (RIE) process on SOI substrates with a 340 nm Si template layer and a 2 μ m buried oxide (BOX) SiO₂ layer. A low-index PECVD SiO₂ layer was then deposited on the top of the patterned Si to form the bottom MR.

Employing the PDMS stamp based transfer printing process, we transferred an InGaAsP QW active layer and disks to the SiO₂ layer on top of the bottom Si MR. Later, the top MR was patterned and released from the SOI substrates, and then transfer printed to a transparent glass substrate and it was then transferred to the top of the InGaAsP QW disks to complete the MR-VCSEL fabrication. Both the top MR and the bottom MR make up a single piece, while the InGaAsP disks are separated from each other, forming an array of disks.

One fabricated MR-VCSEL cavity, operating at a low temperature (LT Design), is shown in Fig. 40. Also shown in Fig. 40(a) is the scanning electron micrograph (SEM) image of the

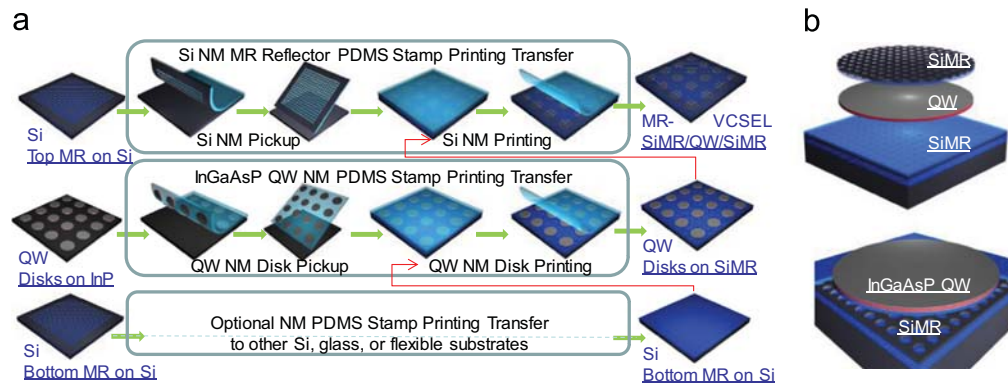


Fig. 39. MR-VCSEL fabrication based on the nanomembrane (NM) PDMS stamp printing process. (a) Schematic illustration of multi-layer PDMS transfer printing process for the formation of a MR-VCSEL array. (b) Schematic of a complete, individual MR-VCSEL device. Reproduced with permission from [57].

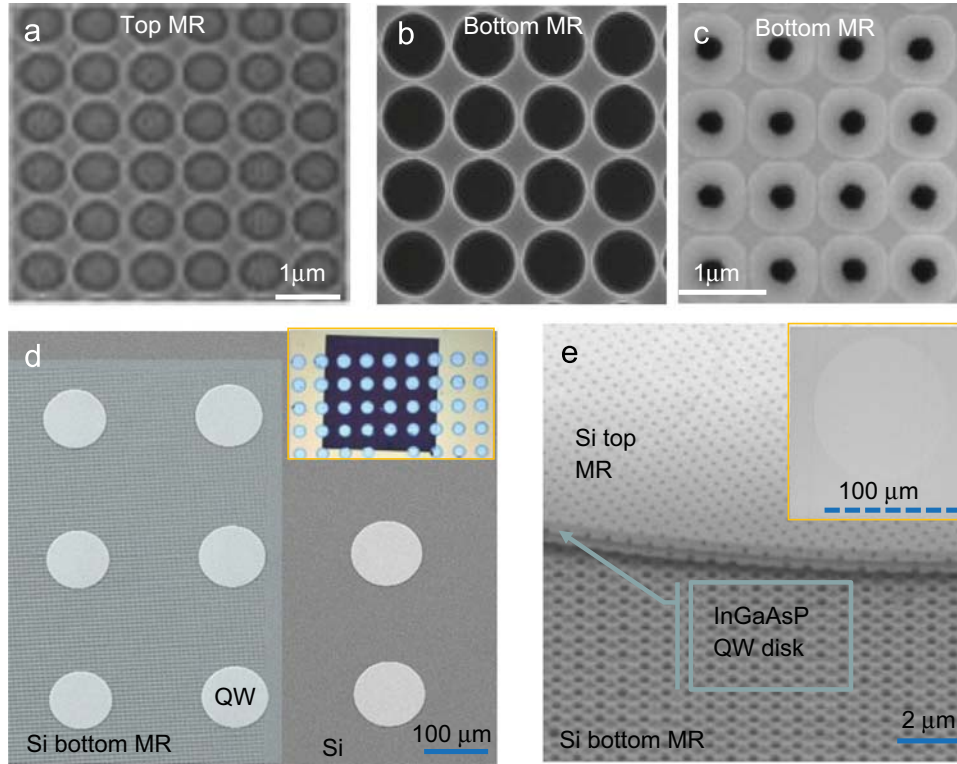


Fig. 40. SEM images and micrographs of a membrane reflector (MR) and an MR-VCSEL. Reproduced with permission from [57].

transferred top MR on a glass substrate with $a=860$ nm and $r/a=0.46$. The bottom SiMR with $a=860$ nm and $r/a=0.45$ was directly fabricated on an SOI substrate and followed by the deposition of a thin SiO_2 film on top, with a SiO_2 layer thickness of $t_2 \sim 383$ nm. SEM images before and after the top SiO_2 deposition are also shown in Fig. 40(b) and (c), respectively.

Fig. 40(d) shows a SEM image of the InGaAsP QW disks transferred onto the bottom SiMR. Shown here are six QW disks already transferred onto a patterned bottom SiMR region (another two QW disks were laid on the unpatterned Si region). The diameter D of these QW disks (i.e., the active area of the MR-VCSEL's) is $100 \mu\text{m}$. Shown in the inset of Fig. 40(d) is a micrograph of the top view of the fabricated device, with the QW disks transferred onto a bottom SiMR (the darkened square region). A complete MR-VCSEL structure is shown in Fig. 40(e), where both the top and bottom SiMR's are visible, with an inset showing a single QW disk underneath the top SiMR layer. Notice that the total vertical cavity thickness is only $2.4 \mu\text{m}$.

The reflections of these MR's are measured under normal incidence using a slightly focused white light beam and normalized with a gold mirror. The design and measurement results of the top and the bottom MR's are summarized in Fig. 41(a) and (b). All the reflectors designed and demonstrated here have peak reflection values of $>99\%$, with high reflection bands. It is clear that the measured and simulated reflections are matched well, indicating that our fabrication techniques work well. One thing we want to mention here is that the small dip at the edge of the

high reflection band comes from the non-ideal normal incidence, i.e., the slightly focused beam includes a small partial of oblique incident light around the beam edge.

The MR-VCSEL device is tested under the PL setup using a quasi-continuous wave (c.w.) 532 nm laser pump (with 50% duty cycle). Shown in Fig. 41(c) is the L - L plot (light output for different pump powers) and the corresponding spectral linewidths measured at $T=50$ K. The threshold pump power is ~ 8 mW, or 0.32 kW/cm². The measured spectral linewidths reduce from 30 nm below threshold to 0.6–0.8 nm above threshold. The measured spectral outputs are shown in Fig. 41(d), for pump powers below, at, and above threshold (points i, ii, iii, and iv at the L - L curve). The lasing spectral linewidth is ~ 8 Å, which is limited by the measurable resolution of the monochrometer. The relative peak location shift shown in Fig. 41(d) from bias levels (ii) and (iii, iv) is mostly related to mode hopping and the temperature rise inside the active region at higher pump power levels.

This MR-VCSEL LT device was also characterized at temperatures up to 120 K. Fig. 42(a) shows the normalized lasing spectra (arbitrary units, a.u.) above the threshold at $T=15$ K, 50 K, 70 K, 90 K, 120 K. We can find the lasing peak red shift as T increases and multimode lasing for most T cases at a rate $(d\lambda_c/dT)$ close to the simulated 0.088 nm/K. Mode hopping occurred below and above the operation temperature of 80 K. As T rose higher than 125 K, we did not get any lasing, which is mainly limited by the MR reflector bandwidth because the QW emission becomes weak. The LT design cavity has three lasing wavelengths of 1448 nm (at 10 K), 1478 nm (at 50 K), and 1520 nm (at 120 K). One can clearly see that these lasing wavelengths match well with the cavity resonances.

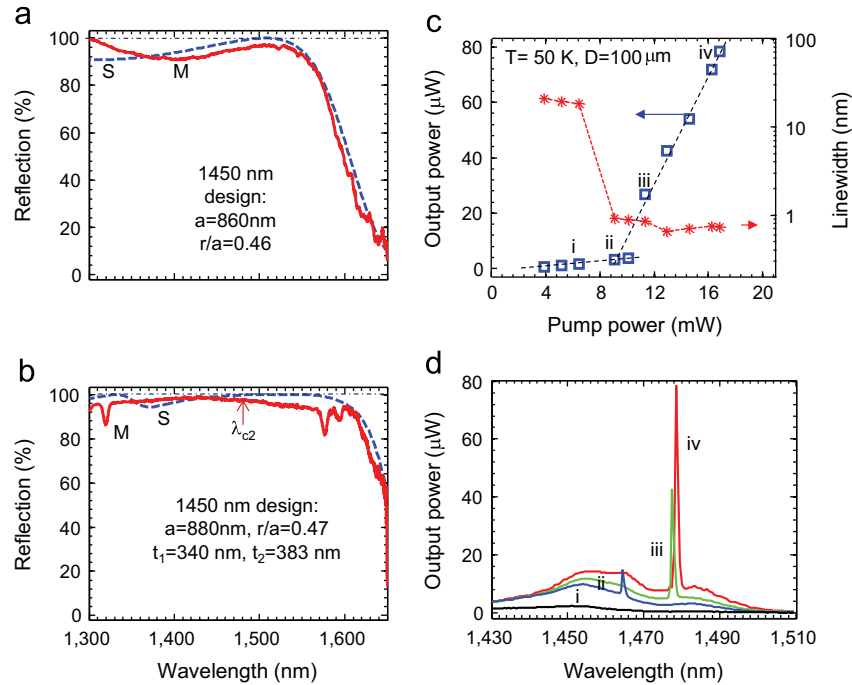


Fig. 41. (a) Reflections of top and bottom membrane reflectors (MR's), and (b) for LT cavity design. (c) The L - L plot (light output for different pump powers) and the corresponding spectral linewidths at $T=50$ K; (d) the measured spectral outputs for pump powers below, at, and above thresholds. Reproduced with permission from [57].

By improving cavity design and thermal engineered layers to achieve better thermal performance, we were able to drastically reduce the lasing threshold [173]. The measured L – L plots are shown in Fig. 42(b) for a MR-VCSEL device under two types of c.w. pumping laser sources at $T=15$ K. By switching the pumping laser sources from 532 nm to 980 nm, the lasing thresholds reduce from 10 mW to 1.9 mW (inset of Fig. 42(b)). The reduction of the lasing threshold is largely contributed to the significant reduction in thermal heating inside the lasing cavity. This is evident from the measured lasing spectral outputs, as shown in Fig. 42(b), where the lasing spectral peaks shifts from 1482 nm (with 532 nm pump) to 1452 nm (with 980 nm pump). Such a large blue-shift in lasing wavelength is a direct result of significantly reduced heat dissipation. Further threshold reduction is possible with much improved cavity design and the incorporation of highly thermal conductive buffer layers. Also shown in Fig. 42(b) are the measured reflection spectra of the top (R_t) and bottom (R_b) Si-MR's used for this MR-VCSEL.

In summary, with the advances in MR design and fabrication, one can expect the performances of the MR-VCSEL to become compatible with or better than the DBR-based VCSEL's, owing to its ultra-compact cavity size and extremely high finesse optical cavity. To realize the full potential of MR-VCSEL's, an efficient electrical injection scheme has to be incorporated. Additionally, the use of low index oxide layer presents a bottleneck in the thermal dissipation of QW active region. Different cavity designs and other types of buffer layer materials need to be explored with a low refractive index, a low optical loss, and a high thermal conductivity.

7. Fano resonance photonic crystal field localization and absorption engineering

7.1. Electromagnetic field localization and enhancement in photonic crystal cavities

Electromagnetic field localization and enhancement in nanoscale structures and cavities have been investigated extensively for enhanced light-matter interactions [161,173,174]. Three types of nano-cavities are being investigated, including photonic crystal bandgap (PBG) defect cavities [175–177], metallic surface plasmon-polaritons (SPP) and optical antennas [177–180], as well as dielectric photonic crystal Fano resonators (Fano). As shown in Table 4, despite different principles and characteristics, these nanophotonic resonant structures do offer promising solutions to the different application requirements.

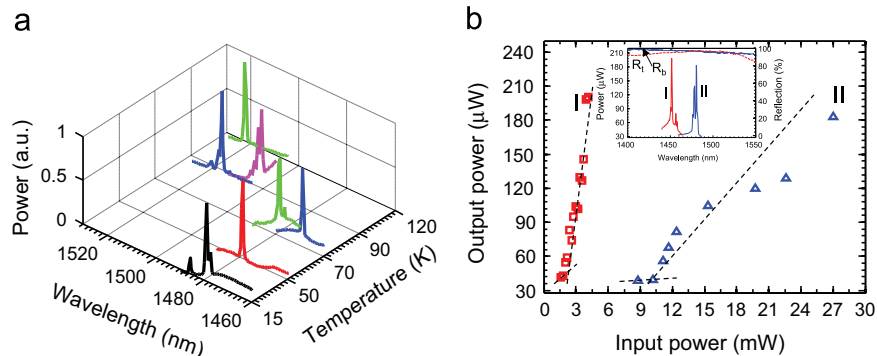


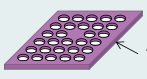
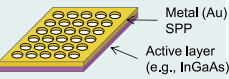
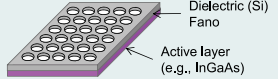
Fig. 42. (a) Measured lasing spectral at different temperatures under 530 nm laser pumping. (b) Measured lasing spectra at $T=15$ K under 532 nm (I) and 980 nm (II) lasers pumping. The inset is the corresponding lasing spectra and the measured reflections of the top and bottom MR's.

Photonic crystal (PC) exhibits photonic band gaps (PBGs) and unconventional dispersion and refractive properties making possible hitherto not realizable optical devices such as ultra-compact routers, and highly wavelength selective and compact add/drop filters [174,181]. Due to the ability to achieve spontaneous emission control [26,143,182], photonic crystal slab (PCS) [18] waveguide cavities have been a subject of active research for ultra-compact high efficiency light sources, with potentially zero threshold [145–149]. Additionally, PC structures can lead to other physical phenomena, such as optical absorption property alteration through photonic density of states (DOS) engineering. Enhancement and suppression of thermal emission and absorption reported so far have been based mainly on the bandedge effect in various metallic PC structures or clusters. Enhanced absorption can happen near or at the band edge where the electromagnetic Bloch wave is still extended throughout the structure, its group velocity is near zero, and the photonic DOS is greatly increased. In this regime, an enhanced light-matter interaction is expected, and enhanced laser gain, light absorption and nonlinear effects have all been proposed [175,178,183–188]. Enhanced absorption in tungsten 3D PC's has been reported [189]. Both theoretical and experimental research has been carried out and confirmed the modification of Planck blackbody radiation [190]. Most of the work done so far has been focused on the absorption change in one-dimensional distributed Bragg reflector (1D DBR) based cavities [185,191], or one-, two- and three-dimensional (1D, 2D, 3D) metallic photonic crystal cavities [178,184,186].

Simultaneous inhibition and redistribution of spontaneous emission in PC has been demonstrated theoretically and experimentally in a lossless dielectric PCS structure [178]. The introduction of an absorption layer in a dielectric PCS structure (e.g. quantum well, quantum dots) can lead to the modification of the absorption characteristics, due to the spectrally-selective light-matter interaction in the cavity. We proposed a photonic crystal infrared photodetector (PCIP) configuration, where the photonic crystal defect cavity was integrated with the quantum dot infrared photodetectors (QDIPs) [182,184] for a higher operation temperature and spectrally selective absorption, which are highly desirable for infrared gas sensing and hyper-spectral imaging. High spectral selectivity with tunable wavelength coverage and spectral width can be feasible based on defect engineering, simple lithographic control, and/or external control.

Theoretical investigations have been carried out on the spectrally selective absorption properties in one- and two-dimensional (1D, 2D) PC structures with and without defect. The work is based on the transfer-matrix method (TMM) [192] and the three-dimensional (3D)

Table 4
Comparison of nano-cavity enhanced photodetectors for multimodal sensing.

	Photonic crystal bandgap defect cavity (PBG)	Metallic surface plasmon-polariton (SPP)	Dielectric photonic crystal Fano resonance (Fano)
Schematic			
Principle	<ul style="list-style-type: none"> Localized defect mode with high field concentration within the slab 	<ul style="list-style-type: none"> Local field enhancement near metal-dielectric interface 	<ul style="list-style-type: none"> Local field enhancement in the dielectric layer or inside the slab
Pros.	<ul style="list-style-type: none"> Potential very high Q and low V Suitable for single photon detection 	<ul style="list-style-type: none"> Suitable for large area detector (arrays) No etching inside active absorption layer 	<ul style="list-style-type: none"> Suitable for large area detector (arrays) Relaxed index contrast requirement (no PBG needed) Flexible integration schemes (inside or above slab) Metal-free pure dielectric structure Capable of spectral, angle, and polarization detection
Cons.	<ul style="list-style-type: none"> Requires large index contrast for PBG formation Etching through active absorption layer Limited detection area 	<ul style="list-style-type: none"> Requires the use of lossy metal Polarization dependent coupling scheme 	<ul style="list-style-type: none"> Sensitive to dispersion properties of the guided modes

finite-difference time-domain (FDTD) [39] technique. The defect-free 1D PC structures, displayed enhanced absorption at either lower or higher frequency bandedges, depending on the relative refractive index of absorptive layers. Wavelength selectivity as high as 40 was observed. For 2D symmetric air hole triangular lattice PC structures [39], enhanced absorption at the defect level was obtained, with the enhancement largely dependent upon the spectral overlap between the absorption material and the defect mode cavity. Complete absorption suppression within the photonic bandgap region was observed in defect-free cavities, and in single defect cavities when the absorption spectral band had no overlap with the photonic bandgap [193,194].

Similar to metallic based plasmonic structures, local field enhancement can also be realized in defect-free dielectric photonic crystal cavities, due to the Fano resonance principles in photonic crystals and metamaterials [195]. Based on the dispersion engineering and modal symmetry properties, local field enhancement can be observed both inside the air holes of the PCS (inside PCS) and right above the PCS (outside PCS), as shown in Fig. 43. Spectrally-selective absorption enhancement can be achieved by incorporating a dispersive medium inside Fano resonance cavities (air holes, Fig. 43(a)) or by placing a thin layer of absorptive material on top of (or below) the dielectric PCS (Fig. 43(b)). We have reported spectrally selective absorption enhancements (>20 times) at near infrared (1550 nm) when PbSe colloidal quantum dots (CQDs) were placed inside the air holes of the Fano resonance Si PCS cavities [195]. We also observed spectral selective absorption enhancement in an ultra-thin InGaAs NM when it was placed on top of the Fano resonance Si PCS structure [80,177]. It was also reported recently that strong field enhancement with high Q factors can be observed in coupled bi-layer structures, with a single top PCS layer (Fig. 43(c)) [196] and double PCS layers (Fig. 43(d)) [38]. By controlling

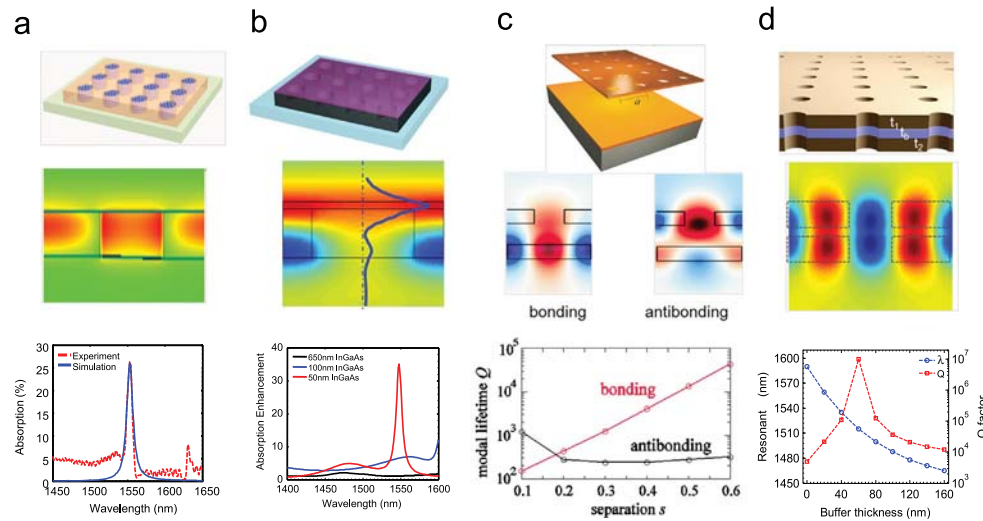


Fig. 43. Localized field enhancements in dielectric photonic crystal slab (PCS) cavities due to Fano resonances: (a) inside the single-layer PCS cavity; (b) above Fano PCS; (c) in coupled single-layer PCS; and (d) in between coupled bi-layer PCSs [38]. Schematics are shown on the top panels, with simulated field distributions shown in the middle panel. Measured and simulated absorption of PbSe CQD inside Si Fano cavity and simulated absorption enhancement of different thickness InGaAs NM transfer printed on top of Si Fano filters are shown in the bottom panel of (a) and (b), respectively. The simulated high Q filter resonance spectral locations and the corresponding Q factors for different separations are shown in the bottom panels of (c) and (d) (reproduced with permissions from [38,195,196]). (a) Field enhancement *inside* single layer PCS, (b) Field enhancement *above* single layer PCS, (c) Field enhancement *in* coupled asymmetric PCS and (d) Field enhancement *between* coupled bi-layer PCS.

the design parameters, the optical Q factors approach infinity with optimal buffer thickness, due to the generation of the coupled dark states [38,120]. Experimentally, we have demonstrated Q factors of 80,000 for a coupled bi-layer PCS Fano filter [38,126,127].

7.2. Demonstration of spectral-selective absorption enhancement and IR detectors

By incorporating a dispersive medium inside the Fano resonance cavities, it is possible to develop ultra-compact infrared photodetectors with spectrally-selective absorption enhancement properties on any substrates for any wavelengths. We have previously reported theoretical work on enhanced IR absorption in defect-free PC cavities, via Fano resonances, due to spectrally-selective light-matter interaction in the cavities.[177,197] Based on the modal properties, two types of cavities have been investigated based on Fano resonance Si-NM Fano filters, with (a) integrated colloidal quantum dots (CQDs) inside the air holes, and (b) InGaAs NM's stacked on top of Si Fano filters. We will review these two types of structures here.

7.2.1. CQD integrated Si-NM Fano filters

We reported direct absorption measurements of solution processed colloidal quantum dots (CQDs) in patterned Si NM PC Fano resonance cavities that are transferred to flexible plastic PET substrates [195]. The Fano resonance filter structure was designed and fabricated on a silicon-on-insulator (SOI) substrate, and subsequently transferred to a transparent and flexible PET substrate [197]. Then, colloidal PbSe CQDs were back-filled inside the air holes of the transferred SiNM PC region. The schematic is shown in the top panel of Fig. 43(a), along with the simulated field profile shown in Fig. 43(b), where the peak intensity of the field is centralized inside the air holes of the Si-NM Fano resonance PCS structure. The measured and simulated absorption spectrum was shown in the bottom panel of Fig. 43(a), where we found a sharp peak at the shifted Fano resonance regime (1550 nm). The measured and simulated spectra match very well.

To further illustrate the interactions between the Fano filters and the CQD's, and also to quantify the changes in the absorption due to the interactions, we introduce an absorption enhancement factor parameter. It is defined as the ratio of the absorption of the CQDs inside Fano filters to that of the CQDs without Fano filters. Fig. 44(a) and (b) show the absorption spectra of three wavelength QDs and the transmission spectra of three Fano filters. Using these QDs and filters, three different cases were studied. For Case 1 (QD1 and Filter 1), there was a very good spectral overlap between the Filter 1 resonance peak and the QD1 absorption around 1550 nm. This overlap leads to an absorption enhancement factor of 9 at the resonance location of Filter 1, as shown in Fig. 44(c). In the second case (Filter 2 and QD2), a Fano filter sample was fabricated with Fano resonance at 1468 nm, by increasing the air hole radius (r) to 149 nm. This sample was filled with another spectrally-matched PbSe CQD (QD2), with their absorption peak at around 1450 nm. Following the same procedure, the absorption enhancement factor was derived and the data were plotted in Fig. 44(c). An absorption enhancement factor of 18 was obtained for this sample, which may be due to the combined effects of a larger air fill factor, a higher quality factor of Fano resonance, as well as a higher quantum efficiency of CQD's in this case.

Another set of Fano filters (Filter 3) was fabricated with Fano resonance of 1564 nm, by reducing the air hole size to a radius of 103 nm. CQD's with an absorption peak at 1640 nm (QD3) were used here, which have no absorption at 1564 nm. In this case, there is no absorption observed around 1564 nm spectral regime. By comparing these three cases, it clearly indicates

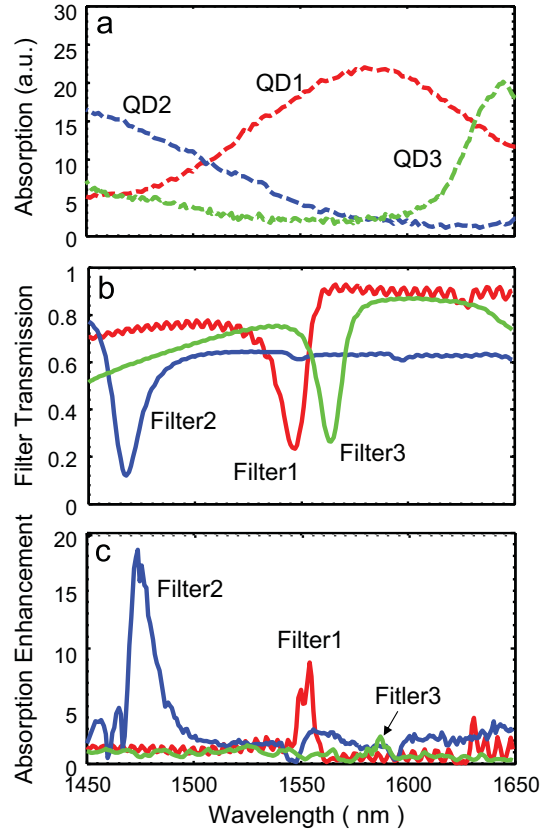


Fig. 44. (a) Three sets of CQD's with different absorption peak locations; (b) three different Fano filters with different resonance locations; and (c) absorption enhancement factors for these three sets of samples. Reproduced with permission from [195].

that the enhanced absorptions at different Fano resonance locations originate from the strong interactions between the absorptive medium (CQDs in this case) and the spectrally matched Fano resonances.

It is also worth noting that the quality factors of Fano resonance in our experiments were far from optimal. According to our earlier theoretical work, one or two orders of absorption enhancement can be expected for the Fano filters with optimized factors [197]. In addition, the fill factor of the CQD's into the air holes of PC cavities can also be further increased.

Another interesting feature for the photodetectors based on Fano resonance filters is the ability of dispersion engineering to achieve the desired angular and polarization properties.[40,96] We experimentally observed a blue-shift (4.5 nm/degree) in absorption resonances for transverse electrical (TE) mode, with the increase of incident angles up to 20° off surface-normal incidence. At the same time, the absorption resonance for transverse-magnetic (TM) mode does not shift much. These experimental results agree well with the simulated absorption properties, based on the RCWA technique. The results also match previously reported results on Fano resonance filters.[96] The spectral shift is largely dependent on the polarization states of the incident beam, the direction of the incident beam and, the phase matching conditions. It is feasible to have

different spectral shifting characteristics, either red- or blue-shifts, at various shift rates ranging from 0.5 to 5 nm/degree [96].

In conclusion, PbSe/PbS CQD absorption characteristics were directly measured inside the air holes of Si Fano resonance filters on flexible PET substrates. The experimental results agree well with the simulation results. Significant absorption enhancements can be found in Fano resonance when the CQD absorption spectrally overlaps with the Fano filter resonance. The study will lead to a new class of photodetectors with desired angular-, spectral-, and polarization-dependent properties and such devices can be used in a wide variety of optical communications, hyper-spectral imaging systems and flexible photonics.

7.2.2. Fano resonance enhanced photonic crystal Infrared Photodetectors

Shown in Fig. 45(a) and (b) are the schematics of the Fano Resonance enhanced Infrared Photodetector and the cross section view of the device showing the Fano filter lattice constant (a), air hole radius (r) and the thicknesses of SiNM (t), InGaAs NM (h) and gold electrodes (g). The filter design and fabrication follows the processes discussed earlier, with Si-NM Fano filters transferred onto glass substrates [41,80,96].

The SiNM Fano filter (h) is 340 nm thick. The square lattice air-hole PC structure has a period (a) of 900 nm, and the air hole radius (r) of 280 nm. A 750 nm thick InGaAs nanomembrane (NM) was then transfer-printed on top of the transferred Si Fano filter on glass. The transferred InGaAs NM was thinned down to 100 nm using BCl_3/Cl_2 plasma reactive-ion etching for optimal absorption enhancement. [80] Shown in Fig. 45(c) is a top view scanning electron micrograph (SEM) of the 100 nm thick InGaAs NM on top of the Si Fano filter on the glass

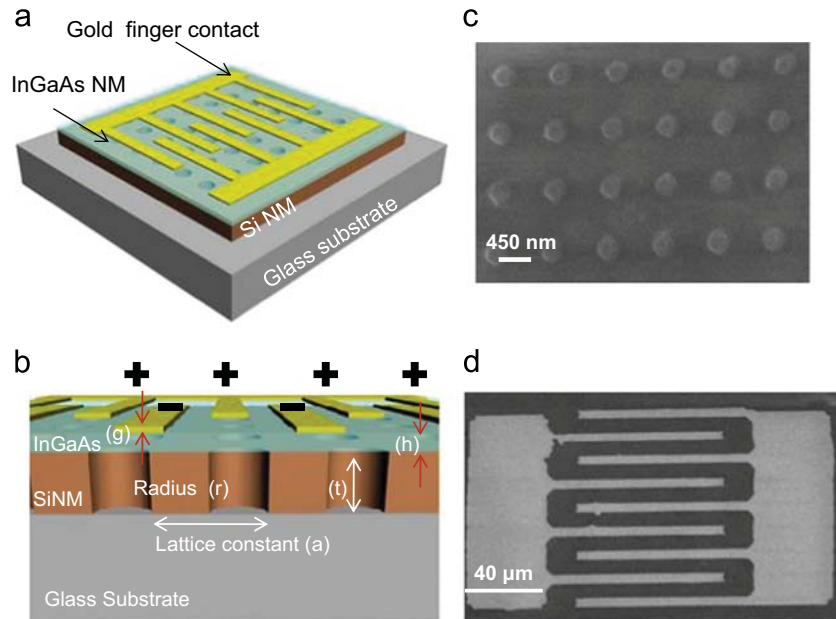


Fig. 45. Schematic of (a) SiNM Fano photodetector; and (b) cross section schematic of Fano PD showing air hole radius (r), lattice constant (a), thickness (t) of SiNM, and thickness (h) of InGaAs layer. (c) Top view scanning electron micrograph of the 100 nm thin InGaAs NM on Si resonant filter and; (d) the 10 nm thick interdigitated Au finger contact on InGaAs NM.

substrate. The Schottky metal contacts were made using thermal evaporation of 10 nm Au. The active area of the photodetector is $100 \times 100 \mu\text{m}^2$. The anode and cathode are formed by interdigitated finger contacts with spacing of $6 \mu\text{m}$, as shown in Fig. 45(d).

A broadband white light source is generated from a quartz tungsten halogen lamp that is collimated by a collimator. A 50/50 beam splitter is used for transmission and reflection measurement. The transmission and reflection measurements were done on the InGaAs nano membrane on and off the SiNM Fano resonance filter, without metal electrodes. It is also possible to design a filter with negligible absorption at resonance. Shown in Fig. 46(a) is the measured percentage of absorption in the 100 nm InGaAs NM on and off the SiNM Fano resonance filter. In all the cases, the absolute absorption is calculated by subtracting the transmission and reflection spectrum from unity. An optical band pass filter with a central wavelength of 1520 nm, with a FWHM of 10 nm, was used for the photocurrent characteristics. Photodetector performance was characterized after the incorporation of finger contacts. Shown in

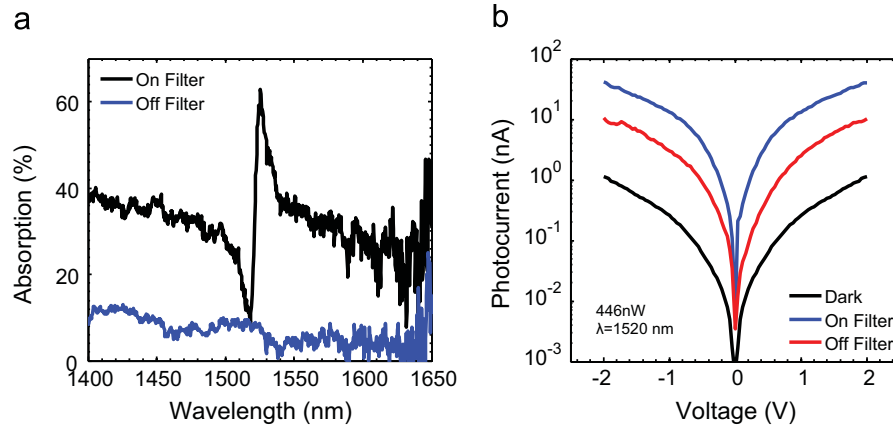


Fig. 46. Measured (a) absolute absorption in percentage and (b) photocurrent in the 100 nm thin InGaAs MSM PD on and off the SiNM Fano resonance filter.

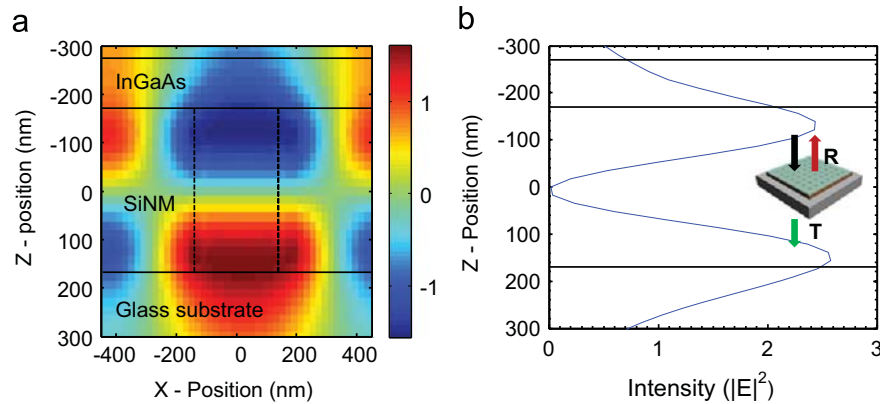


Fig. 47. (a) A cross-sectional view of the FDTD calculation of the electric field in the vicinity of the Fano resonance membrane at resonance. (b) The intensity distribution through the center of the unit cell. The inset shows the orientation of the Fano resonance enhanced MSM PD.

Fig. 46(b) is the measured photocurrent at the resonant nanomembrane wavelength. All the measurements were performed for normal light incidence. An optical attenuator was used to measure the photocurrents at various incident power levels.

When the light couples into the discrete modes of the photonic crystal, the resonant field decays away from the interface of the filter and a strong field region penetrates the InGaAs NM. Thus there is an increased light matter interaction. The resonant coupling of the Fano filter increases the absorption of the 100 nm InGaAs NM from 7% to 64% (Fig. 46(a)). This is primarily due to the overlapping of the spatial mode of the Fano filter onto the 100 nm thick InGaAs NM. The amount of the absorption enhancement depends on the filter's modal property. In Fig. 47, we show the electric field profile obtained at the Fano resonance wavelength with the finite-difference time domain (FDTD) method. This increased light matter interaction increases the photo generated carriers for the same amount of incident power and hence would increase the responsivity of the photoconductive devices.

Shown in Fig. 48 is the responsivity and responsivity enhancement of the InGaAs MSM PD on and off the Si Fano resonance membrane. The responsivity enhancement is defined as the ratio of the responsivity of the MSM PD on the Si Fano resonance membrane to the responsivity

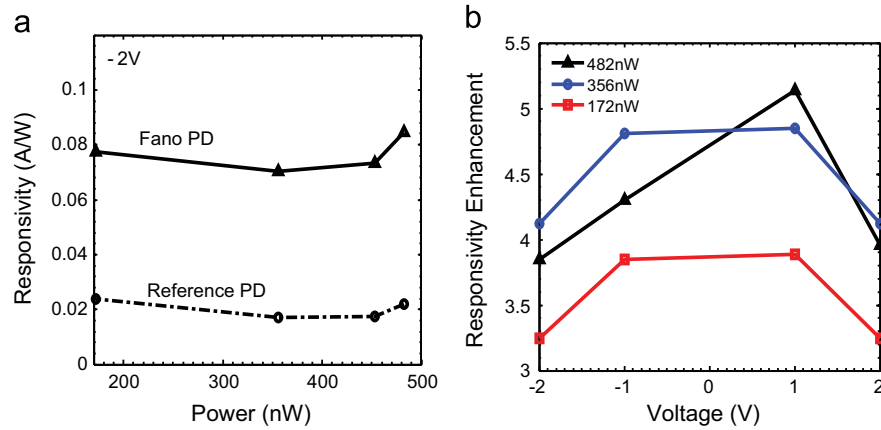


Fig. 48. (a) Measured responsivity of the InGaAs Fano Photodetector (solid) and reference PD (dash) at -2 V. (b) The measured responsivity enhancement at 1523 nm for various power levels.

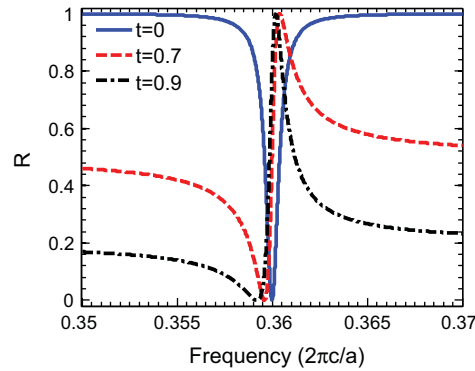


Fig. 49. Simulated Fano resonance line shapes with different symmetry.

of the MSM PD off the Si Fano resonance membrane. The leaky modes from the Si Fano resonance membrane significantly increase the amount of time light spends within the detector active region, and therefore enhances the probability of detection. It is also worth noting that the quality factors of Fano resonance in our experiments were far from optimal. According to earlier theoretical work, it is possible to design an extremely high Q filter. [80,198] With optimized quality factors it is possible to achieve one or two orders of absorption enhancement.

In summary, we have designed and fabricated a stacked ultra-thin InGaAs/Si Fano resonance membrane photodetector. We demonstrate a 3.8 responsivity enhancement at the Fano resonance wavelength. The bandwidth of the MSM detectors is limited by the transit time which can be overcome by reducing the finger spacing. Although we demonstrate the detector at the IR region, the spectral resolution and tunability can be accomplished by controlling the cavity Q and resonant peak location by changing the r/a ratio of the photonic crystal. The Fano resonant membranes can potentially be transferred on a range of foreign substrates including plastics thereby creating potential for flexible nano photonics.

8. Fano resonance photonic crystal sensors

8.1. Asymmetric Fano resonance line shape and high Q cavities

The cavity characteristics of photonic crystals are very sensitive to the lattice parameters, as well as the environment (i.e. refractive index change). Sensors can be either based on in-plane guided modes and photonic bandgaps in PCS's with in-plane light coupling into high index dielectric slabs [199,200], or based on a Fano resonance in PCS with light coupled from out-of-the-plane directions. Fano resonance based sensors are very favorable due to their much simpler and morerelaxed alignment for light coupling to PCS structures from out-of-the-plane (e.g. surface normal) directions.

As discussed earlier in Section 2, the Lorentzian resonance is one fundamental resonance with a symmetric graph. In contrast, the Fano resonance exhibits a distinctly asymmetric shape as described in Eq. (10). Shown in Fig. 49 are cases of $t=0$, 0.7 and 0.9, respectively, with $\omega_0=0.36(2\pi c/a)$, and $\tau=2.5 \times 10^3(a/2\pi c)$. One can see when $t=0$, the formula becomes Lorentzian and the graph symmetric. When t increases, the graph becomes more asymmetric and the width of the line becomes sharper. The shape of the graph for the Fano resonances ($1 > t > 0$) are much sharper than the Lorentzian graph although they possess the same life time factor τ or

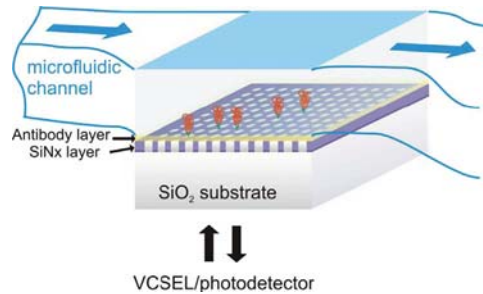


Fig. 50. Schematic of an integrated 2D PCS Fano resonance microfluidic bio-sensing system: Analyte is detected by measuring a change in the local index of refraction due to captured molecules on the biosensor surface. Reproduced with permission from [205].

the quality factor Q . This unique feature significantly reduces the frequency shift required for on/off switching and also allows more energy efficient operation in optical sensor applications [38,120,201–203].

For more practical applications of Fano resonances in optical sensors, the sensitivity related to the on/off switching ratio also needs to be improved, i.e., the width of the line for the resonance or the quality factor Q . As discussed in Section 4, there are two general design directions to improve the quality of 2D PCS based optical filters/sensors. For a single layer slab, using relatively small air holes (or small r/a ratios) can achieve a higher Q , but the size of the air hole radii will be limited by fabrication resolution. On the other hand, coupled bi-layer PCS Fano filters can have Q factors much higher than single layer PCS Fano filters, due to the bright or dark states arising from the coupled bright or dark resonances, as discussed in Section 4. Theoretically, by optimizing the lattice parameters and the buffer layer thicknesses, one can achieve very high or infinite Q 's.

The nature of the PCS Fano guided modes has significant implications regarding spectral sensitivity, limit of detection, substrate presence, and the range of detectable analytes [8,9,41,126]. The increase in the optical Q factors can also lead to enhanced localized field distribution, which can be designed for increased sensitivity because of the increased light-matter interactions. With the design optimization of Fano resonance modal properties, enhanced sensitivity is feasible when the analyte material is placed in the high field concentration region. This was discussed and reviewed in Section 7, for spectrally selective absorption enhancement and photo detector applications. Beheiry et al. [204] reported sensitivity enhancement in Fano resonance filters for biosensing applications. Three-fold spectral sensitivity enhancement is demonstrated for suspended PCS structures. They also reported that the sensitivity is very sensitive to the polarization states.

In summary, optical sensors can be constructed based on the following Fano resonance characteristics:

- (1) High sensitivity based on the spectral shift associated with asymmetric Fano resonance line shapes.
- (2) Enhanced sensing based light-matter interactions associated with a high Q cavity and localized field enhancement.
- (3) High sensitivity based on displacement in coupled Fano resonance PCS cavities.

8.2. Fano resonance PCS sensor configurations

Based on the effect of Fano resonances and different Fano tunable mechanisms, many types of sensors have been proposed and developed, such as refractive index sensors [205], displacement sensors [204], etc.

Levi et al. [205,206] reported an all-dielectric, transparent 2D PCS based sensor that detects index-of-refraction changes in an aqueous solution utilizing guided resonances or Fano resonances. The resonant peak widths and the expected peak shifts were designed with a 0.2 nm spectral line, which is the width of a typical VCSEL light source, in mind. The measured peak shift $\Delta\lambda=0.2$ nm corresponds to a detectable index change $\Delta n=1.5 \times 10^{-3}$. This filter can be combined with an optical readout module including a light source, a detector, and micro-optics to form a miniature integrated biosensor. This enables reduced cost, small sample volume, and

increased speed and parallelism, all of which are desirable for high throughput analysis in medical diagnostics. As shown schematically in Fig. 50, the excitation and detection of PC slab resonances occur perpendicular to the sample. Light from the underlying laser is visible on a SiN_x PC slab over a SiO₂ substrate, and is reflected back vertically to the detector. Interference between the original beam and the light coupled with guided modes introduces Fano-resonance peaks in the reflection spectra. Consequently, the laser-detector module observes reflection changes when an analyte binds to the PC slab surface. The analyte binding can be mediated through antibody–antigen reactions as indicated in Fig. 50, or through other techniques.

Huang et al. [207] reported reflectance-based Fano resonance PCS sensors made of 2D TiO₂ nanopillar arrays. Such a reflectance-based structure with a large functional area not only simplifies the optical guiding but also enhances the sensor signal. A linear shift of reflectance peaks is found for liquids with refractive indices varying from 1.333 to 1.390 at a wavelength near 1500 nm. The sensor system and related results are shown in Fig. 51, where one can see that when the sugar concentration in the solution is increased, the reflection peak moves from a short wavelength to a longer wavelength.

Another type of Fano sensor is designed based on the Fano resonance shift in which the displacement of the coupled PC cavity structure is induced by the surrounding pressure or temperature changes [126]. Fig. 52(a) shows the sensor structure of a set of coupled PC slabs with a gap in-between. The incident light shines vertically from the top. When the gap is larger than $0.5a$, where a is the PC lattice constant, this coupled device works like an FP cavity with two mirrors, such that the coupling between the two slabs is primarily due to the propagating waves, and the transmission or reflection spectra is independent of the lateral alignments. Shown in Fig. 52(b) are the transmission spectral shifts (red to blue) with a reduced gap. When the reflectivity for each slab is high, the transmission becomes highly sensitive to the longitudinal displacements. When the gap becomes very small, the evanescent tunneling and near-field coupling between the slabs become important, and the spectrum is much more sensitive with the lateral displacement, as shown in Fig. 52(c), where the gap is $0.1a$ and there is a lateral shift of $0.05a$ along the (10) direction. One can see the shift of the Fano resonances between when comparing the two cases. Using these features of Fano resonance related to displacement to detect the surrounding pressure or temperature change will be much more effective than conventional FP sensors. Sha et al. [208] reported an experimental demonstration of highly sensitive displacement sensors based on this principle using microwave bands. In addition, the

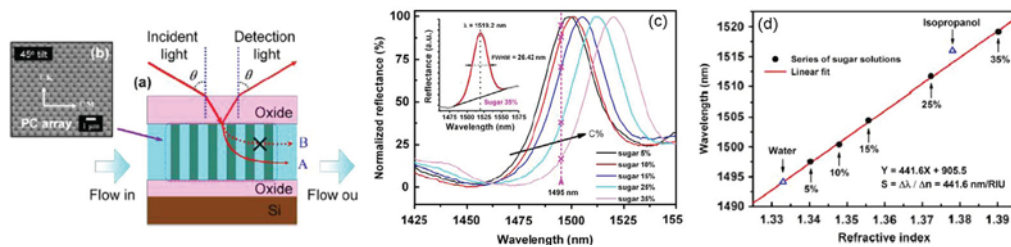


Fig. 51. (a) Schematic drawing of the reflectance-based PC liquid sensor; (b) SEM image of the uniform and smooth TiO₂ nanopillars array. The pillar height is 950 nm, the pillar radius is 225 nm, and the chamber volume is ~ 4 nL. (c) Normalized reflectance curves of different concentration sugar solutions tested with the PC liquid sensor. Inset: one example showing the Gaussian fit of the reflectance peak for determining the exact peak position. (d) Measured peak positions of 5–35% sugar solutions together with water and isopropanol versus their refractive indices. The linear fitting slope indicates a sensitivity of 441.6 nm/RIU. Reproduced with permission from [207].

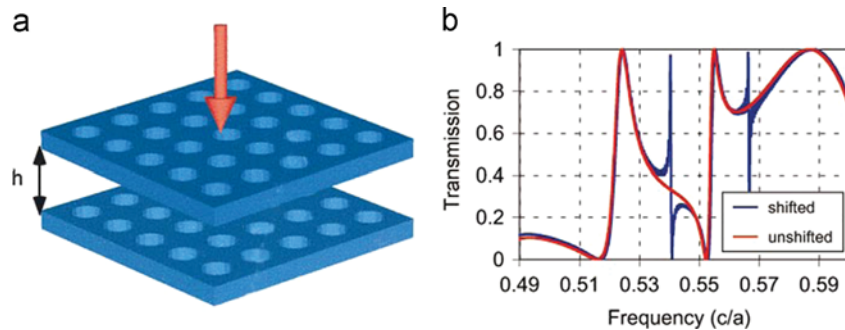


Fig. 52. (a) Schematic of a displacement-sensitive photonic crystal structure. The structure consists of two photonic crystal slabs. The red arrow represents the direction of the incident light. The transmission spectrum of the normal incident light is strongly influenced by the spacing (h) between the slabs. (b) Transmission spectrum through two-slab structures. The spacing between the slabs is $0.1a$. The red curve corresponds with a structure with holes in two slabs aligned to each other vertically. The blue curve corresponds to a structure with a lattice of holes in the top slab shifted by $0.05a$ along the (10) direction with respect to the bottom slab. Reproduced with permission from [126].

acoustic sensor reported by Kilic et al. [209] used a Fano mirror placed at the end of an optical fiber, making it similar to this kind of coupled Fano PC cavity structure.

9. Fano resonance photonic crystal cavity optomechanics

9.1. Optical forces in nano-scale cavities

Maxwell, dealing mathematically with the stresses in an electro-magnetic field, reached the conclusion that “in the medium in which waves are propagated there is a pressure normal to the waves and numerically equal to the energy in unit volume” [209]. Universal to physics from mesoscale and microscale down to nanoscale, optomechanical interactions are a rich subject of research and enable an especially rich set of phenomena and opportunities because of the presence of both attractive and repulsive forces [210]. Rapid developments have been made in this area in the past decade. Efforts were made to higher optomechanical coupling coefficients and several experimental demonstrations and approaches for enhancing the strength of the effect were achieved during 2007–2009 [210].

Optical forces resulting from interacting modes and cavities can scale to remarkably large values as the optical modes shrink to nanometer dimensions [211]. It has been noted that the remarkable spatial confinement and large field enhancements afforded by nanometer-scale guided modes can result in significant forces when optical modes and cavities interact [212,213]. Scaled down to nanoscale dimensions, transverse optical forces in an integrated silicon photonic circuit through an embedded nanomechanical resonator were reported in 2008 [214]. In addition, intensive progresses were made in 2009. Both attractive and repulsive optical forces can be obtained between planarly coupled nanophotonic waveguides [215]; force is tuned from attractive to repulsive by controlling the relative phase of the optical fields injected into the waveguides [216]. A static mechanical deformation of up to 20 nm in a silicon nitride structure was experimentally demonstrated in the stacked double ring resonator structure with resonance shifting spanning 80 times the intrinsic resonance linewidth with low optical power [217]. Micrometer-scale displacements of the waveguide are observed for milliWatt-level optical input

powers in a structure with a high- Q optical microresonator coupled with a micrometer-scale waveguide [218]. Seamless wavelength routing over a range of 3,000 times the intrinsic channel width was achieved in a specially designed nano-optomechanical system [219]. Eichenfield et al. proposed the idea of “optomechanical crystals,” i.e., that in a photonic crystal, the periodicity of the host medium is used to manipulate the properties of light, whereas a phononic crystal uses periodicity to manipulate mechanical vibrations [220]. A picogram- and nanometer-scale in a photonic-crystal optomechanical cavity was measured in a pair of specially patterned nanoscale beams, resulting in a scale of the per-photon force and the mass of the structure [221].

All of these results indicate that there is potential for radiation pressure actuated devices to be used in a variety of photonic applications, such as channel routing/switching, buffering, dispersion compensation, pulse trapping/release, widely tunable lasers, and other light signal manipulations on chip [222].

9.2. Optical forces in coupled Fano resonance PCSs

This concept was extended to 2D PCS's where the radiation force can be further enhanced due to the stored and strongly localized electromagnetic field inside the PCS's. Many systems have been investigated, including coupled waveguides, waveguides coupled to substrates, as well as a variety of resonator structures such as micro-rings, disks or toroids that support whispering gallery modes, and point defects in photonic crystal slab structures that support standing-wave optical modes. Recently, the behavior of lateral and normal optical forces between coupled photonic crystal slabs attract a lot of interest, because near the frequencies of guided resonances, we see significant enhancement of the optical forces [120,223].

Optical forces in coupled photonic crystal slabs have received a great deal of attention recently [125,196,223,224]. It was shown theoretically that resonances arising from coupled photonic crystal slabs can generate optical forces that are proportional to the quality factor of the resonances [120]. These forces can be attractive or repulsive and may also be engineered in asymmetric structures [196]. We will first review some of the basic principles for manipulating optical forces in coupled slab structures, as shown in Fig. 53. Due to their different origins, the two types of dark states in Section 4.2 exhibit qualitatively different force divergence behaviors. Three cases were considered [120].

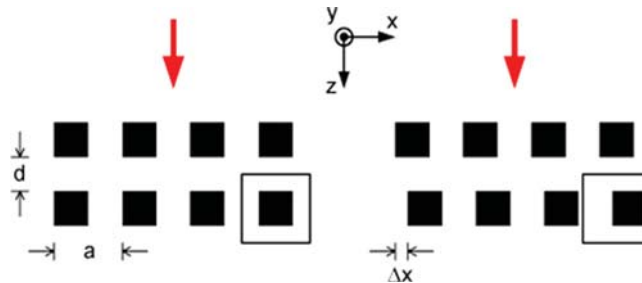


Fig. 53. Schematic of the double slab system. The red arrows indicate the directions of the incident light. Each slab consists of an array of high index rods ($\epsilon=12$) surrounded by air ($\epsilon=1$). The empty rectangle indicates the surface over which the integration of the stress tensor is performed. In the right panel, the bottom slab is shifted relative to the first slab by a distance of Δx . Reproduced with permission from [120].

In the first case shown in Fig. 53(a), we consider the dark resonance from coupled bright resonances as in Fig. 17. As the slab separation is changed, the quality factor of the dark resonance becomes finite. The resonant properties are plotted in Fig. 54. Since the resonant decay rate must vanish at the separation, during which the resonance is decoupled from radiation, the lowest order term in the resonant decay rate is proportional to the square of the separation. Hence the optical force, proportional to the quality factor, diverges quadratically with respect to the separation (Fig. 55).

In the second case, shown in Fig. 53(b), we consider a dark state from coupled dark resonances as in Fig. 16. With a relative shift, the dark state splits into two near-dark resonances, and the resonant properties of these two near-dark resonances are plotted in Fig. 56. The quality factor diverges as Δx^{-2} , which is the lowest order of dependence. The normal force, F_z , diverges in the same way as Q , but the lateral force, F_x , diverges as Δx^{-1} because the average lateral force per photon to the lowest order is proportional to Δx . The divergence behavior of the optical forces is plotted in Fig. 57.

In the third case, we consider a dark state from coupled bright resonances, similar to Case 1, except that the two slabs are shifted relative to each other by $0.2a$, where a is the lattice constant.

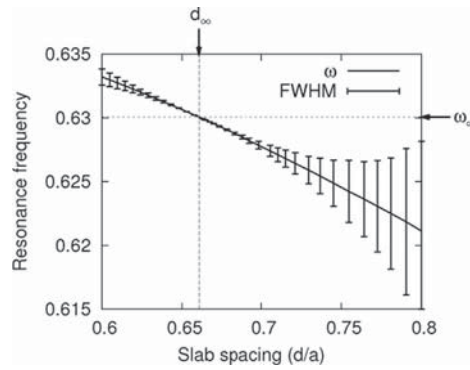


Fig. 54. Resonance peak and linewidth in the vicinity of the dark state arising from coupled bright resonances as in Fig. 17 (Case 1). Reproduced with permission from [120].

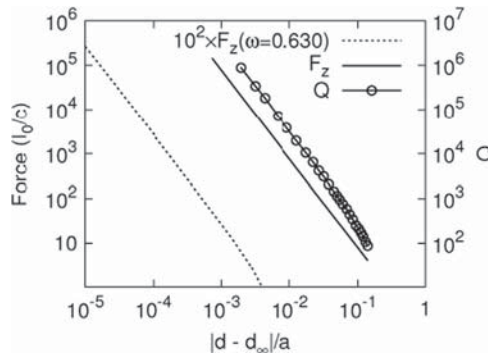


Fig. 55. Divergence behavior of normal force on resonance compared to the Q as the slab spacing is varied away from the dark state in Case 1. For reference, the force variation at a constant frequency near the dark state frequency is also plotted with a dashed line. Reproduced with permission from [120].

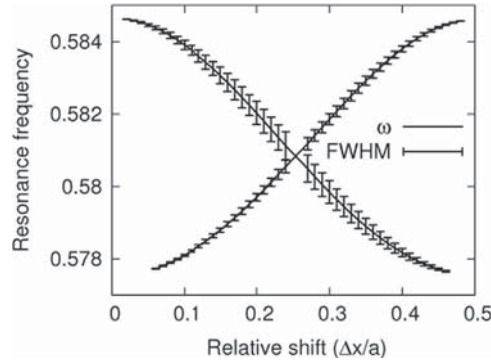


Fig. 56. Resonance peak and linewidth in the vicinity of the dark state arising from coupled dark resonances as in Fig. 16 (Case 2). Reproduced with permission from [120].

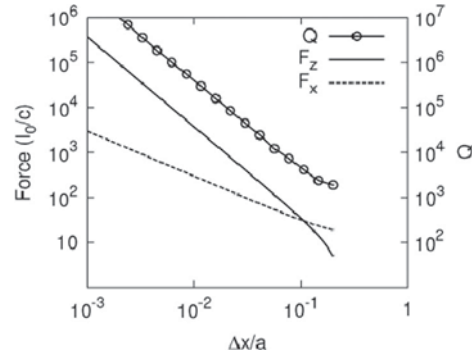


Fig. 57. Divergence behavior of normal and lateral forces on resonance compared to the Q for various shifts near the symmetry point $\Delta x=0$ for Case 2. Reproduced with permission from [120].

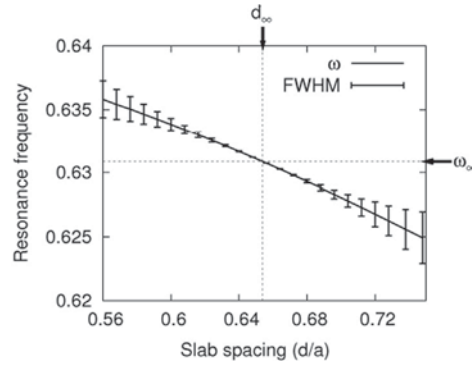


Fig. 58. Resonance peak and linewidth in the vicinity of the dark state for Case 3 at $\Delta x=0.2a$. Reproduced with permission from [120].

A dark state still exists, as seen in Fig. 58. As the slab separation is changed, both the normal force, F_z , and the lateral force, F_x , vary in the same way as Q , inversely proportional to the square of the separation (Fig. 59).

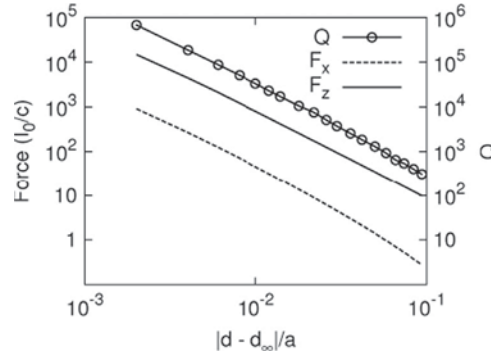


Fig. 59. Divergence behavior of normal and lateral forces on resonance compared to the Q for various slab spacings near the dark state in Fig. 16. Reproduced with permission from [120].

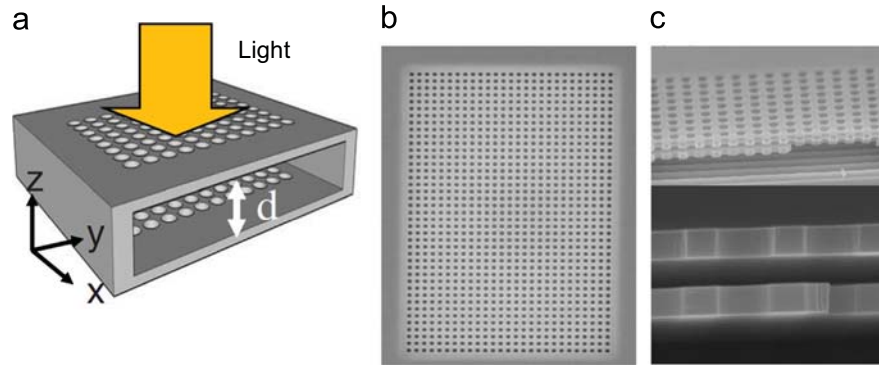


Fig. 60. (a) Schematics of the experiment. The structure is fully clamped (all-side clamped); (b) top-view scanning electron microscope image; and (c) bird's-eye view (upper) and cross section (lower) of a bilayer PCS. The period is 750 nm and the hole radius at the center is 270 nm. Reproduced with permission from [225].

In conclusion, in a coupled photonic crystal slab system, the optical forces are strongly influenced by the symmetries of the system as well as its resonance properties. It is worth noting that these proposed structures can lead to enhanced light-induced pressure over larger areas, in a configuration that is directly accessible to the externally incident, free-space optical beams. The force scales with the Q of the resonances in the structure. By placing the system configuration in the vicinity of a dark state, a dramatic enhancement of the optical forces may be obtained due to the large resonant enhancement of the fields.

Followed by initial theoretical investigations of high- Q and strong optomechanical coupling in defect-mode double-layer PCS cavities [223], Notomi et al. [225] reported an experimental demonstration of strong optomechanical interactions in InP-based defect-free bi-layer PCS cavities, based on bandedge or Fano resonance modes. Significant radiation force of the stored light (F) should appear as the electromagnetic energy stored in the cavity (U) changes with the change in spatial separations (z) between two coupled PCS slabs, as shown in the following

equation:

$$F = -\frac{dU}{dz} = -\left(\frac{U}{\omega}\right)\left(\frac{d\omega}{dz}\right) = -\left(\frac{PQ}{\omega^2}\right)\left(\frac{d\omega}{dz}\right)$$

where z is the spatial coordinate of vertical direction, and the electromagnetic energy stored in the cavity is $U = N\hbar\omega_c = PQ/\omega$. P is the incident optical power. For the mode with $(d\omega/dz) > 0$, $F < 0$, attractive force appears between the two PCS's. Based on the modal dispersion properties [223], the estimated radiation force per unit of electromagnetic energy in the cavity is $\sim 0.23 \mu\text{N/pJ}$, with the force estimated to be $\sim 0.4 \mu\text{N/pJ}$. For an incident power of 19.7 mW, a displacement of 3.6 nm was obtained for a cavity Q of 1600 at 1568 nm, as a result of an optical force of 10.8 nN (Fig. 60).

Theoretical analysis showed that the optical force is periodic, corresponding with displacement, resulting in stable and unstable equilibrium positions. Both attractive and repulsive force were induced depending on the spatial symmetry of the stored electromagnetic field profile in the double-layer PC slab cavities and air-slot cavities [225].

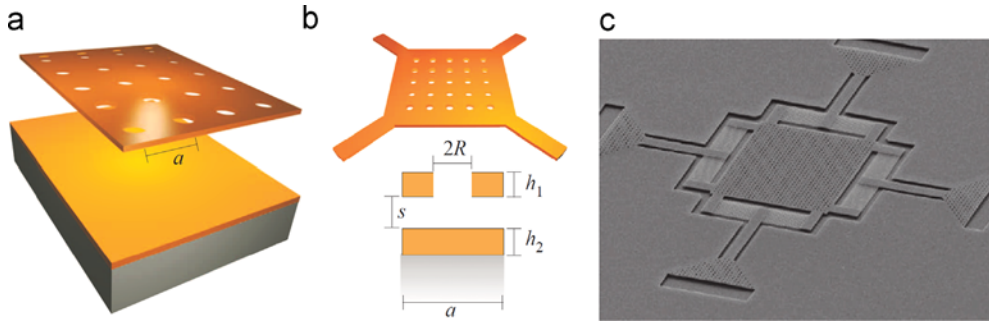


Fig. 61. (a and b) Schematic and (c) SEM image of single-membrane (asymmetric) structure: a photonic-crystal (holey) membrane consisting of a square-lattice of air holes on silicon is suspended (separation s) on top of an unpatterned (homogeneous) silicon slab (thickness $h_2 = 0.2a$) sitting on top of a semi-infinite silica substrate. Light is apparent on the membrane from the normal direction (top). Key parameters are: $a = 920 \text{ nm}$, $R = 207 \text{ nm}$, $h_1 = h_2 = 185 \text{ nm}$, and $s = 265 \text{ nm}$. Reproduced with permissions from [196,226].

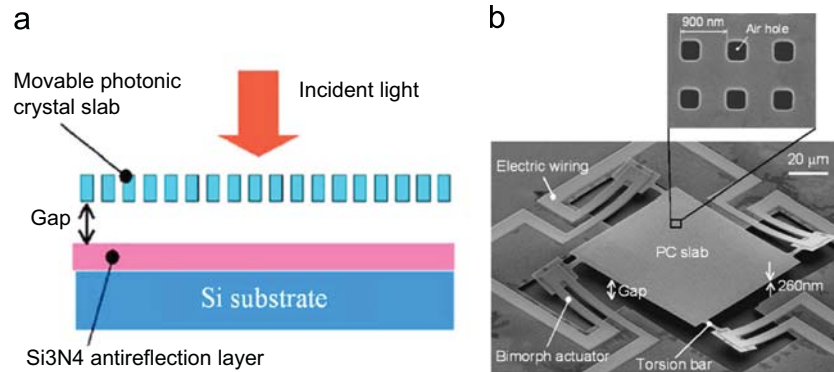


Fig. 62. (a) Cross section diagram of the MEMS tunable Fano filter design; and (b) SEM image of the fabricated Fano filter. The inset shows the magnified view of the fabricated PC slab. Reproduced with permission from [43].

Similar to the symmetric double-layer PCS systems, tunable attractive and repulsive forces can also arise in highly asymmetric structures coupled with external radiation. One recent theoretical study by Rodriguez et al. [196] shows this generality by demonstrating that tunable attractive and repulsive forces can also arise in highly asymmetric structures coupled with external radiation (Fig. 61(a)). Recently, Hui et al. [226] reported an experimental observation of repulsive forces with a displacement of 1 nm/mW in such an Si based hybrid PCS membrane/unpatterned Si membrane cavity (Fig. 61(b)). It is also predicted that such configurations can extend the displacement range to many tens of nanometers, providing a simple, non-intrusive solution to extending the actuation range of MEMS devices.

9.3. Optomechanical control and MOMES applications

There is a variety of all-optical operations that can be created by this method, ranging from all optical switching and tuning (for telecom, sensing and imaging applications) to adaptive dispersion and filter synthesis (for applications such as adaptive filtering of laser lines and optical clock recovery). Microelectromechanical systems (MEMS's) are the promising mechanisms for introducing variable functions into PC devices. Although several devices with variable structures of PC slabs combined with MEMS were considered, there have been very few reports on the experimental studies because of the difficulty in fabricating hybrid structures [196,226]. A few experimental results, as well as principle design, have been reported [124,227]. In order to introduce variable function to the Fano resonances in PC slabs, Suh et al. [126] studied two PC slabs facing each other analytically for a wavelength-tunable PC filter. Kanamori et al. [43] experimentally demonstrated a wavelength-selective variable reflection filter controlled by changing the gap with a microelectromechanical actuator (Fig. 62).

10. Fano resonance photonic crystal slowlight and nonlinearity

10.1. Slowlight and stopping light in Fano resonance photonic crystals

In the next-generation of information networks, path switching of optical packets at network nodes will be very important, and solutions that can perform the task with a high data rate, high throughput, and low power consumption are required. The ability to drastically slow down the propagation speed of light, and to coherently stop and store optical pulses, holds the key to the ultimate control of light, and has profound implications for optical communications [43,228,229].

PhC structures, which give the dispersion of the allowed propagation frequencies as a function of the propagation vector k , determine the group velocity with which an optical wave packet propagates inside a medium. This frequency (energy) dispersion for photons also determines the effective index and effects related to it (such as refraction, collimation, etc.). Both group velocity (v_g) and group velocity dispersion (GVD) play an important role in light propagation. In general, there are a lot of band portions or positions where the band slope is flat, which makes v_g anomalous. At the band edge v_g should become extremely small ($v_g \sim 0$). Such a flat energy portion is also encountered at both the maximum and minimum points of the lower and upper bands resulting from an anti-crossing between two bands with the same symmetry. There are many bands where v_g becomes negative. These are called group velocity anomalous (GVA) [230]. This effect has been applied towards the realization of light sources and slow light waveguides, with enhanced interaction time between the matter and the cavity [231–233]. Slow

light effect has been investigated extensively in various nano-scale photonic structures with extremely strong material dispersion properties, such as high index photonic wires, coupled-resonators, photonic crystals, and metamaterials.

The PhC structures always support the slow light $v_g \sim 0$ at the band edge with only a single wave vector. Therefore, it is not yet sufficient for stopping light, for that one needs to be able to reduce the group velocity to zero for an entire range of wave vectors. So, Yanik et al. [228] proposed a resonant optical structure which can change its bandwidth dramatically and generate sharp tunable resonances through Fano interference. To illustrate the interference process, they considered a basic building block, as shown in Fig. 63, that consists of a resonator A that is directly coupled to a waveguide, and one or more side cavities B_i that are side coupled to the waveguide of cavity A. The presence of such multiple resonance pathways leads to Fano interference. Based on the coupled-mode theory, they calculated the transmission spectra through this system with a single side-cavity B_1 . The spectra are calculated for photonic crystal structures shown on the right sides of the figures. The gray dots represent the position of the dielectric rods in a perfect crystal. By tuning the dielectric constant of the defect rod, the lower-frequency eigenstate of the system exhibits a dramatic bandwidth variation, as seen in Fig. 63(b and c), where the field patterns that correspond to the lower frequency transmission peak are also shown on the right side. The system can be implemented for the all-optical bandwidth modulations and light stopping schemes. Miroshnichenko et al. [234] proposed a concept of the Mach–Zehnder–Fano interferometer by inserting a cavity exhibiting Fano resonance into a conventional interferometer. By employing the scattering-matrix approach, they demonstrated that the transmission becomes sensitive to the position of the cavity such that an asymmetric structure exhibits a series of narrow resonances with almost perfect reflection.

10.2. Bi-stability, switching, and modulation

Among the great diversity of nonlinear processes in optics, nonlinear dynamic phenomena such as bistability and excitability have recently received considerable attention. Optical bistability is the simplest and most robust paradigm for the realization of all-optical transistors and memories. Two ingredients are needed to obtain bistable operation in an optical system: a

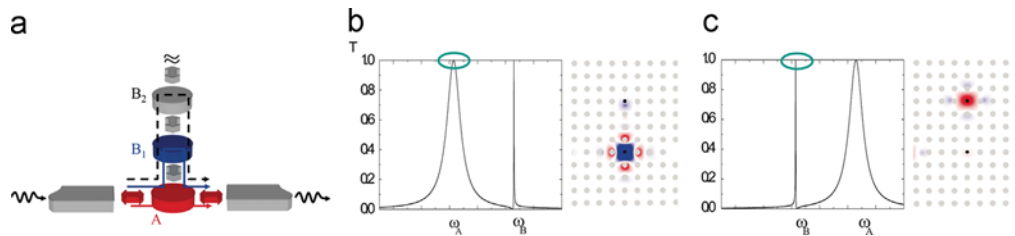


Fig. 63. (a) The basic building block of the all-optical stoplight system. The disks represent cavities, and the arrows indicate available evanescent coupling pathways between the cavities and the waveguides. A waveguide cavity A is inserted into a waveguide, and one or more side cavities B_i are side-coupled to A. Photons tunnel through multiple pathways indicated by black, blue, and red lines, resulting in Fano interference that is tunable by adjusting the resonant frequency of the cavities. (b and c) Transmission spectra through the system of (a), but with a single side-cavity B_1 . Notice the dramatic variations of the width of the lower-frequency transmission peak as a function of the resonant frequencies. Reproduced with permission from [228].

resonance capable of localizing the light intensity in the spectral domain, and a nonlinear property that changes the spectral response as a function of the light intensity. Under certain conditions during the injection of a nearly resonant beam, two stable states for the transmission/reflection through the device can coexist. Since the seminal works of Gibbs in the late 1970s [235], considerable effort has been devoted to the development and optimization of nanocavities for bistable operation [228,236]. Modern design of nanocavities allows high quality Q factors that dramatically reduce bistability thresholds, which are calculated as V/Q^2 , with V referring to the optical mode volume and Q referring to the cavity quality factor [237–240]. Since Fano resonance is much more sensitive than the Lorentzian resonance due to the sharper lines in its graph, it can also reduce the frequency shift requirements for nonlinear switching [241]. According to this unique feature of Fano resonance, many authors have investigated the optical bi-stability, switching and modulation properties by introducing the nonlinearity into material [241–249]. Optical bistability involving Fano resonances due to the Kerr effect in photonic crystal cavities has been theoretically studied based on Green's functional solution of Maxwell's equations [243]. Fano resonances have also been studied using the transfer matrix technique [8,250], and coupled-mode equations [29].

Yacomotti et al. [236] reported experimental demonstration of all-optical bistability in an InGaAsP QW-based 2D PCS structure lying on top of a Bragg reflector (Fig. 64). Bistability was obtained around 1550 nm, using a low group velocity mode at the band edge of the photonic dispersion characteristic. The origin of the bistable regime is a fast 275 ps relaxation time, electronically induced in the nonlinear refraction index. A low intensity threshold of 4 kW/cm² was observed, with a contrast of 65% between the high and low reflectivity states.

The authors conclude that the key to achieving bistable operation in this system is the combination of a high quality factor that reduces power thresholds and increases the relative nonlinear shift with respect to the width of the resonance, and the appropriate location of the optical resonance with respect to the QW absorption, leading to a good compromise between dispersion and absorption in the Urbach tail.

Yang et al. [241] experimentally observed optical bistability enhanced through sharp Fano interferences in high- Q localized silicon photonic crystal resonances $Q \sim 30,000$ and modal volume ~ 0.98 cubic wavelengths. This phenomenon was analyzed through nonlinear coupled-mode formalism, including the interplay of $\chi^{(3)}$ effects such as two-photon absorption and related

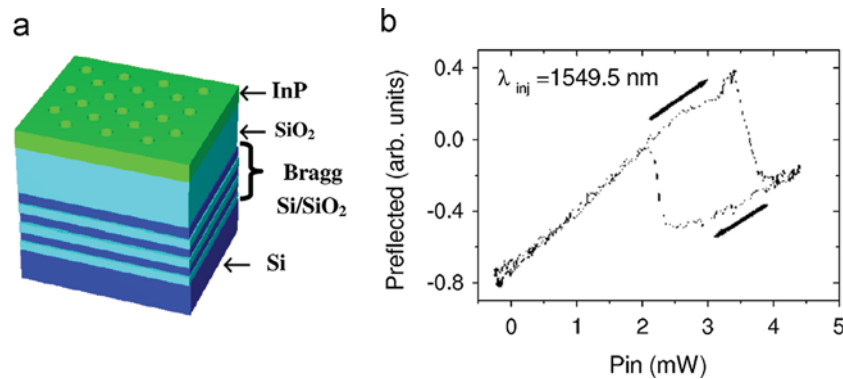


Fig. 64. (a) Sketch of the 2D PCS structure; and (b) hysteresis cycle corresponding to bistability of the reflected power at the operation wavelength. Reproduced with permission from [236].

free-carrier dynamics, optical Kerr as well as thermal effects and linear losses. Experimental and theoretical results demonstrate Fano resonance based bistable states with switching thresholds of 185 μW and 4.5 fJ internally stored cavity energy (~ 540 fJ consumed energy) in silicon for scalable optical buffering and logic.

While bistability is well known as a building block for all-optical memories, switching, and logic gates, excitability underlies spiking behavior toward external stimuli [251–253]. This was originally introduced in neuroscience as the mechanism responsible for the action potentials firing in neurons. In optics, excitability has mainly been studied in active resonators. First demonstrated in a semiconductor laser under optical feedback, it has been recently investigated in microphotronics and nanophotonics, namely in a 2D PCS band-edge resonator, where it has been identified as thermo-optical excitability [254]. More recently, the optical torque wrench, a fascinating example of excitability, was reported in the context of optomechanics [255]. Importantly, an excitable system may undergo a transition to self-sustained oscillations as long as the control parameter is varied.

Fast third-order nonlinearity is the key to achieving the previously mentioned regimes in an optical cavity. Because these effects are generally weak, their enhancement is of central importance in reducing operation thresholds. For instance, nonlinear effects can be enhanced in systems allowing tight light confinement and low optical losses, such as PhC nanocavities. A reduction of both the optical volume and optical losses leads to a decrease of the bistability threshold since the latter scales as V/Q^2 [237]. A few theoretical works have been reported by Bulgakov et al. [256,257] [258–260] on coupled non-linear Fano resonance cavities based on PhC structures. So far, only few works were devoted to the understanding and implementation of nonlinear dynamics in PhC nanocavities. They have mostly focused on the optical bistability of thermal origin, mainly because thermal effects in ultra-small cavities are usually dominant when compared to ultra-fast nonlinearities. Electronic nonlinearities in nanoresonators are more difficult to achieve and observe due to technological issues and the small signals at play with fast time frames (picosecond to nanosecond). Even so, some works have recently demonstrated the bistability of electronic origin in PhC nanocavities [255,261]. Brunstein et al. [251] experimentally demonstrated excitability and self-pulsing in a 2D PhC nanocavity. These nonlinear dynamic regimes have been achieved through a competition between electronic and thermal nonlinear responses. The excitable pulses showed a duration in the time scale of the thermal processes ($\sim 1 \mu\text{s}$). In addition, the refractory time was investigated and a linear dependency was found between this time and the pulse duration. These results might open a door to future applications for active photonic crystal nanocavities as integrated networks of nonlinear optical cells.

11. Conclusions and prospects

This review offers comprehensive coverage of recent progress made in defect-free 2D PCS based Fano resonance photonics. Due to the coupling of in-plane discrete guide modes with the vertical continuum radiation mode, Fano resonance arises, and enables light coupling and manipulation from out of the plane directions, which offers additional dimensions for a range of surface-normal devices and structures. The unique asymmetric shapes, associated with the sharp transitions in amplitude and phase between peaks and dips in the transmission/reflection spectra at Fano resonances, enable a wide range of spectral linewidth control, from broadband (flattop) membrane reflectors, to ultra-high Q filters, with potentially infinite Q factors in coupled double-layer PCS filters. Sensors based on Fano resonance principles can be intrinsically much more

sensitive, and scalable for 2D integration and multiplexing, owing to its simple and robust out-of-plane light coupling scheme. Localized field enhancement over a broad area in these dielectric Fano resonance structures can be more attractive for applications where spatial resolution is not a major concern, such as photodetector, sensor, and solar cell applications. With proper design, the development of ultra-thin membrane layers with complete (100%) transmission, reflection, or absorption is feasible. Cavity enhanced optical forces in coupled Fano resonance PCS cavities offer a new platform for large area membrane manipulation and optomechanic control for reconfigurable cavities. The dispersion and slow light property can be leveraged for novel device applications, such as low threshold lasers, low switching energy modulators and switches, bistability and memory devices, as well as other nonlinear optical structures.

Additionally, a wide range of planar dielectric structures can be used to realize a different kind of optical beam control functions, such as coupling, focusing, collimation, isolation, and beam steering, etc. Recently, metasurfaces, planar, ultra-thin metamaterials are the ones with reduced dimensionality in the form of quasi-2D curved structures for wavefront engineering and phase/polarization control of light propagation [251,261–264]. They also enable new physics and phenomena that are distinctively different from those observed in their 2D or 3D counterparts. Most importantly, these new structures are compatible with planar on-chip nano-photonic devices, for applications in integrated photonics. Exciting advances over the last few years have demonstrated great potential of metasurfaces for broadband flat optics, mostly based on metallic nano-antennas and subwavelength metallic grating, for negative refraction, optical vortices, reflections and refractions with phase discontinuity and phase front engineering, and for enhanced quantum emission with enhancement of photonic density of states in highly anisotropic hyperbolic metasurfaces [265]. Compared to metallic metasurfaces, Planar dielectric structures based on Fano resonance principles can offer similar functionalities with much reduced optical loss (with easy integration for gain) for large area planar optics and photonic structures [13,266].

Future research in the areas of fundamental studies, new structures, new devices, and integrated chips can lead to a wide range of applications towards 3D integrated photonics, reconfigurable optics, beam routing and shaping, vertical coupling, sensing systems, etc.

Acknowledgments

The authors acknowledge contributions from their current and former students, as well as collaborators involved in the research work reviewed here. We also thank funding agencies and program directors for their instrumental support from US Air Force Office of Scientific Research (AFOSR, Dr. Gernot Pomrenke), US Army Research Office (ARO, Dr. Michael Gerhold), and US National Science Foundation (NSF, Drs. John Zavada and Dominique Dagenais). We also thank the fabrication support from the University of Texas at Arlington Nanotechnology Research Center, and the University of Texas at Austin, part of NSF NNIN.

References

- [1] U. Fano, *Phys. Rev.* 124 (1961) 1866.
- [2] C. Ott, A. Kaldun, P. Raith, K. Meyer, M. Laux, J. Evers, C.H. Keitel, C.H. Greene, T. Pfeifer, *Science* 340 (2013) 716–720.
- [3] R. Wood, *Lond Edinb., Dublin Philos. Mag. J. Sci.* 4 (1902) 396–402.

- [4] A.E. Miroschnichenko, S. Flach, Y.S. Kivshar, *Rev. Mod. Phys.* 82 (2010) 2257.
- [5] B. Luk'yanchuk, N.I. Zheludev, S.A. Maier, N.J. Halas, P. Nordlander, H. Giessen, C.T. Chong, *Nat. Mater.* 9 (2010) 707–715.
- [6] M. Rahmani, B. Luk'yanchuk, M. Hong, *Laser Photonics Rev.* 7 (2013) 329–349.
- [7] V. Giannini, Y. Francescato, H. Amrania, C.C. Phillips, S.A. Maier, *Nano Lett.* 11 (2011) 2835–2840.
- [8] S. Fan, *Appl. Phys. Lett.* 80 (2002) 908.
- [9] S. Fan, J.D. Joannopoulos, *Phys. Rev. B* 65 (2002) 235112.
- [10] R. Magnusson, S.S. Wang, *Appl. Phys. Lett.* 61 (1992) 1022.
- [11] R. Magnusson, M. Shokoooh-Saremi, *Opt. Express* 16 (2008) 3456–3462.
- [12] H. Kikuta, H. Toyota, W. Yu, *Opt. Rev.* 10 (2003) 63–73.
- [13] C.J. Chang-Hasnain, *Semicond. Sci. Technol.* 26 (2011) 014043.
- [14] L. Chen, M.C.Y. Huang, C.F.R. Mateus, C.J. Chang-Hasnain, Y. Suzuki, *Appl. Phys. Lett.* 88 (2006) 031102.
- [15] S. Boutami, B. Bakir, P. Regreny, J. Leclercq, P. Viktorovitch, *Electron. Lett.* 43 (2007) 282.
- [16] L. Carletti, R. Malureanu, J. Mørk, I.S. Chung, *Opt. Express* 19 (2011) 23567–23572.
- [17] S.G. Tikhodeev, A.L. Yablonskii, E.A. Muljarov, N.A. Gippius, T. Ishihara, *Phys. Rev. B* 66 (2002) 45102.
- [18] S.G. Johnson, F. Shanhui, P.R. Villeneuve, J.D. Joannopoulos, L.A. Kolodziejski, *Phys. Rev. B (Condens. Matter)* 60 (1999) 5751–5758.
- [19] J.D. Joannopoulos, S.G. Johnson, J.N. Winn, R.D. Meade, *Photonic Crystals: Molding the Flow of Light*, Princeton University Press, Princeton, New Jersey 08540, 2008.
- [20] W. Zhou, in: H.S. Nalwa (Ed.), *Encyclopedia of Nanoscience and Nanotechnology*, vol. 20, American Scientific Publishers, Valencia, California 91381, 2011.
- [21] J.C.C.A. Mekis, I. Kurland, S. Fan, P.R. Villeneuve, J.D. Joannopoulos, *Phys. Rev. Lett.* 77 (1996) 3787.
- [22] S.G. Johnson, M.L. Povinelli, J.D. Joannopoulos, *Active and passive optical components for WDM communication*, in: *Proceedings of SPIE-International Society for Optics and Photonics Engineering*, Denver, CO, USA, 2001.
- [23] S. John, O. Toader, A. Chutinan, *IEICE Trans. Electron.* E87-C (2004) 266–273.
- [24] S. Noda, M. Imada, M. Okano, S. Ogawa, M. Mochizuki, A. Chutinan, *IEEE J. Quantum Electron.* 38 (2002) 726–735.
- [25] C.D. Seassal, Y., X. Letartre, C. Grillet, P. Rojo-Romeo, P. Viktorovitch, T. Benyattou, *IEEE J. Quantum Electron.* 38 (2002) 811–815.
- [26] S. Noda, T. Baba, *Roadmap on Photonic Crystals*, Springer, 2003.
- [27] M. Notomi, *Proc. IEEE* 99 (2011) 1768–1779.
- [28] M. Kanskar, P. Paddon, V. Pacradouni, R. Morin, A. Busch, J.F. Young, S.R. Johnson, J. MacKenzie, T. Tiedje, *Appl. Phys. Lett.* 70 (1997) 1438–1440.
- [29] S. Fan, W. Suh, J. Joannopoulos, *J. Opt. Soc. Am.* 20 (2003) 569–572.
- [30] W. Suh, Z. Wang, S. Fan, *IEEE J. Quantum Electronics* 40 (2004) 1511–1518.
- [31] H.A. Haus, *Waves and Fields in Optoelectronics*, Prentice-Hall Englewood Cliffs, NJ, 1984.
- [32] K.X. Wang, Z. Yu, S. Sandhu, S. Fan, *Opt. Lett.* 38 (2013) 100–102.
- [33] A. Rosenberg, M. Carter, J. Casey, M. Kim, R. Holm, R. Henry, C. Eddy, V. Shamamian, K. Bussmann, S. Shi, D.W. Prather, *Opt. Express* 13 (2005) 6564–6571.
- [34] M. Moharam, T. Gaylord, *J. Opt. Soc. Am. A* 71 (1981) 811–818.
- [35] M. Moharam, E.B. Grann, D.A. Pommet, T. Gaylord, *J. Opt. Soc. Am. A* 12 (1995) 1068–1076.
- [36] V. Liu, S. Fan, *Comput. Phys. Commun.* 183 (2012) 2233–2244.
- [37] K. Johnson, *Appl. Phys.* 24 (1981) 249–260.
- [38] Y. Shuai, D. Zhao, Z. Tian, J. Seo, D.V. Plant, Z. Ma, S. Fan, W. Zhou, *Opt. Express* 21 (2013) 24582–24589.
- [39] A. Taflove, S.C. Hagness, *Computational Electrodynamics: The Finite-difference Time-domain Method*, Artech House, 2000.
- [40] Z. Qiang, H. Yang, L. Chen, H. Pang, Z. Ma, W. Zhou, *Appl. Phys. Lett.* 93 (2008) 061106.
- [41] W. Zhou, Z. Ma, H. Yang, Z. Qiang, G. Qin, H. Pang, L. Chen, W. Yang, S. Chuwongin, D. Zhao, *J. Phys. D Appl. Phys.* 42 (2009) 234007.
- [42] D. Taillaert, W. Bogaerts, P. Bienstman, T. Krauss, P. Van Daele, I. Moerman, S. Versteuyft, K. De Mesel, R. Baets, *IEEE J. Quantum Electron.* 38 (2002) 949–955.
- [43] Y. Kanamori, T. Kitani, K. Hane, *Appl. Phys. Lett.* 90 (2007) 031911.
- [44] C. Lin, Z. Lu, S. Shi, G. Jin, D.W. Prather, *Appl. Phys. Lett.* 87 (2005) 091102.
- [45] W. Suh, S. Fan, *Appl. Phys. Lett.* 84 (2004) 4905.
- [46] S. Boutami, B.B. Bakir, H. Hattori, X. Letartre, J.L. Leclercq, P. Rojo-Romeo, M. Garrigues, C. Seassal, P. Viktorovitch, *Photonics Technology Letters, IEEE* 18 (2006) 835–837.

- [47] J.A. Rogers, M.G. Lagally, R.G. Nuzzo, *Nature* 477 (2011) 45–53.
- [48] S.W. Hwang, H. Tao, D.H. Kim, H. Cheng, J.K. Song, E. Rill, M.A. Brenckle, B. Panilaitis, S.M. Won, Y.S. Kim, *Science* 337 (2012) 1640–1644.
- [49] O.G. Schmidt, K. Eberl, *Nature* 410 (2001) 168.
- [50] R. Trotta, P. Atkinson, J. Plumhof, E. Zallo, R. Rezaev, S. Kumar, S. Baunack, J. Schröter, A. Rastelli, O. Schmidt, *Adv. Mater.* 24 (2012) 2668–2672.
- [51] X. Li, *Adv. Opt. Photon.* 3 (2011) 366–387.
- [52] S.A. Scott, M.G. Lagally, *J. Phys. D Appl. Phys.* 40 (2007) R75–R92.
- [53] H.C. Yuan, Z. Ma, M.M. Roberts, D.E. Savage, M.G. Lagally, *J. Appl. Phys.* 100 (2006) 013708.
- [54] L. Sun, G. Qin, J.H. Seo, G.K. Celler, W. Zhou, Z. Ma, *Small* 6 (2010) 2553–2557.
- [55] K. Zhang, J.H. Seo, W. Zhou, Z. Ma, *J. Phys. D Appl. Phys.* 45 (2012) 143001.
- [56] W. Zhou, Z. Ma, H. Yang, L. Chen, W. Yang, Z. Qiang, G. Qin, H. Pang, S. Chuwongin, D. Zhao, in: *Proceedings of SPIE*, 2010.
- [57] H. Yang, D. Zhao, S. Chuwongin, J.H. Seo, W. Yang, Y. Shuai, J. Berggren, M. Hammar, Z. Ma, W. Zhou, *Nat. Photon.* 6 (2012) 615–620.
- [58] E. Yablonovitch, T. Gmitter, J. Harbison, R. Bhat, *Appl. Phys. Lett.* 51 (1987) 2222.
- [59] P. Demeester, I. Pollentier, P. De Dobbelaere, C. Brys, P. Van Daele, *Semicond. Sci. Technol.* 8 (1993) 1124–1135.
- [60] J. Schermer, P. Mulder, G. Bauhuis, M. Voncken, J. Van Deelen, E. Haverkamp, P. Larsen, *Physica Status Solidi (a)* 202 (2005) 501–508.
- [61] O. Moutanabbir, U. Gösele, *Annu. Rev. Mater. Res.* 40 (2010) 469–500.
- [62] J. Haisma, G. Spierings, *Mater. Sci. Eng.: R: Rep.* 37 (2002) 1–60.
- [63] C.-T. Ko, K.-N. Chen, *Microelectron. Reliab.* 50 (2010) 481–488.
- [64] M.A. Meitl, Z.T. Zhu, V. Kumar, K.J. Lee, X. Feng, Y.Y. Huang, I. Adesida, R.G. Nuzzo, J.A. Rogers, *Nat. Mater.* 5 (2006) 33–38.
- [65] S.M. Harazim, V.A.B. Quinones, S. Sanchez, O. Schmidt, Lab-in-a-tube: On-chip Integration of Glass Optofluidic Ring Resonators for Label-free Sensing Applications, *Lab Chip* 12 (2012) 2649–2655.
- [66] Y.M. Song, Y. Xie, V. Malyarchuk, J. Xiao, I. Jung, K.-J. Choi, Z. Liu, H. Park, C. Lu, R.-H. Kim, *Nature* 497 (2013) 95–99.
- [67] W. Zhou, Z. Ma, *IEEE Photon. J.* 5 (2013).
- [68] J. Hu, L. Li, H. Lin, P. Zhang, W. Zhou, Z. Ma, *Opt. Mater. Express* 3 (2013) 1313.
- [69] M.M. Roberts, L.J. Klein, D.E. Savage, K.A. Slinker, M. Friesen, G. Celler, M.A. Eriksson, M.G. Lagally, *Nat. Mater.* 5 (2006) 388–393.
- [70] J.A. Rogers, T. Someya, Y. Huang, *Science* 327 (2010) 1603.
- [71] C. Janglin, C.T. Liu, *IEEE* 1 (2013) 150–158.
- [72] H. Ko, K. Takei, R. Kapadia, S. Chuang, H. Fang, P.W. Leu, K. Ganapathi, E. Plis, H.S. Kim, S.-Y. Chen, *Nature* 468 (2010) 286–289.
- [73] Y. Chen, H. Li, M. Li, *Sci. Rep.* 2 (2012).
- [74] J.-H. Seo, J. Park, D. Zhao, H. Yang, W. Zhou, B.-K. Ju, Z. Ma, *Photon. J., IEEE* 5 (2013) 2200106.
- [75] H.-C. Yuan, J. Shin, G. Qin, L. Sun, P. Bhattacharya, M.G. Lagally, G.K. Celler, Z. Ma, *Appl. Phys. Lett.* 94 (2009) 013102.
- [76] C. Boztug, J. Sánchez-Pérez, F. Sudradjat, R. Jacobson, D. Paskiewicz, M. Lagally, R. Paiella, *Small* (2012).
- [77] H. Zhou, J.-H. Seo, D.M. Paskiewicz, Y. Zhu, G.K. Celler, P. Voyles, W. Zhou, M. Lagally, Z. Ma, *Nat. Sci. Rep.* 3 (2013) 1291.
- [78] J. Yoon, S. Jo, I.S. Chun, I. Jung, H.-S. Kim, M. Meitl, E. Menard, X. Li, J.J. Coleman, U. Paik, J.A. Rogers, *Nature* 465 (2010) 329–333.
- [79] W. Yang, H. Yang, G. Qin, Z. Ma, J. Berggren, M. Hammar, R. Soref, W. Zhou, *Appl. Phys. Lett.* 96 (2010) 121107.
- [80] A. chadha, W. Yang, T. Saha, S. Chuwongin, Y. Shuai, W. Zhou, G.J. Brown, Z. Ma, *Proc. SPIE* 8268 (2012) 8268G.
- [81] H.-s. Kim, E. Brueckner, J. Song, Y. Li, S. Kim, C. Lu, J. Sulkin, K. Choquette, Y. Huang, R.G. Nuzzo, J. A. Rogers, *Proc. Natl. Acad. Sci.* 108 (2011) 10072–10077.
- [82] T.-H. Kim, W.M. Choi, D.-H. Kim, M.A. Meitl, E. Menard, H. Jiang, J.A. Carlisle, J.A. Rogers, *Adv. Mater.* 20 (2008) 2171–2176.
- [83] C.A. Bower, E. Menard, S. Bonafede, J.W. Hamer, R.S. Cok, 2010 Proceedings of 60th Electronic Components and Technology Conference (ECTC), 2010.

- [84] C.A. Bower, E. Menard, P.E. Garrou, in: Proceedings of 58th Electronic Components and Technology Conference, ECTC 2008, 2008.
- [85] S. Kim, J. Wu, A. Carlson, S.H. Jin, A. Kovalsky, P. Glass, Z. Liu, N. Ahmed, S.L. Elgan, W. Chen, P.M. Ferreira, M. Sitti, Y. Huang, J.A. Rogers, Proc. Natl. Acad. Sci. (2010).
- [86] S. Jung-Hun, P. Jungho, Z. Deyin, Y. Hongjun, Z. Weidong, J. Byeong-kwon, M. Zhenqiang, Photon. J. IEEE 5 (2013) (2200106–2200106).
- [87] R. Saeidpourazar, L. Rui, L. Yuhang, M.D. Sangid, L. Chaofeng, H. Yonggang, J.A. Rogers, P.M. Ferreira, J. Microelectromechan. Syst. 21 (2012) 1049–1058.
- [88] J.H. Seo, T.Y. Oh, J. Park, W. Zhou, B.K. Ju, Z. Ma, Adv. Funct. Mater. 23 (2013) 3398–3403.
- [89] M.J. Zablocki, A. Sharkawy, O. Ebil, D.W. Prather, Opt. Lett. 36 (2011) 58–60.
- [90] A. Ghaffari, A. Hosseini, X. Xu, D. Kwong, H. Subbaraman, R.T. Chen, Opt. Express 18 (2010) 20086–20095.
- [91] W. Zhou, Z. Ma, S. Chuwongin, Y.-C. Shuai, J.-H. Seo, D. Zhao, H. Yang, W. Yang, Opt. Quantum Electron. 44 (2012) 605–611.
- [92] D. Chanda, K. Shigeta, S. Gupta, T. Cain, A. Carlson, A. Mihi, A.J. Baca, G.R. Bogart, P. Braun, J.A. Rogers, Nat. Nanotechnol. 6 (2011) 402–407.
- [93] D. Hines, V. Ballarotto, E. Williams, Y. Shao, S. Solin, J. Appl. Phys. 101 (2007) 024503.
- [94] H.C. Yuan, G.K. Celler, Z. Ma, J. Appl. Phys. 102 (2007) 034501.
- [95] H. Yang, Z. Qiang, H. Pang, Z. Ma, W.D. Zhou, Electron. Lett. 44 (2008) 858–859.
- [96] L. Chen, Z. Qiang, H. Yang, H. Pang, Z. Ma, W.D. Zhou, Opt. Express 17 (2009) 8396–8406.
- [97] X. Xu, H. Subbaraman, A. Hosseini, C.Y. Lin, D. Kwong, R.T. Chen, Opt. Lett. 37 (2012) 1020–1022.
- [98] E. Yablonovitch, D. Hwang, T. Gmitter, L. Florez, J. Harbison, Appl. Phys. Lett. 56 (1990) 2419–2421.
- [99] K. Jeonghee, N.G. Toledo, S. Lal, L. Jing, T.E. Buehl, U.K. Mishra, Electron Device Lett., IEEE 34 (2013) 42–44.
- [100] W. Maszara, J. Electrochem. Soc. 138 (1991) 341–347.
- [101] K. Tanabe, K. Watanabe, Y. Arakawa, Sci. Rep. 2 (2012).
- [102] A.M. Kiefer, D.M. Paskiewicz, A.M. Clausen, W.R. Buchwald, R.A. Soref, M.G. Lagally, ACS Nano 5 (2011) 1179–1189.
- [103] G. Roelkens, J. Van Campenhout, J. Brouckaert, D. Van Thourhout, R. Baets, P.R. Romeo, P. Regreny, A. Kazmierczak, C. Seassal, X. Letartre, G. Hollinger, J.M. Fedeli, L. Di Cioccio, C. Lagahe-Blanchard, Mater. Today 10 (2007) 36–43.
- [104] F. Niklaus, G. Stemme, J.-Q. Lu, R.J. Gutmann, J. Appl. Phys. 99 (2006) 031101–031128.
- [105] C.-T. Ko, K.-N. Chen, Microelectron. Reliab. 52 (2012) 302–311.
- [106] T. Akatsu, C. Deguet, L. Sanchez, F. Allibert, D. Rouchon, T. Signamarcheix, C. Richtarch, A. Boussagol, V. Loup, F. Mazen, J.-M. Hartmann, Y. Campidelli, L. Clavelier, F. Letertre, N. Kernevez, C. Mazure, Mater. Sci. Semicond. Process. 9 (2006) 444–448.
- [107] M. Bruel, Electron. Lett. 31 (1995) 1201–1202.
- [108] G. Roelkens, D. Van Thourhout, R. Baets, J. Lightwave Technol. 23 (2005) 3827–3831.
- [109] G. Roelkens, L. Liu, D. Liang, R. Jones, A. Fang, B. Koch, J. Bowers, Laser Photon. Rev. 4 (2010) 751–779.
- [110] D. Liang, G. Roelkens, R. Baets, J. Bowers, Materials 3 (2010) 1782–1802.
- [111] A.W. Fang, H. Park, O. Cohen, R. Jones, M.J. Paniccia, J.E. Bowers, Opt. Express 14 (2006) 9203–9210.
- [112] A.W. Fang, H. Park, Y.-h. Kuo, R. Jones, O. Cohen, D. Liang, O. Raday, M.N. Sysak, M.J. Paniccia, J.E. Bowers, Mater. Today 10 (2007) 28–35.
- [113] F. Niklaus, G. Stemme, J.-Q. Lu, R. Gutmann, J. Appl. Phys. 99 (2006) 031101.
- [114] H. Yang, D. Zhao, J. Seo, S. Kim, J. Rogers, Z. Ma, W. Zhou, IEEE Photon. Technol. Lett. 24 (2012) 476–478.
- [115] A. Carlson, S. Wang, P. Elvikis, P.M. Ferreira, Y. Huang, J.A. Rogers, Adv. Funct. Mater. 22 (2012) 4476–4484.
- [116] S.T. Thurman, G.M. Morris, Appl. Opt. 42 (2003) 3225–3233.
- [117] K.B. Crozier, V. Lousse, O. Kilic, S. Kim, S. Fan, O. Solgaard, Phys. Rev. B 73 (2006) 115126.
- [118] W. Suh, O. Solgaard, S. Fan, J. Appl. Phys. 98 (2005) 033102.
- [119] W. Suh, S. Fan, Opt. Lett. 28 (2003) 1763–1765.
- [120] V. Liu, M. Povinelli, S. Fan, Opt. Express 17 (2009) 21897–21909.
- [121] S. Peng, G. Morris, J. Opt. Soc. Am. A 13 (1996) 993–1005.
- [122] I. McKerracher, L. Fu, H. Tan, C. Jagadish, J. Phys. D Appl. Phys. 46 (2013) 095104.
- [123] V. Lousse, W. Suh, O. Kilic, S. Kim, O. Solgaard, S.H. Fan, Opt. Express 12 (2004) 1575–1582.
- [124] T. Stomeo, M. Grande, G. Rainò, A. Passaseo, A. D'Orazio, R. Cingolani, A. Locatelli, D. Modotto, C. De Angelis, M. De Vittorio, Opt. Lett. 35 (2010) 411–413.
- [125] Y. Roh, T. Tanabe, A. Shinya, H. Taniyama, E. Kuramochi, S. Matsuo, T. Sato, M. Notomi, Phys. Rev. B 81 (2010) 121101.

- [126] W. Suh, M.F. Yanik, O. Solgaard, S. Fan, Appl. Phys. Lett. 82 (2003) 1999.
- [127] Y. Shuai, D. Zhao, A. Singh Chadha, J.-H. Seo, H. Yang, S. Fan, Z. Ma, W. Zhou, Appl. Phys. Lett. 103 (2013) 241106.
- [128] A.E. Willner, Nat Photon 1 (2007) 87–88.
- [129] D. Babic, S. Corzine, IEEE J. Quantum Electron. 28 (1992) 514–524.
- [130] M.C.Y. Huang, Y. Zhou, C.J. Chang-Hasnain, Nat. Photon. 1 (2007) 119–122.
- [131] D.L. Brundrett, T.K. Gaylord, E.N. Glytsis, Appl. Opt. 37 (1998) 2534–2541.
- [132] H. Wu, W. Mo, J. Hou, D. Gao, R. Hao, H. Jiang, R. Guo, W. Wu, Z. Zhou, J. Opt. 12 (2010) 045703.
- [133] V. Karagodsky, F.G. Sedgwick, C.J. Chang-Hasnain, Opt. Express 18 (2010) 16973–16988.
- [134] Z. Qiang, H. Yang, S. Chuwongin, D. Zhao, Z. Ma, W. Zhou, Photon. Technol. Lett., IEEE 22 (2010) 1108–1110.
- [135] H. Yang, S. Chuwongin, Z. Qiang, L. Chen, H. Pang, Z. Ma, W. Zhou, Appl. Phys. Lett. 95 (2009) 023110.
- [136] Y. Shuai, D. Zhao, G. Medhi, R. Peale, Z. Ma, W. Buchwald, R. Soref, W. Zhou, IEEE Photon. J. 5 (2013).
- [137] K. Balasundaram, P.K. Mohseni, Y.-C. Shuai, D. Zhao, W. Zhou, X. Li, Appl. Phys. Lett. 103 (2013) 214103.
- [138] J. Kim, L. Chrostowski, E. Bissillon, D. Plant, Opt. Express 15 (2007) 10330–10339.
- [139] C. Sauvan, J. Hugonin, P. Lalanne, Appl. Phys. Lett. 95 (2009) 211101.
- [140] D. Zhao, Z. Ma, W. Zhou, Opt. Express. 18 (2010) 14152–14158.
- [141] L. Coldren, S. Corzine, Diode Lasers and Photonic Integrated Circuits, Wiley, New York, 1995.
- [142] A. Chadha, D. Zhao, S. Chuwongin, Z. Ma, W. Zhou, Appl. Phys. Lett. 103 (2013) 211107.
- [143] E. Yablonovitch, Phys. Rev. Lett. 58 (1987) 2059–2062.
- [144] S. Noda, M. Fujita, T. Asano, Nat. Photon. 1 (2007) 449–458.
- [145] O. Painter, Science 284 (1999) 1999.
- [146] J. Hwang, H. Ryu, D. Song, I. Han, H. Park, D. Jang, Y. Lee, IEEE Photon. Technol. Lett. 12 (2000) 1295–1297.
- [147] W.D. Zhou, J. Sabarinathan, P. Bhattacharya, B. Kochman, E.W. Berg, P.C. Yu, S.W. Pang, IEEE J. Quantum Electron 37 (2001) 1153–1160.
- [148] R. Colombelli, K. Srinivasan, M. Troccoli, O. Painter, C.F. Gmachl, D.M. Tennant, A.M. Sergent, D.L. Sivco, A. Y. Cho, F. Capasso, Science 302 (2003) 1374–1377.
- [149] H.-G. Park, S.-H. Kim, S.-H. Kwon, Y.-G. Ju, J.-K. Yang, J.-H. Baek, S.-B. Kim, Y.-H. Lee, Science 305 (2004) 1444–1447.
- [150] P. Bhattacharya, J. Sabarinathan, J. Topol'ancik, S. Chakravarty, P. Yu, W. Zhou, Proc. IEEE 93 (2005) 1825–1838.
- [151] B. Ellis, M.A. Mayer, G. Shambat, T. Sarmiento, J. Harris, E.E. Haller, J. Vučković, Nat. Photon. 5 (2011) 297–300.
- [152] D.S. Song, S.H. Kim, H.G. Park, C.K. Kim, Y.H. Lee, Appl. Phys. Lett. 80 (2002) 3901–3903.
- [153] N. Yokouchi, A. Danner, K.D. Choquette, IEEE J. Sel. Top. Quantum Electron. 9 (2003) 1439–1445.
- [154] A. Furukawa, S. Sasaki, M. Hoshi, A. Matsuzono, K. Moritoh, T. Baba, Appl. Phys. Lett. 85 (2004) 5161–5163.
- [155] L.D. Lundberg, D.L. Boiko, E. Kapon, Appl. Phys. Lett. 87 (2005) 241120.
- [156] J.P. Dowling, M. Scalora, M.J. Bloemer, C.M. Bowden, J. Appl. Phys. 75 (1994) 1896–1899.
- [157] M. Meier, A. Mekis, A. Dodabalapur, A.A. Timko, R.E. Slusher, J.D. Joannopoulos, O. Nalamasu, Appl. Phys. Lett. 74 (1999) 7–9.
- [158] S. Noda, M. Yokoyama, M. Imada, A. Chutinan, M. Mochizuki, Science 293 (2001) 1123–1125.
- [159] N. Susa, J. Appl. Phys. 89 (2001) 815–823.
- [160] S. Noda, J. Opt. Soc. Am. B 27 (2010) B1–B8.
- [161] C. Sciancalepore, B.B. Bakir, X. Letartre, J. Harduin, N. Olivier, C. Seassal, J. Fedeli, P. Viktorovitch, IEEE Photon. Technol. Lett. 24 (2012) 455–457.
- [162] S.-L. Chua, Y. Chong, A.D. Stone, M. Soljacic, J. Bravo-Abad, Low-threshold Lasing Action in Photonic Crystal Slabs Enabled by Fano Resonances, 2011.
- [163] W.D. Zhou, J. Sabarinathan, B. Kochman, E. Berg, O. Qasaimeh, S. Pang, P. Bhattacharya, Electron. Lett. 36 (2000) 1541–1542.
- [164] D. Zhao, H. Yang, S. Chuwongin, J.H. Seo, Z. Ma, W. Zhou, IEEE Photon. J. 4 (2012) 2169–2175.
- [165] R. Magnusson, Y. Ding, K. Lee, D. Shin, P.S. Priambodo, P.P. Young, T.A. Maldonado, in: SPIE's 48th Annual Meeting on Optical Science and Technology, International Society for Optics and Photonics, 2003.
- [166] H. Hattori, X. Letartre, C. Seassal, P. Rojo-Romeo, J. Leclercq, P. Viktorovitch, Opt. Express 11 (2003) 1799–1808.
- [167] S. Boutami, B. Benbakir, X. Letartre, J. Leclercq, P. Regreny, P. Viktorovitch, IEEE J. Sel. Top. Quantum Electron. 6 (2000) 1244–1253.

- [168] S. Boutami, B. Benbakir, X. Letartre, J.L. Leclercq, P. Regreny, P. Viktorovitch, *Opt. Express* 15 (2007) 12443–12449.
- [169] B.B. Bakir, C. Seassal, X. Letartre, P. Viktorovitch, M. Zussy, L. Di Cioccio, J.M. Fedeli, *Appl. Phys. Lett.* 88 (2006) 081113.
- [170] I.S. Chung, J. Mørk, *Appl. Phys. Lett.* 97 (2010) 151113.
- [171] P. Viktorovitch, B. Ben Bakir, S. Boutami, J.L. Leclercq, X. Letartre, P. Rojo-Romeo, C. Seassal, M. Zussy, L. Di Cioccio, J.M. Fedeli, *Laser Photon. Rev.* 4 (2010) 401–413.
- [172] Z. Ma, W. Zhou, USPTO, Wisconsin Alumni Research Foundation, USA, 2012.
- [173] D. Zhao, S. Chuwongin, H. Yang, J.H. Seo, J. Berggren, M. Hammar, Z. Ma, W. Zhou, 2012 IEEE 9th International Conference on Group IV Photonics (GFP), IEEE, San Diego, CA, 2012.
- [174] J.N. Anker, W.P. Hall, O. Lyandres, N.C. Shah, J. Zhao, R.P. Van Duyne, *Nat. Mater.* 7 (2008) 442–453.
- [175] K.T. Posani, V. Tripathi, S. Annamalai, N.R. Weiss-Bernstein, S. Krishna, R. Perahia, O. Crisafulli, O.J. Painter, *Appl. Phys. Lett.* 88 (2006) 151104.
- [176] L. Chen, W. Zhou, Z. Qiang, G.J. Brown, *Proc. SPIE* 6370 (2006) 63701I.
- [177] W.D. Zhou, H. Yang, Z. Qiang, L. Chen, G.J. Brown, *Proc. SPIE* 7095 (2008) 709507.
- [178] G. Veronis, R.W. Dutton, S. Fan, *J. Appl. Phys.* 97 (2005) 93104.
- [179] S.J. Lee, Z. Ku, A. Barve, J. Montoya, W.Y. Jang, S. Brueck, M. Sundaram, A. Reisinger, S. Krishna, S.K. Noh, *Nat. Commun.* 2 (2011) 286.
- [180] C.C. Chang, Y.D. Sharma, Y.S. Kim, J.A. Bur, R.V. Shenoi, S. Krishna, D. Huang, S.Y. Lin, *Nano Lett.* 10 (2010) 1704–1709.
- [181] N. Liu, M.L. Tang, M. Hentschel, H. Giessen, A.P. Alivisatos, *Nat. Mater.* 10 (2011) 631–636.
- [182] M. Fujita, S. Takahashi, Y. Tanaka, T. Asano, S. Noda, *Science* 308 (2005) 1296–1298.
- [183] H. Altug, J. Vuckovic, *Opt. Express* 13 (2005) 8819–8828.
- [184] S.Y. Lin, J.G. Fleming, Z.Y. Li, I. El-Kady, R. Biswas, K.M. Ho, *J. Opt. Soc. Am. B (Opt. Phys.)* 20 (2003) 1538–1541.
- [185] Y. Xi, X. Wang, X. Hu, X. Liu, J. Zi, *Chinese Phys. Lett.* 19 (2002) 1819–1821.
- [186] J. Yu, Y. Shen, X. Liu, R. Fu, J. Zi, Z. Zhu, *J. Phys.: Condens. Matter* 16 (2004) L51–56.
- [187] B. Temelkuran, E. Ozbay, J.P. Kavanaugh, G. Tuttle, K.M. Ho, *Appl. Phys. Lett.* 72 (1998) 2376.
- [188] M. Florescu, H. Lee, A.J. Stimpson, J. Dowling, *Phys. Rev. A* 72 (2005) 33821.
- [189] J.G. Fleming, S.Y. Lin, I. El-Kady, R. Biswas, K.M. Ho, *Nature* 417 (2002) 52–55.
- [190] S.Y. Lin, J. Moreno, J.G. Fleming, *Appl. Phys. Lett.* 83 (2003) 380–382.
- [191] M.S. Unlu, S. Strite, *J. Appl. Phys.* 78 (1995) 607–639.
- [192] J.B. Pendry, A. MacKinnon, *Phys. Rev. Lett.* 69 (1992) 2772–2775.
- [193] S. Scharfner, S. Golka, C. Pflugl, W. Schrenk, A.M. Andrews, T. Roch, G. Strasser, *Appl. Phys. Lett.* 89 (2006) 151107.
- [194] W. Zhou, L. Chen, Z. Qiang, G.J. Brown, *J. Nanophoton.* 1 (2007) 013515.
- [195] L. Chen, H. Yang, Z. Qiang, H. Pang, L. Sun, Z. Ma, R. Pate, A. Stiff-Roberts, S. Gao, J. Xu, G.J. Brown, W. Zhou, *Appl. Phys. Lett.* 96 (2010) 083111.
- [196] A.W. Rodriguez, A.P. McCauley, P.-C. Hui, D. Woolf, E. Iwase, F. Capasso, M. Loncar, S.G. Johnson, *Opt. Express* 19 (2011) 2225–2241.
- [197] Z. Qiang, W.D. Zhou, M. Lu, G.J. Brown, *Proc. SPIE* 6901 (2008) 69010F.
- [198] W. Zhou, Z. Qiang, L. Chen, H. Yang, G.J. Brown, *Spectrally Selective Infrared Absorption Enhancement in Photonic Crystal Cavities*, 2008, p. 709507.
- [199] H. Kurt, M.N. Erim, N. Erim, *Sens. Actuators B: Chem.* 165 (2012) 68–75.
- [200] W.-C. Lai, S. Chakravarty, Y. Zou, Y. Guo, R.T. Chen, *Appl. Phys. Lett.* 102 (2013) 041111.
- [201] B. Cunningham, P. Li, B. Lin, J. Pepper, *Sens. Actuators B: Chem.* 81 (2002) 316–328.
- [202] X. Fan, I.M. White, S.I. Shopova, H. Zhu, J.D. Suter, Y. Sun, *Anal. Chim. Acta* 620 (2008) 8–26.
- [203] R. Magnusson, D. Wawro, S. Zimmerman, Y. Ding, *Sensors* 11 (2011) 1476–1488.
- [204] M. El Beheiry, V. Liu, S. Fan, O. Levi, *Opt. Express* 18 (2010) 22702–22714.
- [205] O. Levi, M.M. Lee, J. Zhang, V. Lousse, S.R.J. Brueck, S. Fan, J.S. Harris, *Proc. SPIE* 6447 (2007) 64470P.
- [206] O. Levi, T.T. Lee, M.M. Lee, S.J. Smith, J.S. Harris, *Appl. Opt.* 46 (2007) 1881–1889.
- [207] Y. Huang, G. Pandraud, P.M. Sarro, *Opt. Lett.* 37 (2012) 3162–3164.
- [208] S. Sha, H. Zhai, V.R. Rowda, N.W. Chen, W. Zhou, M. Lu, *Microw. Opt. Technol. Lett.* 54 (2012) 432–434.
- [209] O. Kilic, M. Dignonnet, G. Kino, O. Solgaard, *Measur. Sci. Technol.* 18 (2007) 3049–3054.
- [210] E. Nxcnons, G. Huu, A Preliminary Communication on the Pressure of Heat and Light Radiation, 1901.
- [211] T. Kippenberg, K. Vahala, *Science* 321 (2008) 1172–1176.

- [212] D. Van Thourhout, J. Roels, Nat. Photon. 4 (2010) 211–217.
- [213] P.T. Rakich, Popovi, M.A. cacute, Soljačić, M. cacute, E.P. Ippen, Nat. Photon. 1 (2007) 658–665.
- [214] M. Povinelli, S. Johnson, M. Lončar, M. Ibanescu, E. Smythe, F. Capasso, J. Joannopoulos, Opt. Express 13 (2005) 8286–8295.
- [215] M.L. Povinelli, M. Loncar, M. Ibanescu, E.J. Smythe, S.G. Johnson, F. Capasso, J.D. Joannopoulos, Opt. Lett. 30 (2005) 3042–3044.
- [216] M. Li, W. Pernice, C. Xiong, T. Baehr-Jones, M. Hochberg, H. Tang, Nature 456 (2008) 480–484.
- [217] M. Li, W. Pernice, H. Tang, Nat. Photon. 3 (2009) 464–468.
- [218] J. Roels, I. De Vlaminck, L. Lagae, B. Maes, D. Van Thourhout, R. Baets, Nat. Nanotechnol. 4 (2009) 510–513.
- [219] G.S. Wiederhecker, L. Chen, A. Gondarenko, M. Lipson, Nature 462 (2009) 633–636.
- [220] M. Eichenfield, C.P. Michael, R. Perahia, O. Painter, Nat. Photon. 1 (2007) 416–422.
- [221] M. Eichenfield, R. Camacho, J. Chan, K.J. Vahala, O. Painter, Nature 459 (2009) 550–555.
- [222] J. Ma, M.L. Povinelli, Cur. Opin. Solid State Mater. Sci. 16 (2012) 82–90.
- [223] M. Notomi, H. Taniyama, S. Mitsugi, E. Kuramochi, Phys. Rev. Lett. 97 (2006) 023903.
- [224] D. Woolf, P.-C. Hui, E. Iwase, M. Khan, A.W. Rodriguez, P. Deotare, I. Bulu, S.G. Johnson, F. Capasso, M. Loncar, Opt. Express 21 (2013) 7258–7275.
- [225] Y.-G. Roh, T. Tanabe, A. Shinya, H. Taniyama, E. Kuramochi, S. Matsuo, T. Sato, M. Notomi, Phys. Rev. B 81 (2010) 121101.
- [226] P.-C. Hui, D. Woolf, E. Iwase, Y.-I. Sohn, D. Ramos, M. Khan, A.W. Rodriguez, S.G. Johnson, F. Capasso, M. Loncar, Appl. Phys. Lett. 103 (2013) 021102.
- [227] T.-W. Lu, P.-T. Lee, Opt. Express 17 (2009) 1518–1526.
- [228] M.F. Yanik, S. Fan, Phys. Rev. A 71 (2005) 13803.
- [229] T.F. Krauss, J. Phys. D Appl. Phys. 40 (2007) 2666.
- [230] M. Notomi, K. Yamada, A. Shinya, J. Takahashi, C. Takahashi, I. Yokohama, Phys. Rev. Lett. 87 (2001) 253902.
- [231] Y.A. Vlasov, M. O'Boyle, H.F. Hamann, S.J. McNab, Nature 438 (2005) 65–69.
- [232] A. Miroshnichenko, Y. Kivshar, Opt. Express 13 (2005) 3969–3976.
- [233] S.F. Mingaleev, A.E. Miroshnichenko, Y.S. Kivshar, Coupled-resonator-induced Reflection in Photonic-crystal Waveguide Structures, (arXiv:0804.4140), 2008.
- [234] A.E. Miroshnichenko, Y.S. Kivshar, Appl. Phys. Lett. 95 (2009).
- [235] H.M. Gibbs, Optical Bistability: Controlling Light With Light, Quantum Electronics—Principles and Applications, Academic Press, 1985.
- [236] A.M. Yacomotti, F. Raineri, G. Vecchi, P. Monnier, R. Raj, A. Levenson, B.B. Bakir, C. Seassal, X. Letartre, P. Viktorovitch, Appl. Phys. Lett. 88 (2006) 231107.
- [237] M. Soljačić, M. Ibanescu, S.G. Johnson, Y. Fink, J.D. Joannopoulos, Phys. Rev. E 66 (2002) 055601.
- [238] A.E. Miroshnichenko, S.F. Mingaleev, S. Flach, Y.S. Kivshar, Phys. Rev. E 71 (2005) 036626.
- [239] S.F. Mingaleev, Y.S. Kivshar, J. Opt. Soc. Am. B 19 (2002) 2241–2249.
- [240] S.F. Mingaleev, Y.S. Kivshar, R.A. Sammut, Phys. Rev. E 62 (2000) 5777–5782.
- [241] X. Yang, C. Husko, C.W. Wong, M. Yu, D.-L. Kwong, Appl. Phys. Lett. 91 (2007) 051113.
- [242] A. Cowan, J. Young, Phys. Rev. E 68 (2003) 046606.
- [243] X. Letartre, J. Mouette, J.L. Leclercq, P. Rojo Romeo, C. Seassal, P. Viktorovitch, J. Lightw. Technol. 21 (2003) 1691–1699.
- [244] M. Notomi, A. Shinya, S. Mitsugi, G. Kira, E. Kuramochi, T. Tanabe, Opt. Express 13 (2005) 2678–2687.
- [245] C. Grillet, D. Freeman, B. Luther-Davies, S. Madden, R. McPhedran, D.J. Moss, M.J. Steel, B.J. Eggleton, Opt. Express 14 (2006) 369–376.
- [246] N. Inoue, T. Baba, Proc. SPIE 6352 (2006) 63520R.
- [247] L.Y. Mario, S. Darmawan, M.K. Chin, Opt. Express 14 (2006) 12770–12781.
- [248] J. Song, R. Proietti Zaccaria, M.B. Yu, X.W. Sun, Opt. Express 14 (2006) 8812–8826.
- [249] R. Harbers, S. Jochim, N. Moll, R.F. Mahrt, D. Erni, J.A. Hoffnagle, W.D. Hinsberg, Appl. Phys. Lett. 90 (2007) 201105.
- [250] V. Lousse, J.P. Vigneron, Phys. Rev. B 69 (2004) 155106.
- [251] M. Brunstein, A.M. Yacomotti, I. Sagnes, F. Raineri, L. Bigot, A. Levenson, Phys. Rev. A 85 (2012) 031803.
- [252] B. Maes, P. Bienstman, R. Baets, J. Opt. Soc. Am. B 22 (2005) 1778–1784.
- [253] B. Maes, P. Bienstman, R. Baets, Opt. Express 16 (2008) 3069–3076.
- [254] A.M. Yacomotti, P. Monnier, F. Raineri, B.B. Bakir, C. Seassal, R. Raj, J.A. Levenson, Phys. Rev. Lett. 97 (2006) 143904.
- [255] F. Pedaci, Z. Huang, M. van Oene, S. Barland, N.H. Dekker, Nat. Phys. 7 (2011) 259–264.

- [256] E.N. Bulgakov, A.F. Sadreev, Phys. Rev. B 78 (2008) 075105.
- [257] E.N. Bulgakov, A.F. Sadreev, Phys. Rev. B 80 (2009) 115308.
- [258] E.N. Bulgakov, A.F. Sadreev, Phys. Rev. B 81 (2010) 115128.
- [259] E.N. Bulgakov, A.F. Sadreev, Phys. Rev. B 86 (2012) 075125.
- [260] E.N. Bulgakov, A.F. Sadreev, J. Opt. Soc. Am. B 29 (2012) 2924–2928.
- [261] M. Notomi, T. Tanabe, A. Shinya, E. Kuramochi, H. Taniyama, S. Mitsugi, M. Morita, Opt. Express 15 (2007) 17458–17481.
- [262] N. Yu, P. Genevet, M.A. Kats, F. Aieta, J.-P. Tetienne, F. Capasso, Z. Gaburro, Science 334 (2011) 333–337.
- [263] X. Ni, N.K. Emani, A.V. Kildishev, A. Boltasseva, V.M. Shalaev, Science 335 (2012) 427.
- [264] N. Yu, P. Genevet, F. Aieta, M. Kats, R. Blanchard, G. Aoust, J. Tetienne, Z. Gaburro, F. Capasso, Flat Optics: Controlling Wavefronts With Optical Antenna Metasurfaces, 2013.
- [265] A.V. Kildishev, A. Boltasseva, V.M. Shalaev, Science 339 (2013).
- [266] H. Yamada, M. Nozawa, M. Kinoshita, K. Ohashi, Opt. Express 19 (2011) 698–703.